LBNL-39921
UC-414

ERNEST ORLANDO LAWRENCE
BERKELEY NATIONAL LABORATORY

Fluorescence Spectroscopy of Single Molecules at Room Temperature and Its Applications

Taekjip Ha
Materials Sciences Division

December 1996
Ph.D. Thesis

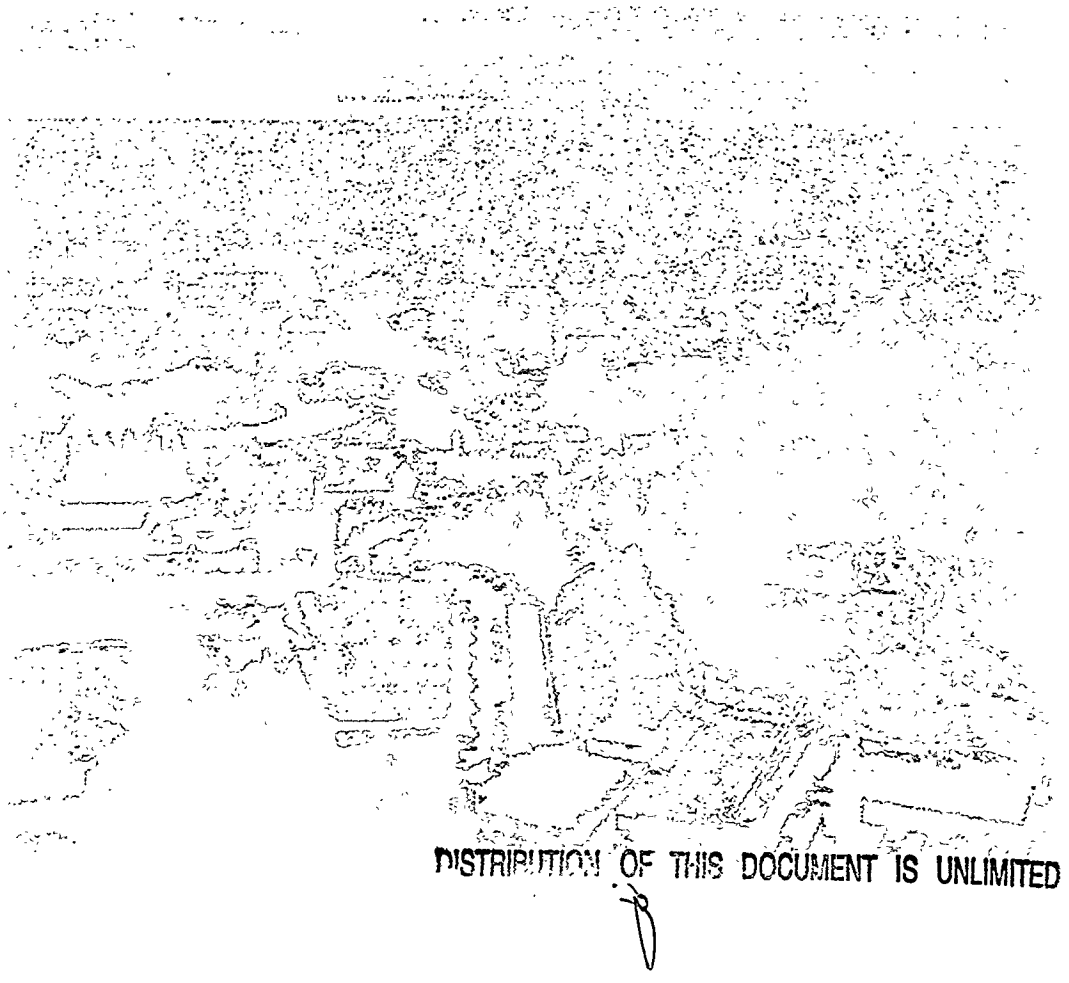

LBNL-39921
UC-414

Fluorescence Spectroscopy of Single Molecules at Room Temperature and Its Applications

Taekjip Ha

Department of Physics
University of California, Berkeley

and

Materials Sciences Division
Ernest Orlando Lawrence Berkeley National Laboratory
University of California
Berkeley, California 94720

December 1996

This work was supported by the Director, Office of Energy Research, Office of Basic Energy Sciences, Materials Sciences Division, of the U.S. Department of Energy under Contract No. DE-AC03-76SF00098.

Abstract

Fluorescence Spectroscopy

of Single Molecules

at Room Temperature and its applications

by

Taekjip Ha

Doctor of Philosophy in Physics

University of California, Berkeley

Professor Daniel S. Chemla, Chair

Abstract

We performed fluorescence spectroscopy of single and pairs of dye molecules on a surface at room temperature. Near field scanning optical microscope (NSOM) and far field scanning optical microscope with multi-color excitation/detection capability were built. The instrument is capable of optical imaging with 100nm resolution and has the sensitivity necessary for single molecule detection. A variety of dynamic events which cannot be observed from an ensemble of molecules is revealed when the molecules are probed one at a time. They include 1) spectral jumps correlated with dark states, 2) individually resolved quantum jumps to and from the meta-stable triplet state, 3) rotational jumps due to desorption/readsorption events of single molecules on the surface. For these studies, a computer controlled optical system which automatically and rapidly locates and performs spectroscopic measurements on single molecules was developed. We also studied the interaction between closely spaced pairs of molecules. In particular, fluorescence resonance energy transfer between a single resonant pair of donor and acceptor molecules was measured. Photodestruction dynamics of the donor or acceptor were used to determine the presence and efficiency of energy transfer Dual molecule spectroscopy was extended to a non-resonant pair of molecules to obtain high resolution differential distance information. By combining NSOM and dual color scheme, we studied the co-localization of parasite proteins and host proteins on a human red blood cell membrane infected with malaria. These dual-molecule techniques can be used to measure distances, relative orientations, and changes in distances/orientations of biological macromolecules with very good spatial, angular and temporal resolutions, hence opening new capabilities in the study of such systems.

Acknowledgments

I owe everything I have learned and done during my dissertation work to the following amazing people.

I thank Shimon Weiss, my research supervisor, for guiding me through the last four years both scientifically and personally. Innumerable hours of daily discussion with him have kept me keen with frontiers and new ideas in the field, and have steered our research into the most exciting new arena. His support and care for individuals in the teamwork made possible strong multi-disciplinary research activities encompassing physics, chemistry and biology.

I thank Thilo Enderle, postdoctoral fellow in the latter two years of my thesis work, for his enormous contribution to the entire project. He taught me innovative thinking and attention to details through many days and nights of shared laboratory works.

I thank Paul R. Selvin for providing his expertise and ideas on fluorescence spectroscopy and energy transfer which were indispensable for the success of the project.

I thank D. Frank Ogletree for his invaluable helps with the construction of near field scanning optical microscope and the data acquisition.

I thank Cathy Magowan for her help in the cell biology work.

I thank Daniel S. Chemla, my adviser, for his generous support to our project, tangible or spiritual. I learned many qualities of a successful scientist from him. He provided us with the lively and open environment to work in, and gave us chances to meet and communicate with many top scientists.

I thank David A. Botkin and Gregg Sucha for teaching me the basics of laser laboratory when I first joined the group.

I thank all of the above and Jennifer Glass, Jim Dunphy, Joy Liang, Sarah R. Bolton, Mary-Ann Mycek, Peter Kner, Gino Segre, Shimshon Barad, Uri Banin, Andreas

Schumacher, Rich Mazzoli, Joseph Orenstein, David Klein and M.Valeria Marquezini for making the life in the lab more enjoyable especially through lunch time and tea time.

I thank Eric Betzig, Jay Trautman, X. Sunney Xie, Pat Moyer and Steve Smith for help discussions about near field scanning optical microscopy and single molecule detection.

I thank Bill Knowlton and Kevin for their help with the electron beam evaporator.

I thank Professor Clarke, Professor Louie, Professor Attwood and Daniel for serving in my qualifying examination committee and dissertation committee.

I thank my parents in Korea for their endless love and trust.

I thank Su-A's parents for their support and love.

I thank Su-A, my wife of three years, for her deep love, patience and dedications.

I thank Su-A again for giving birth to Gloria Nayoung, my eight month old daughter who gives us joy day in and day out.

1. INTRODUCTION

The term single molecule spectroscopy (SMS) has been recently used to designate the investigation of optical properties (usually fluorescent) of individual molecules. Single molecule properties are very sensitive to the immediate local surroundings. Because one molecule is studied at a time, SMS is free from ensemble averaging, truly microscopic theory can be tested and many interesting and unprecedented observations can be made. In the last several years, single molecule detection and spectroscopy have seen an explosion of interests in physics, chemistry and biology. The motivations of this thesis are to understand the static and dynamic properties of single fluorescent molecules at room temperature, to study the interaction between two single molecules, and to develop SMS based, new tools for applications including in biology. In this chapter, we review molecular fluorescence in general, give a brief historical survey of single molecule detection and spectroscopy, and outline the remainder of this dissertation.

1.1. Brief introduction to molecular fluorescence

Fluorescence is the emission of photons from excited electronic singlet state to the ground state. Such transitions are "spin allowed", meaning that the change of spin orientation is not needed. The transition rates are typically 10^8 sec^{-1}, corresponding to fluorescence lifetimes near 10^{-8} sec. The lifetime is the average period of time a fluorophore remains in the excited state. Phosphorescence is the emission which results from transition between states of different spin multiplicity, normally from a triplet excited state to a single ground state. Typical phosphorescence lifetime ranges from milliseconds to seconds because such transitions do not have high transition rates.

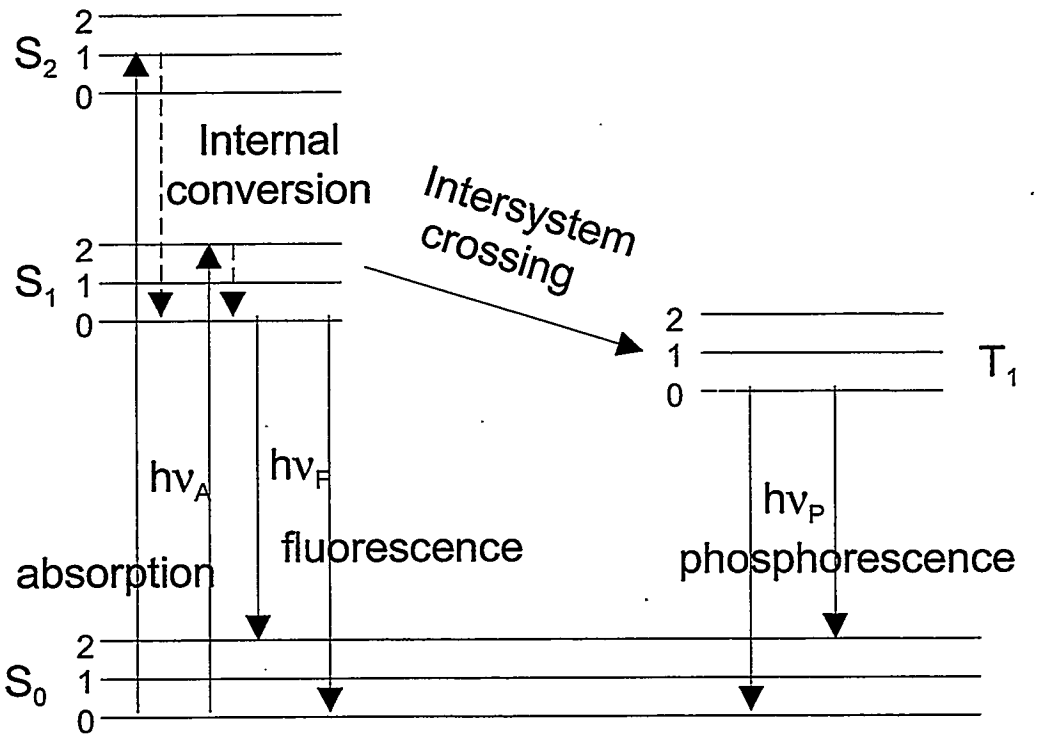

Fig.1.1. Jablonski diagram.

Jablonski diagram in Fig.1.1 illustrates the absorption and emission of photons by fluorophores or florescent molecules. The ground, first and second excited singlet electronic states are named S_o, S_1 and S_2, and the first excited triplet state is named T_1. In each electronic level, there are many vibrational levels denoted by 0, 1, 2... Because the energy difference between vibrational levels is about 150meV, much higher than the thermal energy, the molecules mostly populate the lowest vibrational level in the ground state in ambient conditions. The absorption of the photon $h\nu_A$ usually triggers the following sequence of events. The absorption brings the molecule to a higher vibrational level of S_1 or S_2. Molecules in the condensed phase rapidly relax to the lowest vibrational level of S_1. This process is called 'internal conversion' and occurs in 10^{-12} sec, and hence is complete prior to emission. Then, the fluorescence photon with energy $h\nu_F$ is emitted,

bringing the molecule to one of the higher vibrational levels of S_0, and finally the relaxation to the lowest vibrational level of S_0 occurs quickly in a time of the order of 10^{-12} sec. As a consequence, the absorption spectrum reflects the vibrational structure of the excited stated and the emission spectrum reflects the vibrational structure of the ground state. Molecules can make a non-radiative transition from S_1 to T_1. This transition is called 'intersystem crossing' and is much slower (100~1000 times) than the radiative transition from S_1 to S_0. The return from the triplet state to the ground state is accompanied by the emission of phosphorescence photon, and its decay rate is mainly dependent on the competing non-radiative decay rate due to various quenching mechanism. Not shown in Fig.1.1 but very important to note are the non-radiative decay paths through which the molecule can return to S_0 from S_1.

Energy losses between excitation and emission, or Stokes' shift, are universally observed for fluorescent molecules in condensed phase. One common cause of Stokes' shift is the rapid decay to the lowest vibrational level of S_1. Furthermore, fluorophores typically decay to higher vibrational levels of S_0, resulting in additional loss of energy. Stokes' shift is a most important character of fluorescence for applications to spectroscopy and microscopy because it can be detected selectively from excitation photons. It is very difficult to detect a small number of molecules in absorption because the corresponding change in transmission which has to be measured is extremely small. In fluorescent measurement, the signal is essentially background free and trace amount of molecules are easily detected. Ultimate sensitivity in such measurements is the optical detection of single molecules. This is the reason why single molecule detection investigators used fluorescence and not absorption.

Because of rapid internal conversion, the fluorophore reaches the lowest vibrational level of S_1 well before the emission no matter how it was excited, and the emission spectrum and lifetime are generally independent of the excitation energy.

Fluorescence lifetime and quantum yields are closely related quantities easily measurable. They often yield valuable information on the environment of the fluorophores. They are determined by two rate constants, k_r and k_{nr}. k_r is the radiative decay rate of the excited state S_1 and k_{nr} is the non-radiative decay rate due to all other radiation-less decay channels. The fluorescence quantum yield Q is the ratio of the number of photons emitted to the number absorbed. Since k_r and k_{nr} both depopulate the excited states, but only k_r is responsible for the emission of photon,

$$Q = \frac{k_r}{k_r + k_{nr}} \tag{1.1}$$

The fluorescence lifetime is defined as the average time the molecule spends in the excited state prior to the return to the ground state, and is in general on the order of 10 ns. In terms of k_r and k_{nr}, the lifetime τ is given by

$$\tau = \frac{1}{k_r + k_{nr}} \tag{1.2}$$

The quantum yield and lifetime can be modified by any factor that affect either of k_r and k_{nr}.

Fluorophores preferentially absorb photons with electric field vector along their transition dipole moment which has a defined orientation. Emission is also polarized along the emission transition dipole moment. If molecules are randomly oriented as in solution, the molecules with instantaneously oriented with their transition moment along the excitation field will be preferentially excited. If the rotation during the excited state lifetime is negligible, the emission will be partially polarized along the direction of the excitation field. Degree of polarization of the emission, r so called fluorescence anisotropy, is a sensitive measure of the solvent viscosity or of the rigidity of fluorophore's binding to macromolecules.

1.2. Brief history of single molecule detection and spectroscopy

The ability to detect trace amount of molecules in solutions or on surfaces has numerous important applications in many fields. Since the very first attempt to detect single molecules in liquids by fluorescence(Hirschfeld 1976), many applications to analytical chemistry and life sciences have been suggested. The first successful detection of a single fluorophore in a flowing aqueous solution(Shera et al. 1990), and the detection of a single dopant molecules in a host molecular crystal at cryogenic temperatures(Moerner 1989), introduced improved strategies for detection and background reduction. With the very recent advances in room temperature single molecule detection (SMD) and single molecule spectroscopy (SMS) of *immobilized* molecules at air-solid and liquid-solid interfaces, a whole new range of applications to various fields have emerged.

Single molecule detection and spectroscopy can be categorized in the following way.

- low temperature in solid
- room temperature diffusing/flow in solution
- room temperature immobilized or slowly diffusing: scanning & wide field

For SMD, a single molecule has to be isolated from other molecules. The optical transition of impurities in a solid has a huge inhomogeneous broadening. A strategy for SMD at low temperature in solid is to select spectrally each impurity molecule using very narrow line width. In room temperature SMS, separation is done spatially. The density (volume or area) of the sample is low enough so that only one molecule is under excitation volume at any point in time.

SMD in solid matrix was first achieved at liquid helium temperature from impurity molecules at crystalline or polymer matrix. Individual molecules have extremely narrow line width and molecules with slightly different resonance frequencies due to different environments can be frequency-resolved with high resolution laser spectroscopy (Moerner 1989). Fluorescence excitation spectra, where the total emission is monitored while the excitation energy of the laser is scanned, show easily identifiable narrow peaks that are attributed to single impurity molecules(Orrit and Bernard 1990). The line width of the peak (<10MHz) is quantum limited, that is, it reaches the minimum value allowed by the lifetime of the optically excited state. Many spectroscopic studies of the local environment can be performed on these systems because these narrow lines are extremely sensitive to local perturbations. For example, it has been possible to observe temperature dependent dephasing (Ambrose et al. 1991), optical saturation (Ambrose et al. 1991), Stark effect (Wild et al. 1992), pressure induced effect (Croci et al. 1993), spectral diffusion (Ambrose and Moerner 1991), spectral hole burning (Basche and Moerner 1992), photon bunching (Orrit and Bernard 1990), photon anti-bunching (Basche et al. 1992), quantum jumps(Basche et al. 1995), magnetic resonance of a single molecular spin (Kohler et al. 1993; Wrachtrup et al. 1993a; Wrachtrup et al. 1993b). While all these beautiful experiments are possible for low temperature SMS, only a handful of guest-host system (~10) satisfy the stringent requirements for SMD, and the necessary low temperature preclude any practical applications in biology.

The first SMD at room temperature was done for molecules in a flow cell (Shera et al. 1990). Bursts of molecular emission are attributed to single molecules and autocorrelation function measured from photon bursts yielded on information on transit time of the molecule through the excitation volume and intersystem crossing parameters. The radiative lifetime was measured from a single burst(Wilkerson et al. 1993). Nie et al. demonstrated SMD with superior sensitivity from diffusing molecules in the excitation volume of the confocal microscope (Nie et al. 1994).

The first SMD of immobilized molecules was demonstrated independently by Betzig et al. (Betzig and Chichester 1993)and Ambrose et al(Ambrose et al. 1994b) using near-field scanning microscope(NSOM) (Betzig and Trautman 1992; Lewis et al. 1984; Pohl et al. 1984),. Density of emitting spots that matches the nominal density of molecules and the sudden stop of emission were advanced as proofs for single molecule origin. In addition, Betzig showed strong polarization dependence of both the absorption and the emission arising from a single dipole. It is noteworthy in these experiments, single molecule spots with doughnut shapes or two crescent shapes were observed when the molecular dipole is perpendicular to the surface. This was attributed to the sampling of the electric field distribution near the tip by the molecular dipole. These works were immediately followed by the first spectroscopy of single molecules at room temperature. Trautman et al. measured the emission spectrum of single molecules with NSOM and observed spectral jumps (Trautman et al. 1994). Xie et al. (Xie and Dunn 1994) and Ambrose et al(Ambrose et al. 1994a) measured the fluorescence lifetime of single molecules using time correlated photon counting. In particular, they showed the perturbing effect of the metallic tip on the fluorescence lifetime by measuring the lifetime as a function of the tip position relative to the molecule. They found that the lifetime is longer when the molecule is located at the center of the tip and decreases as the molecule moves toward the edge of the tip. These observation were attributed to the quenching of the excited state by the metallic coating of the tip. Surprisingly, further investigations by Trautman et al. (Trautman and Macklin 1996) and Bian et al. (Bian et al. 1995) showed that the tip position dependence of the lifetime can change depending on the exact conditions. That is, for some cases, the lifetime is longer when the molecule is closer to the edge of the tip. Trautman et al. (Trautman and Macklin 1996) attempted to correlate the tip morphology and the position dependent lifetime. Bian et al. (Bian et al. 1995) found that the tip position dependence of the lifetime is determined by the distance between the tip and the molecule. They have calculated the lifetime as a function of tip

position in three dimension by numerically solving the classical dipole emission driven by its mirror image in the tip, and they could reproduce the experimental observations. Because of these tip induced effects, SMS with NSOM becomes complicated when the observation is made on quantities related to the fluorescence lifetime (~ns). Our group used NSOM-SMS to study the interaction between a pair of molecules adjacent to each other. In particular, we have measured the energy transfer between a donor molecule and an acceptor molecule by measuring the emission spectra of the pair as a function of time when the donor and the acceptor photobleached sequentially (Chapter 6).

SMS at room temperature was thought to be possible only with NSOM, because its small excitation volume limits the background signal from the substrates and enhances the signal. However, the fiber probe of NSOM itself proved to be a dominant source of the background, and several disadvantages of NSOM-SMS such as the difficulty of use, tip perturbation, and limited excitation intensity motivated efforts that led to another breakthrough of room temperature SMS: far-field scanning SMS.

In far-field scanning SMS, the NSOM tip is replaced by the focused laser spot. Superior signal to background ratio, unlimited excitation intensity, ease of use and the non-invasiveness make the far-field scanning SMS far more attractive than NSOM-SMS when the spatial resolution is not necessary (Trautman and Macklin 1996). Exploiting this non-invasiveness, Macklin et al. (Macklin et al. 1996) measured the fluorescence lifetime and the emission spectrum of a single molecule simultaneously and found a strong correlation between them. In addition, they found that the lifetime is strongly dependent component of the dipole moment normal to the air-polymer interface. We have used the high excitation intensity of far-field SMS to observe individual quantum jumps of a single molecule to the metastable triplet state(Ha et al. 1996f). By utilizing excitation polarization modulation, we also observed and identified many different single molecule events: dark state, spectral jump and rotational jumps (Ha et al. 1996c) (see Chapter 5). Xie et al. studied spectral jumps of single molecules by measuring the emission spectrum

with short integration time(~100ms) and found two different classes of spectral jumps with disparate time scales (Lu and Xie 1996).

Advantages of SMS on immobilized molecules are: 1) Same molecule can be studied as long as it stays active. 2) Therefore, various spectroscopic techniques can be applied to obtain far richer information than is possible from diffusing molecules in solution. 3) Imaging technique can also be used to obtain spatial information.

Perhaps the most challenging way of doing SMD at room temperature is the wide field SMD. A large field of view (~100μm) is excited with a laser beam and the emission is mapped in parallel by a CCD camera. Because of the parallel nature, the auto-fluorescence from the optical elements inside the microscope cannot be rejected as in the case of far-field scanning SMS and careful rejection of that background is necessary. By a careful selection of objectives, filters and lenses, single fluorescent molecules slowly moving at the glass-water interface were detected in the wide field geometry (Funatsu et al. 1995; Sase et al. 1995; Schmidt et al. 1996). Further reduction of the background was achieved by exciting molecules in the total internal reflection geometry. With these wide-field SMD techniques, biological applications were demonstrated. Individual ATP turnovers by single myosin molecule(Funatsu et al. 1995), individual actin filaments sliding over heavy meromyosin(Sase et al. 1995) and the sliding motion of single kinesin molecules along microtubules(Vale et al. 1996) were observed with video rate (30 ms) time resolution.

Advantages of wide field SMS vs. scanning SMS on immobilized molecules are: 1) Measurement is done in parallel such that an image can be taken in a short time. Real time observation with video rate time resolution is possible. 2) Moving molecules can be tracked easily. Trajectories of many molecules in the field of view can be found simultaneously.

Unique advantages of scanning SMS over wide field SMS are: 1) Spectroscopic techniques can be applied easily. 2) Better signal to noise performance is possible because

the background due to optical elements can be rejected using the confocal geometry. It is also conceivable of doing spectroscopy on moving molecules by combining it with a tracking tool.

Recently, SMD with two photon absorption was demonstrated using confocal microscope in solution at room temperature (Mertz et al. 1995) and also for low temperature molecules in solid (Plakhotnik et al. 1996). Two photon SMD has practical merits. Since long wavelength excitation can be used, background due to auto-fluorescence of the substrate and optical elements can be substantially reduced. Many natural fluorophores require ultra-violet excitation for single photon absorption, and extremely care need be taken in the selection of optical elements for the measurement. With two photon absorption, UV fluorophores can be studied with regular, high quality optical elements available.

The advance of SMS motivated recent studies of single quantum systems of different kind, namely semiconductor nanocrystals. II-VI compound nanocrystals of nanometer diameter such as CdSe, CdS, ZnSe nanocrystals can be synthesized with very good control over size distribution and surface terminations. Single nanocrystals were measured with far-field microscope both at room temperature (Nirmal et al. 1996) and low temperature and novel effects such as photo-ionization and spectral jumps were observed.

1.3. Outline of the rest of the dissertation

We have used both near-field scanning optical microscope and far-field scanning optical microscope to study immobilized single molecules at the air-solid interface. In chapter 2, *Instrumentation*, we briefly review the general NSOM and describe our specific implementation. Optical excitation (near-field and far-field) and detection

scheme and data acquisition scheme are also discussed. In chapter 3, *Near-field high resolution imaging*, we show three different contrast mechanisms: transmission, topography, and fluorescence. In particular, we present the co-localization study of parasite and host proteins in malaria infected red blood cell membrane using dual color excitation/detection of fluorescence (Enderle et al. 1996). In chapter 4, *Single molecule detection*, single molecule imaging and emission spectroscopy are demonstrated. Signal level expected from a single molecule is calculated from available optical data of the molecules studied and is in good agreement with the measured signal intensity. Several proofs of single molecule origin are also given. In chapter 5, *Single molecule dynamics*, we report observations of many dynamical processes of single fluorophores on a dry surface seen at room temperature. These include spectral jumps and dark states that are often correlated, first room temperature observation of quantum jumps (Ha et al. 1996f), and rotational jumps due to desorption and readsorption to the surface (Ha et al. 1996c). In chapter 6, *Dual molecule spectroscopy*, two techniques using a pair of molecules are developed (Ha et al. 1996d). First observation of energy transfer on a single pair of donor and acceptor molecules (single pair fluorescence resonance energy transfer or spFRET) is reported along with its possible applications in biochemistry on single molecular level (Ha et al. 1996e). Another technique with two molecules that can give nanometer differential distance resolution (Non-resonant dual color imaging) is proposed along with very preliminary results. In chapter 7, *Future directions*, the proposals for future works along the main theme of the dissertation are presented. Finally, Appendix A describes the automated positioning mechanism that we developed for SMS (Ha et al. 1996a).

2. INSTRUMENTATION

2.1. Introduction

Recently, scanning probe microscopies (SPM) have found their way into biological studies, providing high resolution structural information. These techniques are based on the interaction between the specimen and a sharp tip in its close proximity. DNA, proteins and many other biological molecules were successfully imaged with atomic force microscopes (AFM)(Hansma et al. 1995). Of major concern for biological applications is their invasiveness. Since the probe tip is brought very close to the sample (usually a few Å for contact or tapping-mode AFM), the integrity, functionality, structure and chemical properties of the molecules under study may be altered.

Another member of the SPM family is the near-field scanning optical microscope (NSOM) (Betzig and Trautman 1992; Lewis et al. 1984; Pohl et al. 1984), which is based on a probe consisting of a very small (sub-wavelength) aperture. It is usually made by pulling and tapering a single mode optical fiber to an end diameter of less than 100nm and coating its side walls with aluminum. Sample is scanned close to the probe (5~10nm) to form images of various contrasts with super-resolution down to 12nm (Betzig and Trautman 1992). Since the tip-sample distance regulation scheme, called shear force feedback (Betzig et al. 1992; Toledo-Crow et al. 1992), is employed, topography information is obtained simultaneously with the optical information. The NSOM tip usually hovers over the sample much higher than tapping-mode AFM (the most common approach for biological imaging with SPM), and therefore introduces less perturbation to the sample under study. This of course comes at the expense of attainable resolution. However, since NSOM is an optical technique, it has the unique capability to bring a vast

array of optical spectroscopic techniques into nano-scale microscopy. As will be shown in Chapter 6, the spectroscopic capabilities of NSOM, combined with dual-color labeling techniques, can *regain* the needed molecular resolution, and thus offer a relatively non-invasive, true molecular probe.

Although relatively non-invasive to the biological macromolecule, the near-field probe does perturb the fluorescence of a single fluorophore(Ambrose et al. 1994b; Bian et al. 1995; Trautman and Macklin 1996; Xie and Dunn 1994). If higher degree of non-invasiveness is required, far-field (wide-field and confocal) microscopies can be used. To reject out-of-focus light, laser scanning confocal microscope (LSCM)(Pawley 1995) uses a pinhole that is confocal with the diffraction limited illumination spot on the specimen. A series of scanning images can be collected for different focal planes to generate a three-dimensional representation of the specimen. The confocal microscope is widely used for observing physiological reactions and the shapes of living cells. Recently, a few groups demonstrated single molecule spectroscopy with LSCM (Macklin et al. 1996; Trautman and Macklin 1996). The main advantages over NSOM are the non-invasiveness and the ease of use. However, the spatial resolution of LSCM is inferior to the one attainable with NSOM.

A versatile experimental set-up which is based on a conventional up-right fluorescence microscope was built. A sample stage piezo scanner, a NSOM head and a pinhole in the image plane provide near-field and confocal capabilities in addition to conventional wide-field imaging. The NSOM is an add-on: far-field reflection microscopy can be performed on the sample while the head is in place, examining the same field of view in the near-field and in the far-filed.

2.2. Near-field scanning optical microscope (NSOM)

2.2.1. Introduction to NSOM

Conventional lens-based optical microscopy has enjoyed hundreds of years of success, and variety of contrast mechanisms has been developed that enable the detailed study of biological or physical specimen with sub-micron spatial resolution. Since the diffraction of photons fundamentally limits the resolution of the conventional optical microscopy, alternative tools such as electron microscopy, scanning tunneling microscopy and atomic force microscopy have been developed to obtain structural information with near atomic resolution. However, these high resolution microscopy tools are often limited in the applicability because of stringent requirements on the sample preparation and the invasiveness to the specimen, and the wealth of optical contrasts is not directly applicable. Near-field scanning optical microscopy bridges the gap effectively and provides the 12nm spatial resolution while retaining much of the advantages of conventional optical microscopy. The field of NSOM is young (since 1984), and the pioneering works of a few investigator stimulated the rapid growth of the field. Especially, the development of single mode fiber probe and shear force feedback ignited numerous applications to solid state physics (Buratto et al. 1994a; Buratto et al. 1994b; Gregor et al. 1995; Grober et al. 1994; Harris et al. 1996; Hess et al. 1994), polymer science (Blatchford et al. 1996; Higgins and Barbara 1995), single molecule spectroscopy (Ambrose et al. 1994a; Ambrose et al. 1994b; Betzig and Chichester 1993; Bian et al. 1995; Ha et al. 1996c; Ha et al. 1996e; Meixner et al. 1995; Trautman and Macklin 1996; Trautman et al. 1994; Xie and Dunn 1994), and biological imaging (Enderle et al. 1996; Vanhulst and Moers 1996).

Diffraction which limits the resolution of the conventional optical microscopy is a far-field effect. NSOM attempts to overcome this limit by performing optical measurements

in the near-field of a sub-wavelength light source. Consider the case of a sub-wavelength aperture on an opaque screen depicted in Fig.2.1. When the light is incident on one side of the screen, a small number of photons will pass through the aperture, and they will remain confined within the aperture size up to a certain distance. Theoretical treatments of the problem show that the near-field range is comparable to the aperture diameter **a**, after which the light diverges exponentially (Betzig et al. 1986). Therefore, if the sample is brought within the distance $\mathbf{h} < \mathbf{a}$, optical measurement with super-resolution can be achieved. Unlike in the conventional optical microscopes where all the points in the sample plane are transferred to the image plane in parallel, the image has to be obtained serially by scanning the aperture or the sample.

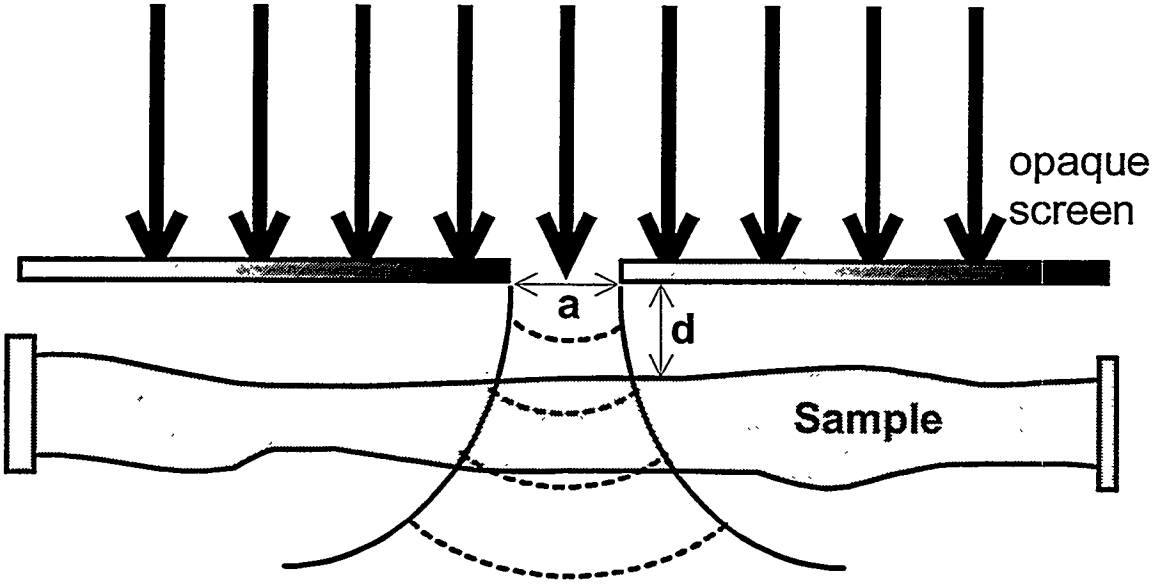

Fig.2.1 Concept of the near-field scanning optical microscope.

The theoretical maximum resolution of such aperture based NSOM is 50nm, and is determined by the finite skin depth of the aluminum, the best material for the opaque screen for the visible light. Because of the finite skin depth, a finite thickness of aluminum should be used to form the opaque screen through which the transmission of the incident light decreases exponentially with the screen thickness. Because of the finite

thickness of the screen, the aperture itself is an evanescent wave guide through which the transmission decreases also exponentially with the screen thickness. As the aperture size gets smaller, the attenuation through the aperture increases, and finally at a ~ 50nm, the transmission contrast between the aperture and the screen disappears (Betzig et al. 1986).

Transmission through the aperture in an ideal, infinitely thin, perfectly conducting screen was evaluated by Bethe (Bethe 1944), and is proportional to $\mathbf{a}^6/\lambda^4$ where a is the aperture diameter and λ is the wavelength of the light source. Increased resolution comes at the penalty of significantly decreased throughput, and **a** has to be decided based on the experimental requirements for each experiment.

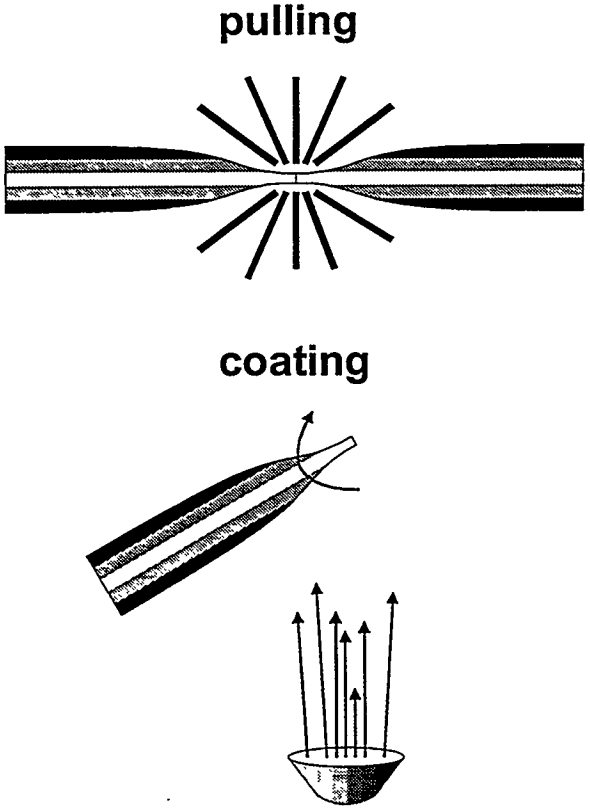

Fig.2.2 Making of a NSOM tip.

An aperture in a screen is not an ideal probe for NSOM because only a very flat sample could be brought close enough to the aperture to utilize the near-field effect. Practical probe is usually made by pulling and tapering a single mode optical fiber to an end diameter of less than 100nm and coating its side walls with aluminum (Fig.2.2). Other alternative probes are also available even though not as successful.

The maximum output power from a NSOM tip is also limited by the finite conductivity of the aluminum rather than by the available laser power because the aluminum absorbs slightly at the visible wavelength and it will result in the overheating and melting of the tip for higher input intensity. A few nano watts of power is obtainable from 50nm aperture and more for bigger apertures.

During the scan, the distance between the sample and the tip needs to be maintained below the aperture size, and this can be achieved by a variety of methods, the most successful of which is the shear force feedback (Betzig et al. 1992; Toledo-Crow et al. 1992). We have built an aperture based NSOM using a single mode optical fiber, and used shear force feedback for distance regulation. More discussion of tip fabrication, characterization, shear force feedback and scan head design will follow.

2.2.2. Tip fabrication and characterization

History of Near-field probes

The first demonstration of NSOM were done in two groups in Cornell (Lewis et al. 1984) and IBM Zurich (Pohl et al. 1984) independently. Later on, Cornell group developed the near-field probe based on micropipette (Harootunian et al. 1986), glass tube of 1~2mm diameter pulled to a sharp tip. Micropipettes are widely used for biology in handling micro-sized specimens. A commercial micropipette puller equipped with tungsten coil for heating the pipette was used to pull the tip and the tip was aluminum coated to eliminate far-field contribution leaking from the side of the tip. Optical fiber was used to deliver laser light into the micropipette. Since the optical fiber has a outer diameter of about 100μm, it can not fit into the micropipette completely, and the light has to propagate through along the unguided portion of the micropipette until it reaches the apex of the tip. This results in significant loss of the input radiation, and the total throughput is too low for any significant spectroscopic applications.

This barrier was overcome when Betzig et al. developed a NSOM tip based on single mode optical fiber (Betzig et al. 1991). Similar micropipette puller equipped with CO_2 laser was used to pull a single mode fiber into a sharp tip and the tip was coated with aluminum. Since the light can be guided within the tapered region of the fiber all the way

down to the region where the dimension becomes comparable to the wavelength, the main loss occurs only within the sub-wavelength portions of the fiber. Throughput of 1 photons out of 10^4 incident photons is possible and output level of 10^{11} photons/sec is achieved for 80nm aperture. This is high enough for most of the linear spectroscopy conceivable, and even for single molecule spectroscopy (Ambrose et al. 1994a; Ambrose et al. 1994b; Betzig and Chichester 1993; Bian et al. 1995; Ha et al. 1996c; Ha et al. 1996e; Meixner et al. 1995; Trautman and Macklin 1996; Trautman et al. 1994; Xie and Dunn 1994).

Meanwhile, there have been alternative probes proposed and developed for NSOM. Perhaps the most interesting alternative approach is the apertureless near-field microscope of Zenhausern et al. with which 50nm resolution barrier for NSOM can be surpassed and extended to about 1nm (Zenhausern et al. 1995; Zenhausern et al. 1994). It uses a sharp tip as a tiny scattering source and interferometric detection of the scattered light which is spatially modulated by the strong dipole-dipole coupling between the tip and the sample. They also demonstrated resonant optical scattering spectroscopy with 5nm resolution (Martin et al. 1996). Although its contrast mechanism is not well understood and is not as versatile as aperture based NSOM, the super-high optical resolution could find many interesting applications.

Selection of fiber

For maximum throughput, a single mode fiber designed for the laser wavelength should be used to make sure that only the lowest mode of propagation is possible. Main idea is to deliver the laser light without loss until the point where the fiber diameter becomes smaller than the wavelength. We used Newport or SpecTran 515nm fiber for Argon laser lines and 568nm line of Kr-Ar laser. 630nm fiber may be used for Argon laser lines as well, but the fiber needs to be stressed or coiled to suppress higher order modes.

Fiber pulling

To pull the fiber (Valaskovic et al. 1995), we have used P-2000 micropipette puller with a built-in CO_2 laser (Sutter instrument, factory-modified for fibers). Plastic jacket at the central 1cm portion of a fiber 2m long is removed by soaking it into Acetone or Chloroform. Then, the fiber is securely mounted on both pulling bars with the stripped part centered. Fiber is pulled slowly on both pulling bars after the CO_2 laser is turned on to heat up a few millimeter of the fiber. Once the fiber starts to melt and the pulling reaches a pre-set velocity, the laser is turned off and the final hard pull is applied after a certain delay. Two fiber probes are produced from each pull and they can be pre-screened by looking under an optical microscope.

Shape, taper angle and taper length are very effective criteria for screening out bad tips. If the taper length is too long or the taper angle is too small, the light has to propagate for longer distance until it hits the final barrier, the sub-wavelength region, and this barrier will also be longer. If the taper length is longer than 1mm, the throughput is much smaller than necessary for single molecule detection and the tip can be discarded without further processing. The shape is also important, and one generally wants to have short taper without big curvature. There are five programmable parameters of the puller that can change the pulling result: HEAT, FILAMENT, VELOCITY, DELAY and PULL. HEAT is the intensity of the CO_2 laser. FILAMENT is the dithering amount of the laser along the length of the fiber and is important only for micropipettes but not for fibers. VELOCITY dictates when to stop the heating and start the final hard pull by specifying the critical velocity of the pulling bars as the fiber starts to melt. DELAY is the time delay between the laser turn-off and the final hard pull where DELAY=128 means no delay. PULL is the strength of the final hard pull. Our working parameters along with usable ranges for 515nm fibers are following.

Table 2.1. Typical parameters for single mode fiber pulling

HEAT	FILAMENT	VELOCITY	DELAY	PULL
330 (±40)	0 (±0)	20 (±4)	127 (±2)	120 (±15)

To obtain shorter taper length and bigger taper angle, HEAT, PULL and VELOCITY have to be decreased while the delay has to be increased. However, in the extreme cases, the fiber may not pull at all because the final pull is applied when the fiber is too cold. If the shortest possible taper length is sought, the reproducibility drops because the pulling conditions are inherently less stable in that part of the parameter space. Therefore, a compromise has to be made between the short taper and the reproducibility.

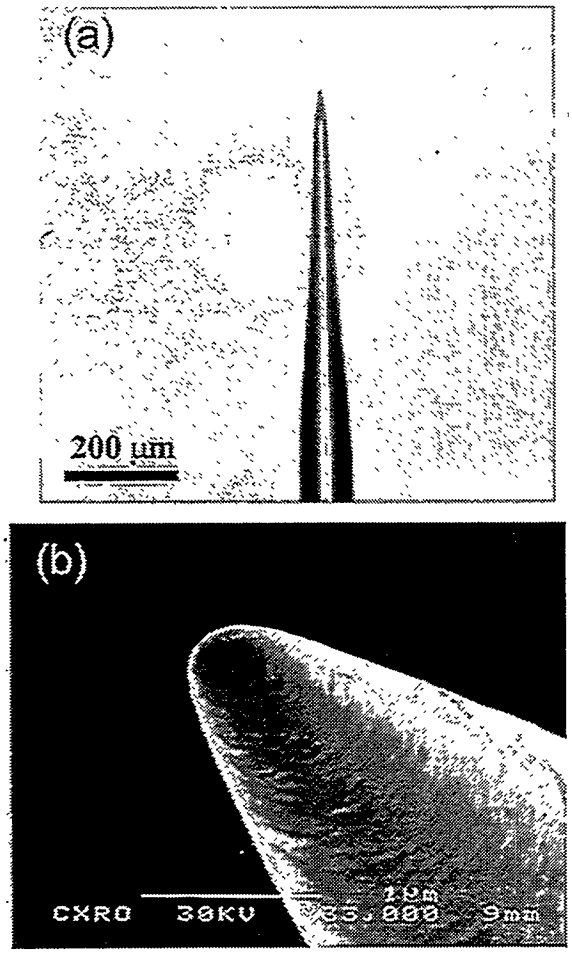

Fig.2.3 Optical and electron micrographs of tips. (a) optical micrograph of freshly pulled, uncoated fiber. (b) SEM image of aluminum coated fiber.

Additional test of the pulling process is coupling light into the fiber. The light coming out of the tapered end of the fiber has to be diffraction limited. Otherwise, the loss before it hits the diffraction limit will be unacceptably large. If the test is positive for one fiber, both fiber tips from the same pull are accepted for further processing. It takes about half an hour to pull 8~10 tips when the reproducibility is good.

Aluminum coating of tip

The end face of the fiber tip is flat with a diameter about 100nm. The side of the tip needs to be coated with aluminum to obtain true sub-wavelength aperture of that diameter (Valaskovic et al. 1995).

The coating is done under a moderate vacuum (~10^{-6} torr) in an electron beam evaporator. At least 100nm thick coating is necessary to guarantee complete block of the light leakage through the side wall. To obtain a 100nm thick coating, 310nm of aluminum is deposited while the tips are rotated using an external dc motor. To avoid coating the very end of the tip, the tips are tilted by 30° with respect to the evaporation direction. Up to eight tips can be coated at one time under almost identical conditions. Coating quality strongly depend on the evaporation rate and the cleanness of the fiber tip. For aluminum, fast evaporation rate as high as 10nm/sec is necessary to avoid clumping. However, if 310nm of aluminum is deposited at such a high rate, the coating quality suffers because the strain is not relieved during the coating. Best result could be obtained when the coating is done in two identical steps of 50nm coating with an interruption during which the tips are cooled down. Dust particles collected on the bare fiber after the pulling can adversely affect the coating, and it is essential to avoid exposing it to the air extensively before coating. Therefore, fiber tips have to be put into vacuum no later than 1 hour after the pulling. Optical micrograph of a tip before coating and SEM picture of a tip after the coating are shown in Fig.2.3.

Mounting of tip

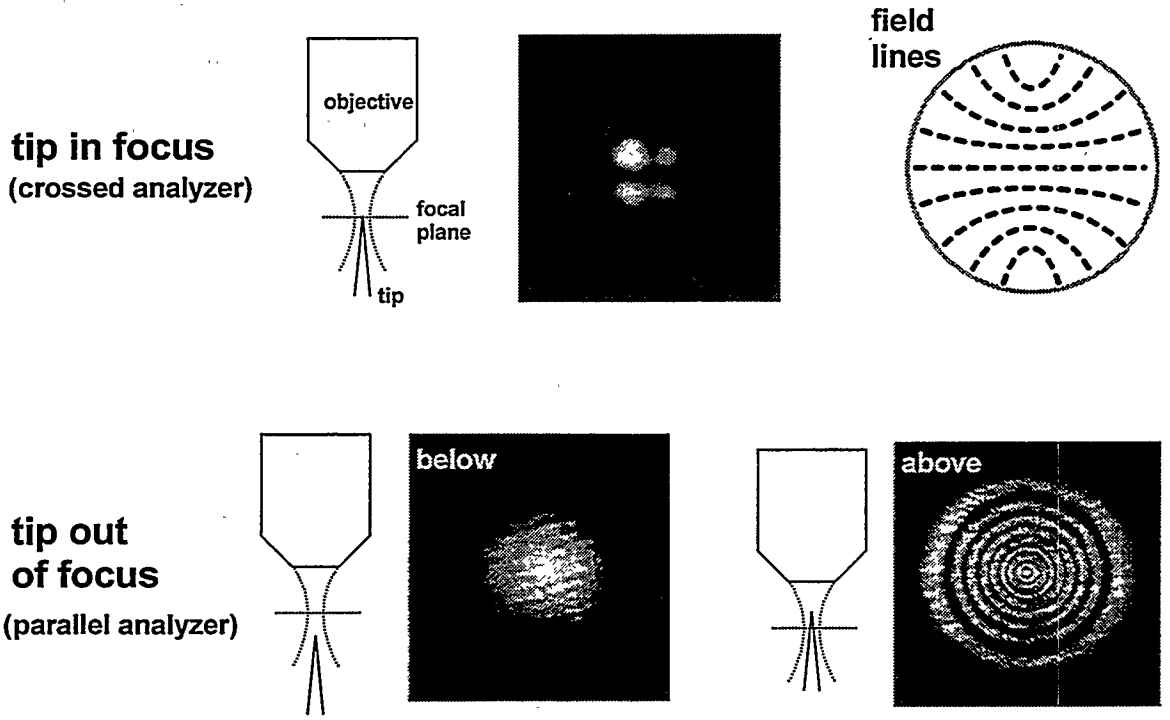

Fig.2.4 Quality control of the near-field tip. Tip with ideal morphology displays a single spot in focus and many concentric rings slightly out of focus. When a cross analyzer relative to the linear polarization is placed, four spots on the corners are seen. Field lines at the aperture seen from above could result in these four spots.

Once coated with aluminum, the fiber tip is mounted inside a glass capillary tube using a silver paint for easy handling and to define the attachment point of the tip to the tube for shear force feedback. Silver paint also serves to block back scattered light from entering the sample plane.

Tip diagnostics

There are a few more tests for these end products. Laser light is coupled into the fiber and the photons emanating from the tip are observed using an optical microscope from above. First, there should be only one spot for any incident polarization. Second, the throughput should be as high as $10^{-4} \sim 10^{-5}$ for single molecule detection. If the throughput is too low, higher input intensity has to be used to get the necessary intensity for SMD, and occasionally this leads to the overheating of the fiber (the reflectivity of aluminum is not hundred percent and about 2% of light is absorbed.) that results in the

destruction of the tip (Stahelin et al. 1996). Third, the background luminescence from fiber polymer jacket and silica-aluminum interface and Raman scattering from the Si-O stretch band in the fiber itself have to be sufficiently low. More than 50% of the fibers are rejected because they fail this test and after many attempts to improve the yield, we have not found a reliable way of reducing this background. Fourth, the resonance of dithering should be strong enough. This condition can be met very well by tightly attaching the tip to capillary tube and the capillary tube to the tip holder. Lastly, polarization quality of the light coming out of the tip is checked (Fig.2.4). An analyzer is place inside the optical microscope and a quarter-waveplate and a half-waveplate are adjusted to achieve the cross polarization that gives the minimum transmission past the analyzer. If the extinction better than 100 is achieved, usually the tip has near perfect morphology as is verified by the high quality single molecule imaging. For an ideal tip, the spot seen on the microscope is a point in focus and many concentric rings when defocused. Interestingly, if an analyzer is placed for the orthogonally polarized light, four symmetric spots can be seen from an ideal tip. Only after a tip passes all these tests, the experiment can begin. Shelf lifetime of the tip after coating can be a few weeks without noticeable degradation, so good tips can be used over and over again unless they are damaged during the experiment. One other useful characterization tool of the near-field tip is to image the aperture with SEM (scanning electron microscope). We used SEM only during the initial stage of finding the operating point for pulling and coating, and other tests described above proved to be adequate for SMD experiments.

2.2.3 Shear force feedback implementation

NSOM demands that the sample under investigation has to be in the near-field of the tip because the resolution quickly deteriorates as the sample is moved away from the

aperture. Since samples in general have topographic features, a distance regulation scheme has to be implemented. Such a scheme should have following elements. 1) There should be a physical observable that is a measure of the sample-tip distance. 2) That observable has to be detected. 3) The detected signal containing the distance information should be converted so that feedback circuit can compare it with a set point and generate the error signal. 4) The error signal has to be applied to the distance adjusting mechanical stage, usually as voltage on the piezoelectric tube.

Review of feedback schemes in NSOM

In the shear force feedback scheme developed in 1992 (Betzig et al. 1992; Toledo-Crow et al. 1992), the dithering amplitude of the tip, laterally driven at its lateral resonance frequency, is the physical observable. Dithering amplitude drops as the tip approaches the surface due to tip-surface interaction, and this amplitude or the associated properties are measured either optically or using other non-optical techniques (Hsu et al. 1995; Karrai and Grober 1995; Leong and Williams 1995). In the case of optical detection, the amplitude of dithering is directly measured and it becomes zero when the tip is in contact with the surface. Therefore, the conversion of the signal and the comparison with the set point is straightforward for optical detection. In the case of non-optical detection, the dithering amplitude is not directly measured, and the signal in-contact is not known a priori. Approach curve needs to be taken to determine the signal level in-contact and the set point has to be determined accordingly. However, its simplicity makes it a attractive option for NSOM in liquid (Moyer et al. 1995; Muramatsu et al. 1995). More widely used detection scheme is the optical detection. Applying error signal to the distance control stage, commonly piezoelectric material after amplification with proper gain and time constant is performed, is in general common to all different approaches of distant regulation.

Before shear force feedback was developed, NSOM operated either without any feedback, or in hybrid modes with other existing scanning microscopy techniques. Optical feedback, based on the interference of the light between the tip and the sample, has been used, and the optical contrast itself is the optical feedback . It does not work reliably for general samples because the signal strongly depends on the optical properties of the surface such as reflectivity rather than just the topography. Tunneling current was used for distance regulation as in STM by coating the tip with gold (Lieberman and Lewis 1993).

Tunneling feedback scheme requires a separation on the order of a few angstrom which is an overkill for NSOM where the separation can be as much as a few hundred angstrom, the attainable optical resolution. When the metallic tips is in such a close contact with the sample, the perturbative effect of the tip can be serious, and purely optical contrast is hard to obtain. For example, the metallic tip can quench the fluorescence of the sample completely when placed within a few angstrom. Also, the tunneling feedback requires a conducting sample, strongly limiting the range of samples that can be studied.

Hybrids between the NSOM and AFM have been demonstrated where the deflection of the cantilever with the built-in sample or tip is monitored or the NSOM fiber itself is bent to form a cantilever like structure (Shalom et al. 1992; Vanhulst et al. 1993a; Vanhulst et al. 1993b). Although the well characterized AFM feedback scheme can be used, the optical quality is sacrificed because of the high degree of loss in photon flux for the bent tip and the difficulty of eliminating far-field contributions for the modified AFM tip. Preliminary results were obtained with the above alternative feedback schemes, but no application beyond the proof of concept has been demonstrated. In fact, the only scheme that yielded significant scientific information is the "no feedback scheme". For example, NSOM study on atomically flat, cleaved semiconductor was performed to probe

the nature of local luminescent centers, without any feedback because of the flat surface and the stability at the low temperature (Hess et al. 1994).

Implementation of shear force feedback with optical detection

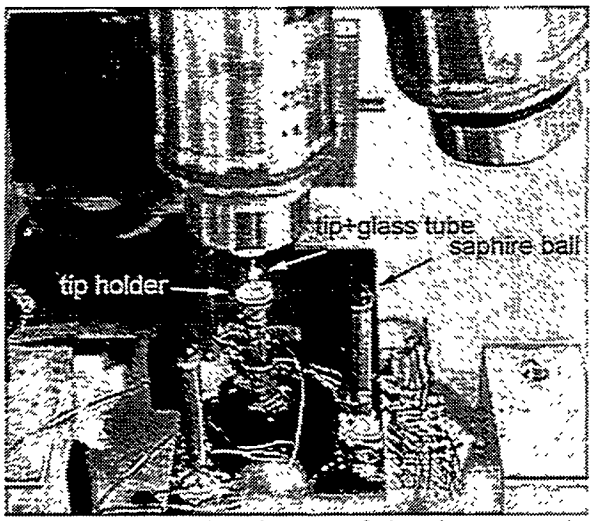

Fig.2.5. Zoom-in picture of the tip area. Tip is glued into a glass tube that is in turn spring loaded in a tip holder. Sapphire balls are glued to the outside piezotubes.

We have adopted the shear force feedback method for NSOM and implemented it in a simple way. Even though our scheme does not have the ultimate sensitivity more sophisticated implementations provide, it is very easy to use and does its main job - not to crash the tip during rapid scanning on a highly corrugated samples - well enough that we describe it briefly with pros and cons.

We glue the fiber tip inside a 1cm long glass capillary tube with a silver paint and about 1mm of the tip sticks out of the capillary tube. This part of the tip vibrates with a resonance frequency between 20kHz and 100kHz when the dithering voltage is applied to the piezotube holding the capillary tube (Fig.2.5). Q factor of the resonance strongly depends on the strength of holding at a number of points: silver paint, spring loaded brass piece holding the capillary tube and the glue that holds the brass piece to the piezotube. The resonance frequency can be most easily found by looking at the light coming from the tip from above using an optical microscope. At the optimum resonance with 5 Volt rms dithering voltage, the tip makes 10-20 micron elliptical motion. The ellipticity, the angle of the ellipse and the amplitude are very sensitive to the dithering frequency and the point of attachments. Usually, the frequency and the point of attachment are adjusted until the tip motion is maximum and mostly linear along the y-direction because the infrared laser light for shear force detection is

incident along the x-direction. For actual shear force feedback, the dithering voltage is reduced down to 5 mV rms with 10 to 20nm dithering amplitude. When the tip is brought close to the surface of the sample, the amplitude of the vibration drops due to the interaction with the surface. The effect can be seen easily as far as 10nm from the surface and at around 5nm separation, the amplitude drops to the half of the unimpeded value. The distance is measured by taking an approach curve and the zero distance to the surface is defined as the position where the dithering amplitude drops to zero. These distances increases if the amplitude of the dithering increases, so the presence of the surface can be felt from farther away with bigger dithering motion (Gregor et al. 1996). As long as the required resolution in the topographic information obtained by shear force feedback scheme is not too high, the dithering may be increased in order to increase the average tip to surface distance. Perturbative effect of the tip on the sample as a function of dithering amplitude needs to be studied in order to evaluate the optimal dithering amplitude for each surface type. In general, the type of surface does not alter the shear force measurements significantly for metal coated fibers. However, for NSOM with uncoated fibers where both the excitation and detection are done through the tip, it was shown that the shear force imaging can yield wrong height information for different type of surfaces because the distance dependence of the shear force varies among different surfaces (Jalocha and Vanhulst 1995).

For optical detection of shear force signal, focused laser light on the side of the tip is used to detect the amplitude either looking at the scattered or diffracted light , or utilizing interferometer with the reflected light. We chose to look at the diffracted light with a split detector for differential measurement (See Fig.2.8). 2mW, temperature and power stabilized, 1.3μm laser diode with a pig tail output is used as a source (since most of our work involves photons in the visible wavelength range, we use Silicon detectors that are not sensitive to infrared laser light.) and bi-cell InGaAs photodiodes are used for the

detection. Laser light is focused with an 5cm focal length lens at about 200μm away from the end of the tip, and the detector is placed also about 5cm away from the tip. The laser light is incident parallel to the sample plane so that the location of the sample does not affect the signal when the tip-sample distance is out of the shear force range. Alternative approach is to bounce the laser beam off the sample plane at an angle, but in this case, the shear force signal cannot be measured when the tip is far way from the sample and the signal may be affected by the sample reflectance. Focusing lens is mounted on a adjustable mirror mount so that the optimal positioning of the beam is possible. The signal from two photodiodes are amplified and the difference between two signals is measured using a lock-in amplifier at the frequency of dithering. The sum of two signals is added to the difference signal with a adjustable ratio such that the dc offset can be zeroed out. We used the x component of the lock-in signal or $r\cos\theta$, because it is sensitive to both amplitude (r) and phase (θ) of the signal. The x signal, when the auto-phase is set, is positive and decreases as the tip approaches the surface. This behavior is opposite to that of tunneling current for STM where the tunneling current increases from zero as the tip approaches the surface. Therefore, the x signal is inverted and the dc offset is added such that the output to the STM current behaves as if it were coming from STM. For the feedback, the set point is normally chosen to be half the amplitude of unimpeded dithering. Gain and time constant

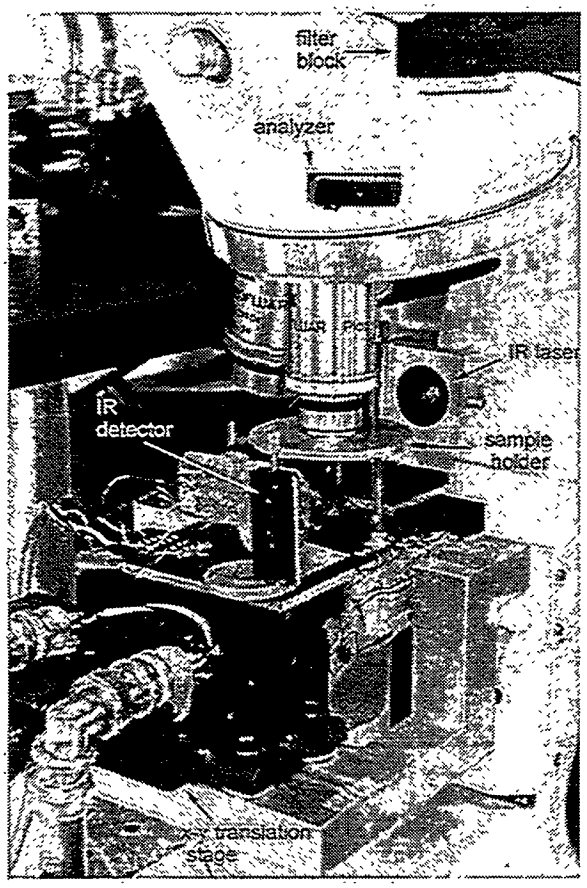

Fig.2.8. Scan head and collection optics.

of the feedback, set manually by the front panel of the scanning electronics, are very important for reliable feedback. When the feedback is slow (low gain and long time constant), the tip may crash more easily during the scan and even in stationary position, and the noise spectrum tells us that the mechanical vibration coupled through the oil immersion objective is not fully compensated by the feedback. If the gain is too high or the time constant is too long, the feedback loop enters oscillation with the tip literally banging on the surface. Usually, the bandwidth of the feedback is increased until the oscillation is about to start. For relatively flat samples of corrugations smaller than 100nm, the feedback can be done fast enough so that scan speed is rather determined by the integration time for the optical signal than by the feedback bandwidth. For samples with gigantic corrugations such as red blood cells, slow scan speed has to be used to avoid crashing into the cell.

2.2.4 Scan Head

To obtain images for any scanning microscopy, the sample or the probe has to be raster scanned relative to each other while the signal of interest is monitored. Because of its ease of use and the sub angstrom precision, the bending motion of piezoelectric tubes is widely used for scanning. In addition, the longitudinal motion of the tube can be used for distance regulation.

Scan head design

For fluorescence NSOM where efficient light collection and excellent background rejection is required, the most essential consideration for the scan head design is not to scan the tip but to scan the sample. Efficient rejection of backgrounds, coming from auto-fluorescence of substrate and optical elements, is usually achieved by putting a pinhole at

the image plane or by using a small area detector such as APD. In both cases, the scheme of scanning the tip does not work unless entire optical system scans together.

Since it is hard to isolate the entire optical system from external vibration other than using optical table, it is important to make the scan head compact and stiff. Micrometers may be used to coarsely position the sample relative to the tip in x, y and z axis, but it will result in a bulkier scan head where stability is sacrificed. Therefore, we adopted the three piezo inertial walker design by Besocke (Frohn et al. 1989) for the coarse x, y motion and z approach. For example, to move the sample in x direction, slowly increasing voltage is applied to all x electrodes of the three outside piezotubes during which the sample follows the motion of the piezotubes. Then, the voltage suddenly returns to the original value and the piezotubes return to the original position. Because of the inertia, the sample holder does not follow the piezotubes and this results in the net translation of the sample. Similar arguments hold true for both y and z motion with the specially designed sample holder with slopes on the bottom (Fig.2.6). Especially, the rotation of the sample holder that can also be achieved by appropriately applying voltages to outside piezotubes (See Fig.2.7 and descriptions later), will result in the vertical motion of the sample holder because of the slopes.

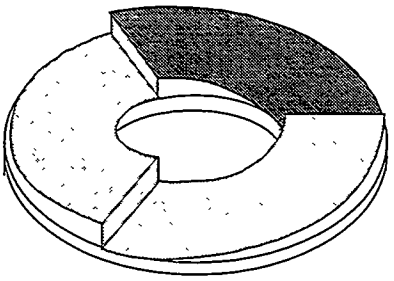

Fig.2.6. Typical sample holder. Outer diameter is 1.25inch and inner diameter is 0.5inch. Height of the ramp is 0.5mm.

One central piezotube holds the fiber tip and supplies the dithering motion for shear force feedback detection. Z approach using rotation makes the approaching scheme simpler without sacrificing stability by maintaining the whole microscope compact, but it has its own drawbacks. 1) x, y positioning is coupled with z due to rotation and makes landing on a specific spot tedious. Also, having arbitrary orientation of the scanning frame is difficult. 2) Since sample holder is sitting on scanning piezotubes rather than being attached to them, slipping of the sample can occur during fast scans with big scan

range. Also, immersion oil can couple vibrations of the optical microscope body into the sample holder causing noise problem in the shear force feedback unseen in air objective case. Both problems can be remedied if z approach is done independently using inchworms and magnets are used to holder sample holder to scanning tubes.

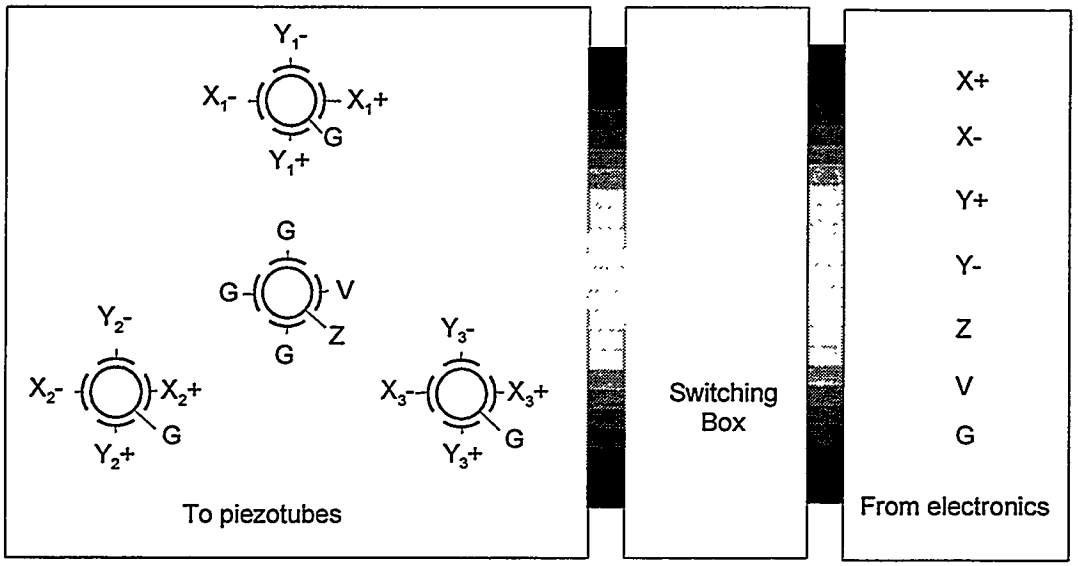

Fig.2.7 Wiring schematics for piezotube electrodes.

1" long EBL#5 tube with 0.125" diameter and 0.011 wall thickness is used (Staveley sensors Inc) for scanning. Originally, tubes are nickel plated inside and outside. Outside the nickel plating is etched to define 4 sectors of electrodes separated by about 1mm from each other. Maximum scan range achieved using +/-130 volt is ~20μm and z range is ~2μm.

Wiring scheme for scan and jerk modes

Below is the specific way of connecting the scan head to the control voltages for each mode (Fig.2.6).

In normal scanning mode, X+, X-, Y+ and Y- voltages from the STM electronics are directly connected to all X_i+, X_i-, Y_i+ and Y_i- (i = 1,2,3) electrodes of three piezotubes that support the sample holder. The inner electrodes of them are grounded (G). The

central piezotube with tip holder has three outside electrodes grounded and the remaining one outside electrode connected to the dithering voltage (V) coming from the lock-in amplifier internal oscillator. The inner electrode of the central piezotube is connected to the z control voltage (Z) from the STM electronic for distance regulation. Z feedback voltage is applied to the central piezotube instead of outside piezo scanners because of following two considerations. 1) The longitudinal resonance frequency of the piezotube is reduced when a mass is attached to the tube hence reducing the feedback bandwidth. The sample holder is heavier than the tip holder in our setup. 2) The viscosity of the immersion oil prevents the sample holder from reacting instantaneously to the piezotube motion.

In the jerk mode when the rough positioning of the sample in x, y, and z direction (up to ~mm) is necessary, a resistor network inside the switching box distribute the ramp voltages from the electronics that come through the X+ and X- nodes in appropriate ways. Operation modes can be changed as needed by turning switches on the switching box manually. When the net translation along x is necessary, X+ and X- are connected to X_i+ and X_i- and Y_i+ and Y_i- are grounded. Likewise, X+ and X- are connected to Y_i+ and Y_i- and X_i+ and X_i- are grounded for translation along y direction. To rotate the sample holder along the tangential direction for z motion, X+ and X- voltages are applied in the following way using a few voltage dividers. For the piezotube #1, Y_1+ and Y_1- are grounded and X_1+ and X_1- are connected to X+ and X- are respectively. For the piezotube #2, $Y_2+ = -\sqrt{3}/2$ X+, $Y_2- = -\sqrt{3}/2$ X-, $X_2+ = -1/2$ X+ and $X_2- = -1/2$ X-. For the piezotube #3, $Y_3+ = \sqrt{3}/2$ X+, $Y_3- = \sqrt{3}/2$ X-, $X_3+ = -1/2$ X+ and $X_3- = -1/2$ X-. Ramp height, ramp duration and the pause between ramps can be adjusted from the STM controller program to obtain optimal motions under circumstances. For x, y translations, a few millimeter scale motion is possible in a few seconds and the total translation range is only limited by the size of the sample holder. For z motion, the bottom of the sample holder is divided into three segments of 120° each with a slope changing along the

circumference (Fig.2.6). By rotating the sample holder with the inertia motion, coarse z motion up to 0.5 mm is possible. For sample holders with bigger z range, the slope is too big for the sample holder to climb back against the gravitational force. During the initial approach in the near-field measurements, it is possible to land the tip on the sample within a few microns of the target area by alternating x, y translation and z approach. It is commonplace that the sample moves in x, y direction when rotated for z approach and therefore continuous adjustment of x, y position is necessary. To reduce the time and effort it takes during the approach, this voltage controlled approach begins only after the sample is manually brought into close but safe position.

2.2.5 Typical approach algorithm.

In this section, we outline typical steps needed to bring the NSOM tip in the feedback range for our own system.

- Mount a tip.
- Soak the fiber (the other end) into acetone.
- Image the tip on the TV using low magnification (20x) air objective.
- Remove the plastic coating of the fiber, cleave the end and couple light into it.
- Optimize the light coupling and see if high enough throughput is obtained.
- Check the shape of the emission in and out of focus.
- Check the polarization extinction.
- Check the background level from the fiber tip itself.
- Sweep the shaking frequency at 5 volt rms to locate the fiber resonance.
- Adjust the direction of the shaking and the height of the tip
- Detect and optimize the feedback signal both on the oscilloscope and the lock-in amplifier by adjusting the positions of laser beam and detector.
- Reduce the shaking voltage down to a few mV.

- Set the lock-in range to the voltage setting ten times the signal level.
- Mount the sample holder.
- Focus on the sample bottom surface and rotate the sample holder manually until the sample gets close enough to the tip (100~200μm)
- Adjust the feedback signal all over.
- Press auto phase button on the lock-in and flip the phase and adjust the output offset to bring the x signal to zero.
- Make sure that all the switches are in default positions in the STM electronics
- Set the time-constant of the lock-in to 100us.
- Set the time constant of STM feedback to 8 and gain to 2.
- Flip the z offset switch to offset position and set the offset voltage at 130volt limiting the z range.
- Flip the z offset switch to range position. It should read -130volt.
- Enable the feedback by flipping the feedback switch. Z range should go to around 0 volt. The tip extend all the way up and because of the offset, it stays at about the middle of the z control range.
- Set the tunneling current set point in the STM electronics to .4nA.
- Make sure that switches in the switching box are in jerk and z approach positions.
- Start approach by clicking on the "approach now" menu.
- Stop occasionally to center the sample holder if the drift in x, y axis is appreciable.
- Feedback should automatically engage once the feedback range is reached.
- Change the z offset to zero to allow full range. Now the tip is in range at the middle of the z control range.
- Adjust the time constants and gain to stabilize the feedback signal on the lock-in amplifier.
- Withdraw the tip to avoid crashing during the following optical alignments.

- Slide the filter cube to the position with no filters.
- Turn off the illumination.
- Position the tip at the center of the field of view of the TV monitor by moving the entire NSOM head with micrometers.
- Slightly defocus the objective away from the sample.
- Rotate the nosepiece to remove the 20x objective and put a drop of oil on top of the sample (backside).
- Engage the 100x oil objective by turning the nosepiece.
- Focus on the tip.
- Set the time constant of the lock in at 30us and time constant of STM electronics at 6 and gain at4.
- Engage the tip back into feedback.
- Adjust the time constants and gain of the STM electronics to stabilize the feedback.
- Focus on the tip and move the NSOM to position the tip at the center of the field of view.
- Do the measurement.

2.3. Optical setup and Data acquisition scheme

Overall view of the experimental setup can be seen in Fig.2.9. Optical schematic for both excitation and detection is shown in Fig.2.10. Fig.2.11 shows the data acquisition scheme.

2.3.1. Excitation schemes

Light sources

We have used several different lasers depending on the specifics of the system. HeCd laser has two lines: 442nm and 350nm. Ar+ laser has multiple lines including 515nm,

497nm, 488nm, 477nm and 458nm. Kr-Ar laser has two additional lines: 568nm and 647nm. HeNe lasers with 632nm or 543nm lines are also used. For tunability, a dye laser pumped by Ar+ is also installed.

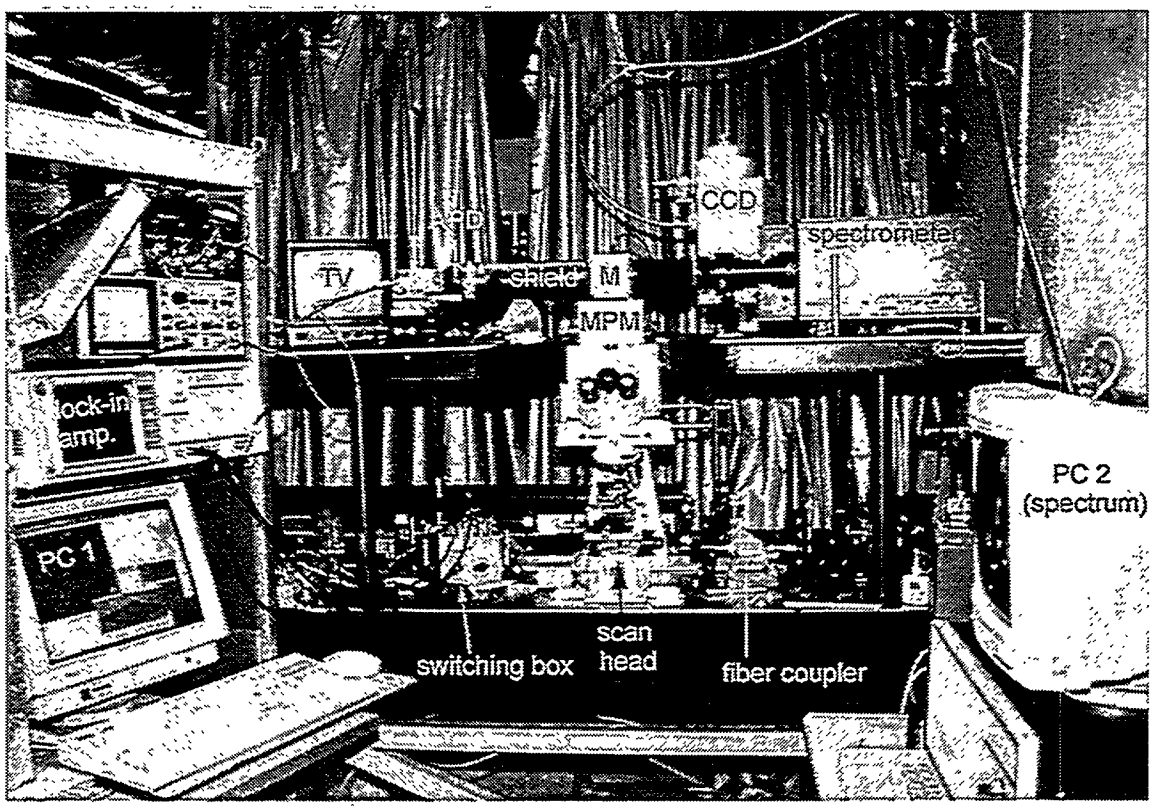

Fig.2.9 Overview of the entire setup.

Excitation schemes

Separate excitation schemes are used for near-field and far-field excitation.

Near-field excitation scheme

Laser light is vertically polarized inside the cavity. To compensate the birefringence in the fiber, one ½ waveplate followed by a ¼ waveplate are placed between the laser and the fiber. For compensation adjustment, the transmission through an analyzer after the

fiber is minimized by rotating both waveplates. Once desired linear polarization state is obtained by nulling the fiber birefringence, further control of the polarization state can be achieved by inserting a ½ waveplate, ¼ waveplate or electro-optic modulator. For near-field tips of good quality, polarization extinction as good as 1,000 to 1 can be obtained and maintained if the fiber is untouched during the experiment.

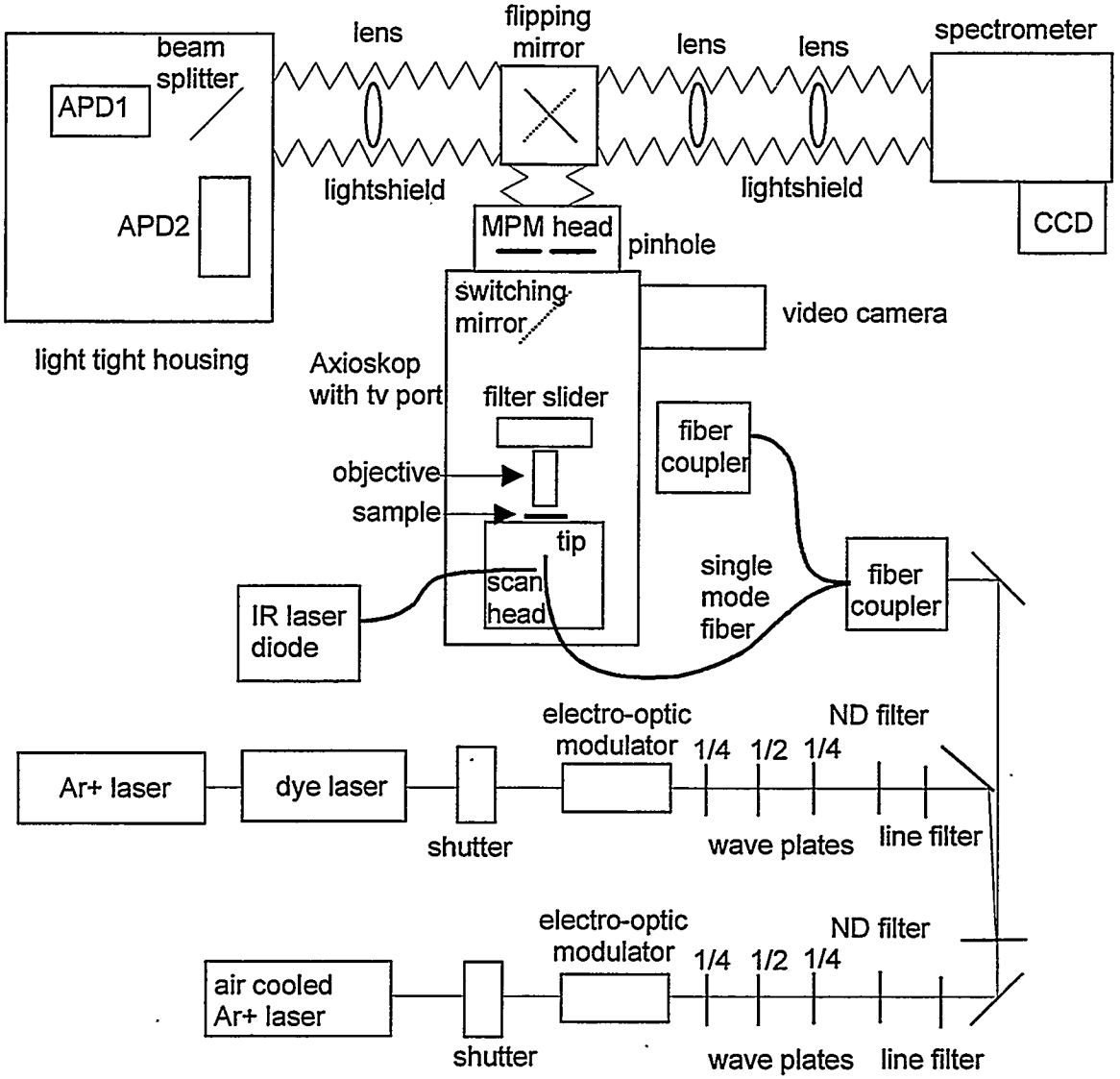

Fig.2.10 Optical setup for near-field and far-field imaging and spectroscopy.

To suppress the spontaneous emission component from the laser, a laser line filter is placed before the fiber. A variable neutral density filter (up to O.D. 2) and a combination of fixed neutral density filters are used to adjust the excitation level. Electronic shutter

(Vincent Assoc., UniBlitz) may be placed in the beam path to control the exposure automatically. Excitation intensity can be as high as 1kW/cm^2 or 2.0 x 10^{11} photons/sec. When two color excitation is needed, two laser beams each with waveplates, filter and shutter in the beam path are combined by a beam splitter. Care must be taken when coupling the two laser beams together, since a beam splitter or dichroic mirror has a polarization dependent response. To prevent this, the two beams are aligned collinearly with a 50% neutral density filter which is tilted under a very small angle (<1°).

Far-field excitation schemes

A single mode fiber is used to bring the laser light to the same level as the epi-fluorescence port. The single mode fiber acts also as a spatial filter, and a few micron core of the fiber can be considered as a point source for confocal microscope. We modified the epi-illumination path of the microscope such that the laser can come in from the side rather than from behind. This avoids hitting many optical elements in the conventional epi-illumination path and enables us to get high quality beam. Before the laser light is coupled into the fiber, waveplates are used to compensate the fiber birefringence. Electronic shutter and neutral density filters are also used. After the fiber, a 20x objective collimates the beam and send it into the microscope. In the beam path, an electro-optic modulator (Conoptics, M350-50 and Model 302) and a waveplate may be used for polarization/intensity modulation. Laser polarization needs to be linear at 45° to both transverse crystal axis of the electro-optic crystal, the change of polarization state is governed by the voltage on the crystal which in turn can be controlled with an analog output voltage (-1 volt ~ 1 volt) from a computer. Output from the electro-optic modulator is elliptically polarized in general, and adding a polarizer afterward results in the intensity proportional to $\cos^2(a*V_m)$ where V_m is the voltage applied to the modulator

and a is a proportionality constant. To obtain a linear polarization with the angle linearly dependent on V_m, a ¼ waveplate with the crystal axis at 45° relative to the crystal axis of the modulator. Polarization of the excitation after the reflection from the dichroic mirror in the epi-illumination path remained linear for all incident linear polarization because the reflectivity of the dichroic mirror at the laser wavelength is high (>98%) for both s and p component of the electric field. A laser line filter and a dichroic mirror are used in the cube block to direct only the laser line toward the main objective. 1.4 NA objective then focuses the light into a diffraction limited spot on the sample plane. The beam on purpose underfilled the objective aperture in order not to scatter off the metallic objective case. Hence, the numerical aperture is not at its optimum in excitation, and 400nm spot size is normally obtained. Excitation intensity is virtually unlimited in the far-field case.

2.3.2. Detection path

Once the sample is excited, the same collection and detection scheme can be used regardless of the excitation scheme.

Light collection

Samples are usually mounted on glass coverslips. Photons are collected with 100x 1.4 NA oil immersion, infinity corrected objective (Zeiss, PlanApochromat). Since the light is collimated after the objective, any number of filters may be inserted without much affecting the imaging quality of the system. The light path in the body of the microscope (Zeiss, Axioskop) consists of the following: (1) dichroic mirror and/or color glass filter for excitation rejection, (2) tube lens; (3) pinhole (640μm or 100μm diameter). Choice of right pinhole size is important because too small a pinhole reject even the major portion of the signal of interest while too big a pinhole will degrade the background rejection effect. After the pinhole, the light is directed to silicon avalanche photodiodes (APD),

where imaging and emission time traces are measured, or to the spectrometer and a cooled CCD camera, for emission spectroscopy.

Detectors

APDs (EG&G Canada, SPCM-200-PQ) have high quantum yields (>50%) over entire visible range, have small number of dark counts (< 10 per second) and have built-in preamplifier and discriminator so that they can send out a TTL pulse for every photon detected. TTL pulses are split into a rate meter for real time signal monitoring and into a PC counting board for data acquisition. Because of detector dead time, the count rate saturates at high count rate. For example, 1.7 needs to be multiplied to the apparent count rate of 1MHz to get the actual count rate. For count rate smaller than 200 counts/millisecond, the correction factor is negligible. One-to-one imaging of the pinhole to the APDs is done using an achromat lens. A diffraction limited spot on the sample plane is roughly contained in the 150mm diameter detector active area, so the efficient detection with good background rejection is possible. A dichroic mirror (Omega optical, DRLP) or a polarizing beam-splitter cube (CVI laser, PBSH-450-700-050) in front of the APDs are used for simultaneous two channel detection. Interference filters are often placed in front of the detectors to reduce crosstalk between the two channels.

For emission spectroscopy, the pinhole is imaged onto the entrance slit of the spectrometer (Spex Industries, 270M) using two achromat lenses and the input angle into the spectrometer is controlled to match the F-number so as to minimize the loss inside the spectrometer. The spectrometer's focal length is 27cm and toroidal mirrors are used to achieve good imaging quality in case extended sources are studied. The best efficiency was obtained with 300 grooves/mm grating. Vertical thirty pixels and horizontal five pixels are grouped together resulting in fast readout time and shorter integration time while maintaining the necessary spectral resolution of 1.5nm. Short integration time is possible because readout noise of 5 counts is independent of binning while the signal

increases in proportion with the binning. For 5 second integration time, 100-300 peak counts are typically observed for single molecules in the near-field case. The loss inside the spectrometer is roughly 50%. The CCD chip(Princeton instrument, PI 330x1100, back-illuminated) is cooled by liquid Nitrogen, and the data acquisition is controlled through the CCD electronics (Princeton Instruments, ST-130).

Collection efficiency

The collection efficiency of the total detection scheme was measured in the following way. Light of known intensity (power is measured with a calibrated power meter, Newport, 1830-C and 818ST) is incident through the epi-illumination path. A mirror is used instead of the sample to reflect the light toward the detector. The number of counts from the detector is converted into power and compared to the incident power. We assume that about half of the photons emitted in the bottom hemisphere are lost in the case of single molecule emission unlike in the case of mirror, and finally estimate the total collection efficiency to be about 10%. That is, out of 100 photons emitted by the molecule, 10 counts can be registered at the computer. For the CCD camera after the spectrometer, each count corresponds to about 100 photons emitted because 5 electrons are registered to be one count due to the gain setting of the CCD electronics and 50% of photons are lost inside the spectrometer.

2.3.3. Data Acquisition

The experiment is controlled by two PC computers (Fig.2.11). Data and control signals are digitized/generated with four plug-in boards (Princeton Instruments parallel buffer board, National Instruments AT-TIO-10 counting board, National Instruments AT-AO-6 analog output board and Data Translation DT2821 analog and digital I/O board)

Commercial programs are used for imaging (RHK Technology, SPM32) and for emission spectroscopy (Princeton Instruments, CSMA).

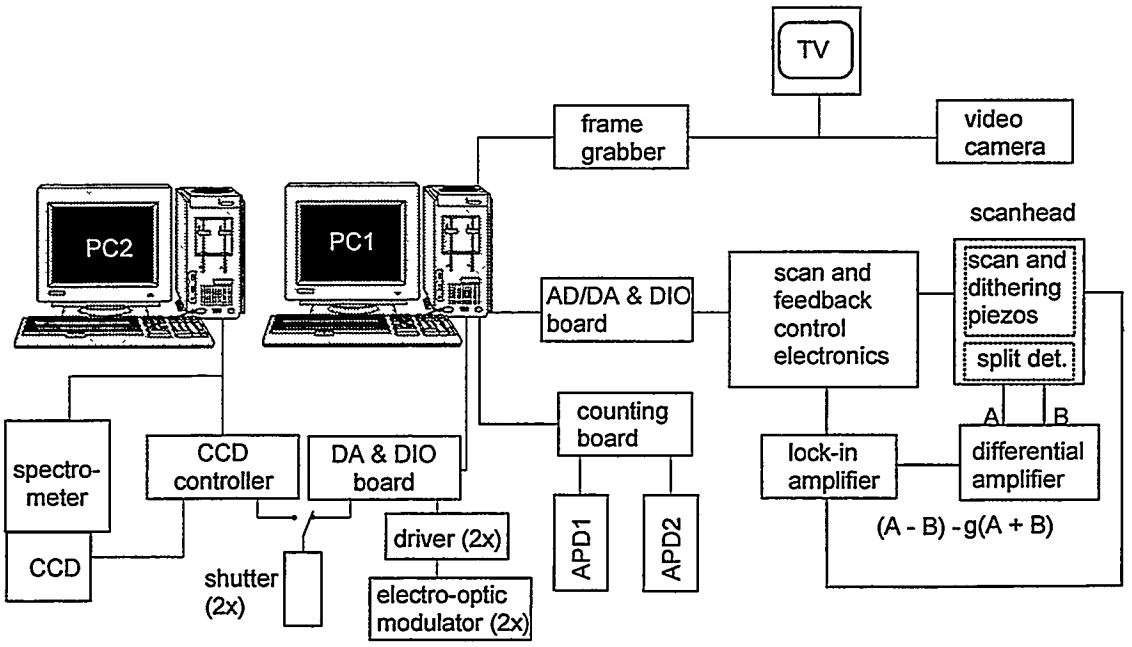

Fig.2.11 Electronic control and data acquisition schematics.

A third program (home-written in C++) is used for automatic search, positioning and modulation spectroscopies (Ha et al. 1996a). It provides the voltage modulation for sample movement, controls the shutter and the electro-optic modulator for polarization and intensity modulation and reads the photon counts for each integration time from the APDs via the counting board. Further description of the program will be given in the context of automated positioning in Appendix A. Commercial STM electronics (RHK Technology, STM1000) is used for both feedback and scanning.

3. HIGH RESOLUTION NEAR-FIELD IMAGING

3.1. Resolution of NSOM

Far-field optical microscopy has lateral resolution limited by diffraction of light. There is a minimum distance d that the diffraction images of two points in the specimen approach each other before they merge and can no longer be resolved as two separate points. This lateral resolution is given by $d = 1.22 \lambda / (NA_{obj} + NA_{cond})$, where λ is the wavelength of the light in vacuum, and NA_{obj} and NA_{cond} are the numerical apertures(NA)s of the objective and the condenser lenses respectively. NA is the given by $NA = \sin(\theta/2) \cdot n$, where θ is the angle of the cone of light acceptable by the lens to form an image, and n is the index of refraction of the medium between the lens and the specimen. Best resolution can be obtained in the epi-illumination geometry where both the illumination and the collection is done through the same high NA objective. With NA = 1.4 available from an oil immersion objective, the ultimate resolution is 220nm when green light (500nm) is used. In principle, better resolution could be obtained for shorter wavelength light, but the quality of the objective deteriorates and other problems like chromatic and spherical aberrations become significant.

Axial resolution is half of the lateral resolution because the response of a point source around the image plane has a shape of an American football elongated along the axial direction(Born and Wolf 1980).

Aperture based NSOM has both lateral and axial resolution on the order of the aperture size. High axial resolution stems from the fact that the energy density drops exponentially away from the aperture rather than quadratically as in the case of far-field focusing. On one hand, it puts a strong requirements on the sample to study with NSOM: the sample has to be thin. Otherwise, part of the sample will be away from the near-field

of the tip, and the result will be difficult to interpret because it will be a superposition of near-field and far-field effects. On the other hand, NSOM can be used as a surface specific tool of a thick sample because of the strong divergence of the energy density. As discussed in the previous chapter, the theoretical resolution limit for the aperture based NSOM is 50nm because of the finite conductivity of the aluminum. However, resolutions down to 12nm have been claimed experimentally for 20nm diameter aperture (Betzig et al. 1991).

In this chapter, we show the NSOM imaging with three different contrast mechanisms: transmission, topography, and fluorescence. Transmission imaging was done on a test pattern for the initial test of NSOM. Shear force imaging accompanies every NSOM imaging because it is a part of the feedback scheme, and its contrast mechanism and response function are discussed. Dual color fluorescence imaging of malaria infected red blood cell demonstrates a case where NSOM has unique advantages that cannot be paralleled by any other imaging techniques and can produce meaningful biological results.

3.2. Transmission imaging of test pattern

For the initial test of NSOM, we imaged a test pattern of small features down to 100nm in size. We used electron beam lithography to make a test pattern containing many geometric shapes and LBL logo. A thin layer (~100nm) of PMMA (molecular weight 495, 4% solution in chlorobenzene) is spin-coated for 45 seconds at 4,500rpm. The coverslips was annealed for 1 hour at 180°C. The pattern was written with an SEM (JEOL) at 208 $\mu C/cm^2$ exposure level. After the exposure, the coverslip was developed for 30 seconds at 21 degree. 20nm of gold is evaporated on the coverslip and the PMMA coating is lift-off by stirring the coverslip in warm acetone.

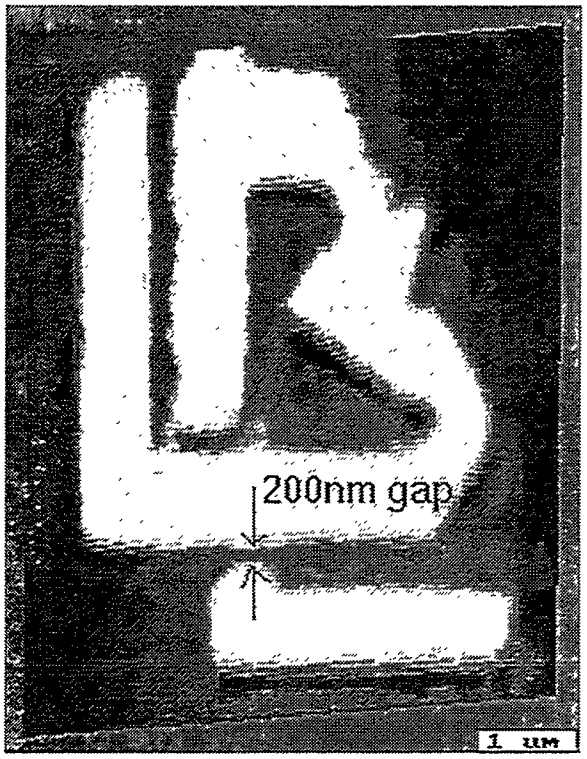

Fig.3.1 Optical image of an lithographic pattern of LBL logo taken with NSOM in transmission mode.

The 442nm line of HeCd laser light is coupled into the fiber and the transmitted light through the sample is collected with an objective and imaged onto a PMT. Optical transmission image and topographic image with shear force feedback are taken simultaneously. One example of the optical image is shown in Fig.3.1. The smallest feature in the test pattern is the 200nm gap marked in the image, and is clearly resolved. Based on the edge sharpness (10% to 90%), the resolution is estimated to be 80nm, or $\lambda/5$.

3.3. Shear force images : effect of the tip morphology

Shear force imaging does not reveal the true topography of the surface and is rather a convolution of the topography and the probe morphology at constant shear force. In addition, dithering of the tip for the shear force detection broadens the response function and limit the resolution of the shear force imaging. In general, performance of a tip in shear force imaging and optical imaging is mutually exclusive. A tip with good resolution in shear force imaging tends to have a sharp protrusion in the metallic coating which results in poor optical imaging both because of distorted electric field distribution around the protrusion and because it prevents the aperture from being close enough to the surface. Likewise, a tip with good morphology for optical imaging does not yield high

resolution shear force imaging because the shear force signal is averaged over entire diameter of the tip which is about 300nm (aperture size + coating).

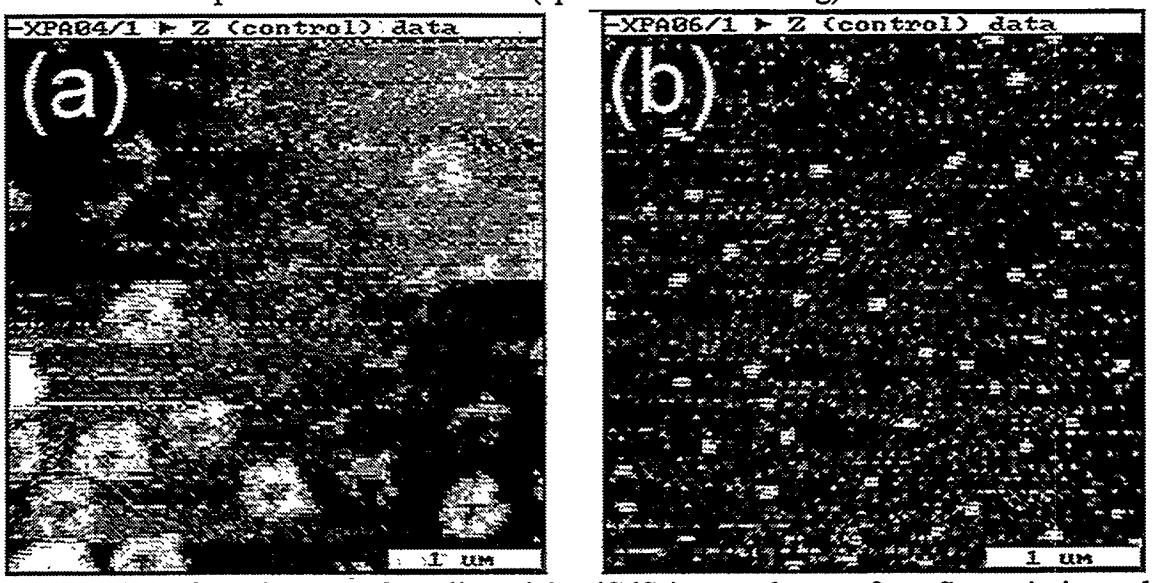

Fig.3.2. Shear force images of small particles (CdSe) on a glass surface. Same tip is used for both images but at different times. The change in morphology of the tip resulted in the different point response function of particles.

In the same manner that a single molecule can be used to map the electric field distribution of the near-field probe because it is a single point dipole source (see next chapter), a small particle may be used as a tool to map the morphology of the tip. Trautman et al. (Trautman and Macklin 1996) used 10-150nm silicon crystallites to image the tip in constant shear force mode in an attempt to correlate the tip diagnostics with the position dependent single molecule lifetime as the tip is scanned across the molecule. We have used CdSe nanocrystals of 2~3nm in size to map the bottom of the tip in the same manner and the result is presented in Fig.3.2. Initially, shear force imaging of single nanocrystals (Fig.3.2a) shows many identical flower-shaped responses with a central hole. In this case, the bottom of the tip is relatively flat and the small particle can map the morphology of the tip, even the aperture. Two scans later, the shear force image (Fig.3.2b) shows many tiny spots. In this case, the tip has either picked up a piece of dirt or been damaged such that a sharp protrusion exists at the end of the tip, and the response function is sharply defined.

3.4. Dual color fluorescence imaging of malaria infected red blood cell membrane

3.4.1. Introduction

One of the crucial aspects of current biological inquiry relates to the organization of cells and how interactions between proteins are involved in important cellular processes, such as gene expression, protein function and signal transduction mechanisms. Several experimental systems have been developed in recent years trying identify such protein-protein interactions. All such attempts to identify interactions in disassembled cellular systems (by bio-chemical techniques) need to be confirmed in a fixed and assembled state, by approaches such as chemical cross-linking in cells or some form of co-localization study using microscopy. A common approach has been confocal microscopy using fluorescent antibody probes. The use of NSOM offers significant advantages, compared to confocal microscopy, in the co-localization of proteins, particularly at the membrane of cells: (i) NSOM imaging exhibits super-resolution; (ii) The near-field source excites fluorescence only from the outermost layer (50 -100 nm) of the cell - i.e. - the cell membrane - due to the quick drop in its evanescent field; (iii) As a result, very good signal to background ratio is obtained, because auto-fluorescence is not integrated across the whole cell thickness; (iv) Topography information from the shear-force feedback allows real space mapping of proteins with sub-wavelength resolution (100nm) in the cell membrane; (v) Dual-color excitation via shared aperture eliminates chromatic aberration, and hence permits super-resolution co-localization studies; (vi) Mapping and co-localization studies can be performed with only few copies of proteins due to the exquisite sensitivity of the instrument.

As a demonstration of the power of NSOM to the co-localization investigations of proteins in cells, we elected to study human red blood cells invaded by the human malaria parasite. During the parasite growth, it expresses proteins that are transported to the red blood cell membrane. Association of parasite proteins with host skeletal proteins leads to modification of the membrane. Knob-associated *P. falciparum* histidine rich protein (PfHRP1) is the predominant parasite protein component of knobs, protrusions of ~100 nm diameter on the infected red blood cell membrane. The mature-parasite-infected red blood cell surface antigen (MESA) associates with host protein 4.1 (Lustigman et al. 1990; Magowan et al. 1995). We performed co-localization studies of parasite proteins with host proteins. Host and parasite proteins were selectively labeled in indirect immuno-fluorescence antibody assays. Simultaneous dual-color excitation and detection with NSOM provided fluorescence maps together with topography of the cell membrane with sub-wavelength (100nm) resolution.

3.4.2. Experimental scheme

For co-localization studies, proteins of interest were labeled with antibodies conjugated to two different fluorophores: FITC and TR. Sample preparation is described in detail in (Enderle et al. 1996)* . FITC was excited by a 488nm line of an air cooled Ar^+ laser (532-AP, Omnichrome) and TR was excited by a 568nm line of a Krypton-Ar^+ laser (Innova 70 Spectrum, Coherent). The two excitation beams were collinearly combined and simultaneously coupled to the NSOM fiber probe. Two detectors were used to simultaneously acquire the two emissions (Ha et al. 1996e). Since the two excitation wavelengths shared the same near-field aperture, the fluorescence images were in perfect registry, pixel by pixel. This is in contrast to confocal and wide-field fluorescence

* Sample was prepared in the laboratory of Cathy Magowan.

microscopy where chromatic aberrations cause misalignment of the two-color images acquired on the two detectors. The excitation was blocked with a color glass long pass filter (515 nm, LP515, Oriel) and a Raman notch filter (568nm, HSPF-568-1.0, Kaiser Optical Systems). The collected light was split into two channels by a dichroic mirror (558nm, 558DRLP, Omega Optical). To eliminate cross-talk between channels, band pass filters 535 nm center, 25 nm full width half maximum (FWHM) (535DF25, Omega Optical) and 635 nm center, 25 nm FWHM (635DF25, Omega Optical) were placed in front of the short wavelength (FITC) and long wavelength (TR) detectors, respectively. With the band pass filters in place, the cross-talk was measured by exciting the dual-color labeled red blood cell with either of the two single laser lines. With 568nm excitation alone, the signal in the long wavelength channel was 90% of the signal obtained with dual-color excitation, and the signal in the short wavelength channel was at the dark count level of the detector, indicating no cross-talk from TR to FITC. With 488nm excitation alone, the signal in the long wavelength channel was 10% of the signal obtained with dual-color excitation. In the short wavelength channel, on the other hand, we measured the same signal level as with dual-color excitation. The 10% cross-talk on the long wavelength channel is due to the absorption tail of TR at 488nm and the emission tail of FITC.

The distribution of proteins in the red blood cell membrane is presented as color-coded image overlaid on topography, which is displayed as height in a three dimensional plot. A quantitative analysis of the co-localization was carried-out through pixel-by-pixel correlation of red and green images: the intensity in each channel was analyzed for every pixel and displayed as a single point in a two-dimensional histogram. The x,y coordinates of each point presented the intensities in red and green channels, respectively. The number of occurrences of each x,y pair is presented by a gray scale value (brighter color corresponds to more occurrences). In such two dimensional histograms, two perfectly correlated images show up as a straight line along the diagonal; anti-correlated images

result in two lines along the two axes and un-correlated images exhibit a broad, unstructured distribution. We note that such analysis can be performed only when the two images are in perfect registry.

3.4.3. Results and Discussion

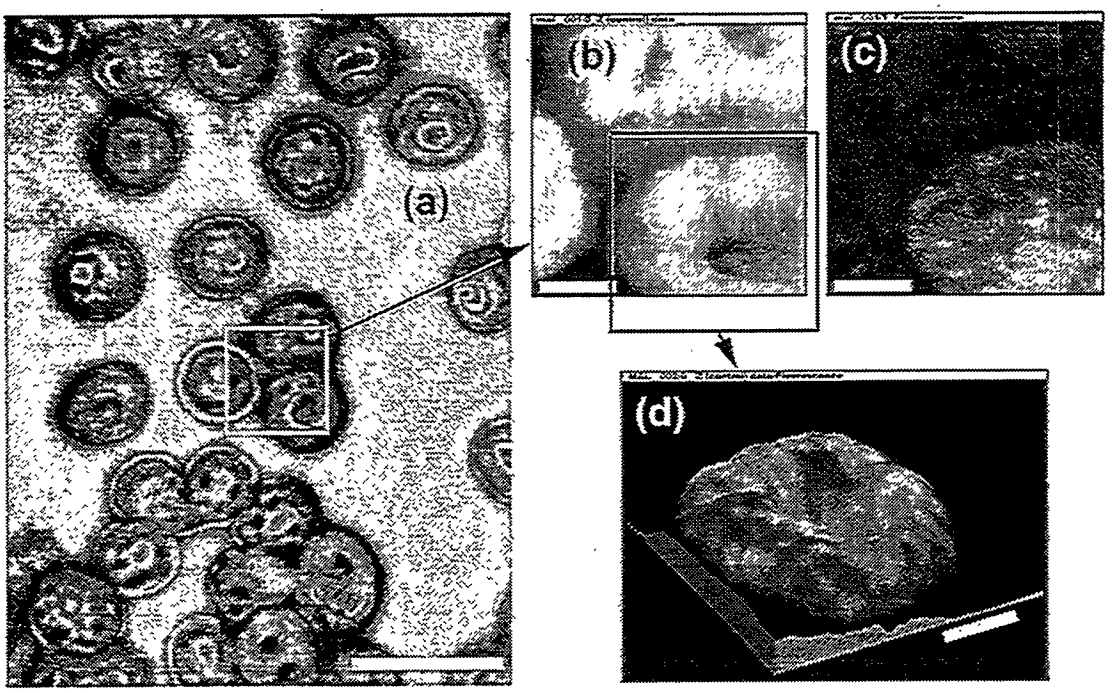

Fig.3.3 Mapping of parasite protein in the erythrocyte membrane. A blood smear of the trophozoite stage was fixed and stained with antibodies against PfHRP1. (a) bright field image of the blood smear. The NSOM tip was positioned above the three cells in the center of the field of view and a scan was taken within the framed area (b) Result of the NSOM imaging in topography (left) and fluorescence (right). . While all three cells are imaged in topography, only the one in the lower right corner was infected and shows up in the fluorescence image. (c) Zoom around the infected cell which was seen in the lower right corner of (b). The fluorescence signal is superimposed as a color value to the topography to show the distribution of PfHRP1 in the erytrhocyte membrane. Scale bar for (b) and (c) is 2 μm. Z range for (c) is 1 μm.

Fig.3.3a shows a bright-field image of red blood cells labeled with antibody against PfHRP1 and immuno-labeled with TMR conjugated secondary antibody. The NSOM tip was positioned at the center of the field-of-view and a zoomed-in scan was performed

(area shown by yellow rectangle). Fig.3.3b and c shows the simultaneously acquired topography signal (left) and fluorescence signal (right). As can be seen, the three cells which are enclosed by the rectangle in Fig.3.3a are visible in the topography image, but only the infected red blood cell, in the lower right corner of the rectangle, is detected in the fluorescence image. In addition, the topography image of the infected cell shows "grainy" features and the membrane surface is deformed compared to neighboring, uninfected cells. Examination of a large number of cells confirmed the finding that infected cells were consistently more deformed in topography maps. The signal strength of the fluorescence was about 300 counts/ms. The background, dominated by the fiber tip auto-fluorescence, was about 10 counts/ms. Auto-fluorescence of red blood cells was negligible compared to the fiber background, most probably due to the membrane-specificity of the technique. A further zoom-in around the infected cell in Fig.3.3b (box) is shown in Fig.3.3d. Here the fluorescence signal is superimposed as a color value (brightness scale goes from black white) on the topography to show the distribution of PfHRP1 in the red blood cell membrane. Fluorescence spots with typical sizes of 100 - 150 nm are clearly resolved. Their average density is found to be 10 spots/mm^2, which corresponds to the surface density of knobs deduced from electron microscopy images of isolated infected red blood cells membranes (Gruenberg et al. 1983). We conclude that the fluorescence spots in Fig.3.3 originate from PfHRP1 in individual electron-dense knobs on the infected red blood cell membrane. We cannot, however, resolve the fluorescence distribution within individual knobs, since the average knob size is 105 nm (Gruenberg et al. 1983), comparable to the resolution of the technique.

Fig.3.4 compares NSOM imaging (Fig.3.4.a) with confocal imaging (Fig.3.4.b) of infected red blood cells. These images were separately taken on infected red blood cells from the same culture which were fixed and dried in parallel and labeled against PfHRP1.

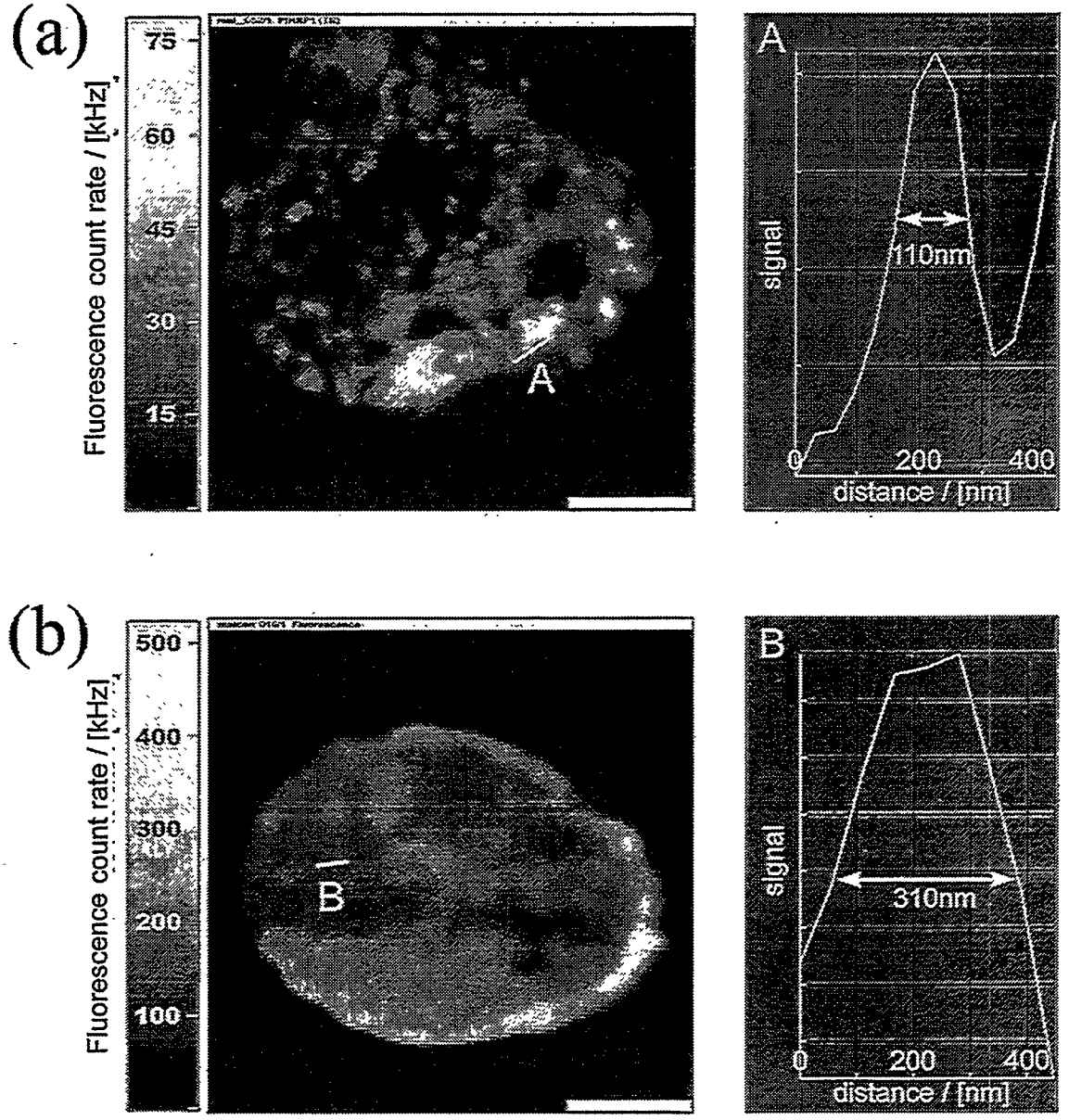

Fig.3.4 NSOM (a) and confocal (b) imaging of infected erythrocytes (not the same cell) which were stained with antibodies against PfHRP1. The figures show the fluorescence image (left) and a cross section (right) through the smallest feature found in the image (marked with a line in the image). (a) In the NSOM imaging, the PfHRP1 knobs can clearly be visualized with a size distribution of 100-300nm. The resolution of the image is at least 100nm, given by the FWHM of the curve along the cross section. (b) The confocal image gives a section through the cell, the membrane can be only seen as a bright ring. The resolution (see curve in the right part) is about 250nm.

The NSOM image (Fig.3.4.a) shows an infected red blood cell reacted with anti-PfHRP1. A cross-section taken along the line "A" is shown on the right. It shows the

smallest feature in the image, with a FWHM of about 100 nm. A confocal image of a similar anti-PfHRP1-labeled infected red blood cell is shown in Fig.3.4.b. Here again the smallest feature in the image is shown in a cross-section "B" (right), with a FWHM of 310 nm. In contrast to the *selective imaging of the membrane proteins* by NSOM, the confocal image shows a cross-section *through* the cell. A bright ring of fluorescence in the confocal image indicates that most of PfHRP1 resides in the membrane. However the confocal image is a cross-section of the cell and can not reveal the distribution of PfHRP1 on the membrane surface, or the membrane topography. Furthermore the resolution of the confocal image is 3 times lower compared to the NSOM image.

Dual-color labeling and dual-color detection, together with pixel-by-pixel analysis described above, were utilized to study co-localization of two host-parasite protein pairs. A thin blood smear of red blood cells infected with trophozoite stage parasites was fixed and then reacted with either mouse monoclonal or rabbit polyclonal antibodies against the proteins under study. Secondary antibodies (anti-mouse or anti-rabbit) labeled with either FITC or TR were then used to stain the proteins.

The results for the control experiment are shown in Fig.3.5a, and for the two host-parasite protein pairs are shown in Fig.3.5b and Fig.3.5c. The left columns of the figure shows the two simultaneously acquired and pseudo-colored images for each case. The left column and the middle column images represent raw data acquired on long wavelength (TR) and short wavelength (FITC) channels, respectively. The right column shows pixel-by-pixel correlation of the red and green channels.

Fig.3.5a shows the results of the control experiment. Immuno-fluorescence staining against PfHRP1 was performed with mAb 89. This monoclonal antibody maps to a repeated epitope on the HRP1 protein. Secondary antibodies (goat anti-mouse) were labeled with FITC and TR. The overlay image (center column) shows only yellow areas, indicating the expected perfect overlap between red and green channels since the same protein moiety has been labeled with two different fluorophores. This overlap is

confirmed by the pixel-by-pixel correlation which shows a straight line along the diagonal (right column). This result confirms the validity of the technique, since no off-diagonal red-green-pairs could be found.

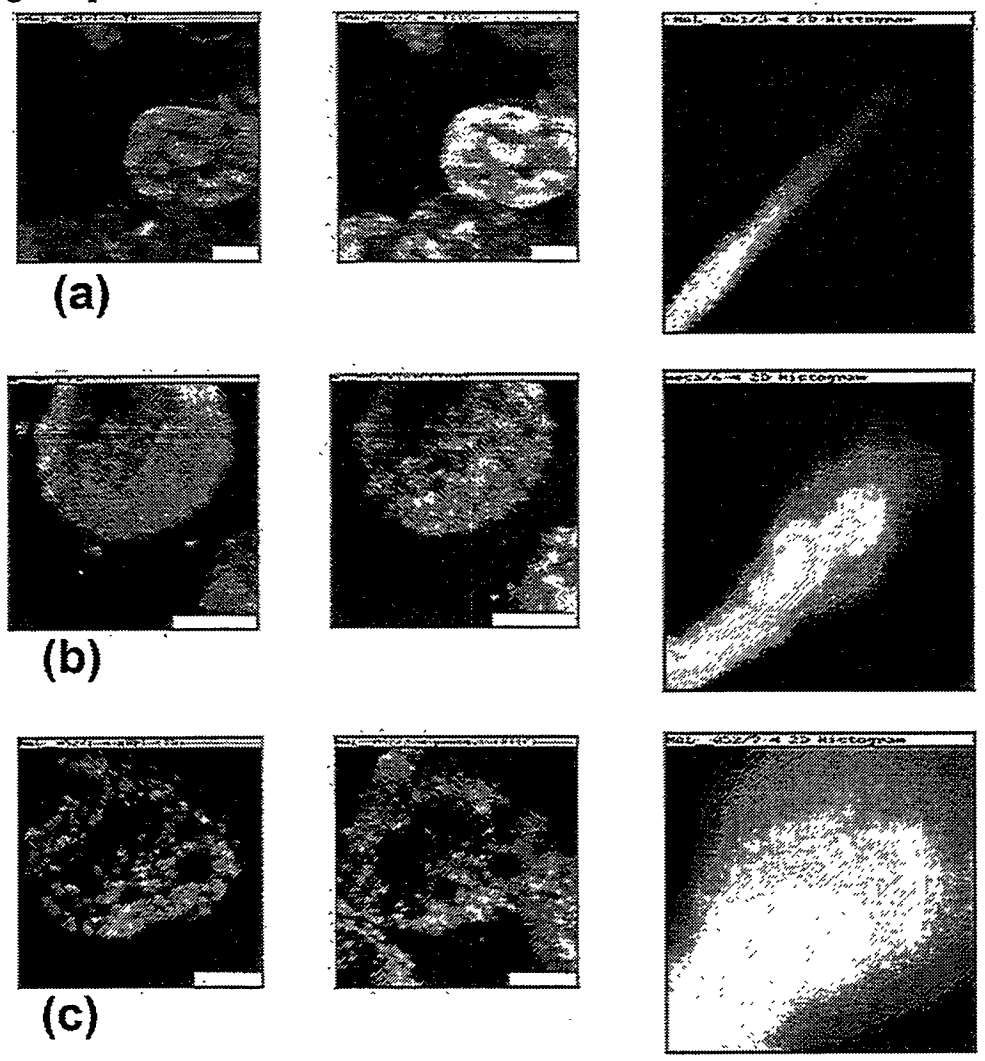

Fig.3.5. Co-localization of malarial and host proteins in the rbc membrane. The secondary antibodies were labeled with FITC (anti-rabbit) and Texas Red (anti-rabbit), respectively. The left two columns show the two simultaneously acquired fluorescence channels by NSOM dual-color imaging, the left column is Texas Red channel, and the middle column is FITC channel. The right column is the analysis of the correlation between the red and green channel according to the 2 d intensity hisogram.. (a) Control experiment. Both primary antibodies were used against PfHRP1. The overlay image show uniform yellow areas and the pixel by pixel correlation is a straight line. (b) Co-localization of MESA and band4.1. (c) Co-localization of PfHRP1 and band4.1. Scale bar for (a)-(c) 2 μm.

Fig.3.5b shows co-localization results for the host-parasite pair protein 4.1/MESA. Protein 4.1 was labeled with FITC conjugated, and MESA with TR conjugated, secondary antibodies. The overlay image (center column) predominantly shows yellow areas of overlap between the two fluorophores. There are very few regions where green-only or red-only fluorescence can be found. The correlation analysis (right column) shows linear distribution, indicating co-localization of MESA with protein 4.1. This result indicates that MESA and red blood cell protein 4.1 interact *in-situ* in the membranes of infected red blood cells.

Fig.3.5c shows co-localization results for the host-parasite pair protein 4.1/ PfHRP1. Secondary antibodies conjugated with FITC or TR were used to localize protein 4.1 and PfHRP1 respectively in the infected red blood cell membrane. The overlay image (center column) clearly shows that PfHRP1 and protein 4.1 are only poorly co-localized, as confirmed by pixel-by-pixel correlation which exhibits a very broad distribution around the diagonal (right column). Thus we conclude that there is no association between protein 4.1 and PfHRP1 in the membrane of infected red blood cells. While both, protein 4.1 and PfHRP1, are present in knob structures, these two proteins do not directly interact with each other as MESA and protein 4.1 do.

3.4.4. Summary

NSOM was used to perform membrane oriented co-localization measurements, together with topography mapping, of parasite and host proteins in malaria infected red blood cells. Our results imply that the malarial protein MESA interacts with red blood cell protein 4.1 in membranes of infected red blood cells while PfHRP1 does not interact with protein 4.1.

Extrapolating from previous biochemical analyses that indicate the presence of protein 4.1 in knobs (Chishti et al. 1992; Leech et al. 1984) and the evidence that PfHRP1 and protein 4.1 both bind to spectrin and actin in the red blood cell skeleton (Discher et al. 1995; Kilejian et al. 1991), it has been tacitly assumed that PfHRP1 and protein 4.1 may interact in infected red blood cell membranes. Our results unequivocally show that this is not the case. This data extends our previous finding that protein 4.1 is not required for PfHRP1 to localize to the infected red blood cell membrane, while protein 4.1 is necessary for localizing MESA at the membrane surface (Magowan et al. 1995).

4. SINGLE MOLECULE DETECTION

4.1. Introduction

Most spectroscopic experiments in condensed matter or liquid phase measure the average behavior of a huge number, N, of molecules, where N may range from 10^6 to 10^{23}. At the same time, most theoretical models are intended to describe the behavior of a single molecule interacting with its surroundings, and averaging over the number of molecules N is normally required to compute an observable. When a single molecule is examined at a time, strong tests of truly microscopic theory may be completed.

In this chapter, we report room temperature SMD on immobilized molecules using near-field and far-field scanning optical microscopy. This area of research was initiated by the pioneering work of Betzig, Ambrose, Xie and Trautman (Ambrose et al. 1994a; Ambrose et al. 1994b; Betzig and Chichester 1993; Trautman and Macklin 1996; Trautman et al. 1994; Xie and Dunn 1994), and holds promises for practical applications as well as fundamental understanding of single molecule level processes.

4.2. Feasibility - signal level estimation

Typical signal level can be estimated for a single fluorescent molecule of interest. The total number of photons detected (N_d) from a single molecule for a given integration time τ and the excitation power P_0 is given by

$$N_d = \eta \phi \sigma P_0 \tau / A h\nu \qquad (4.1)$$

where η is the total detection efficiency of the fluorescent photons, ϕ is the quantum yield of emission, σ is the absorption cross section at the excitation energy, A is the

effective area of the excitation, h is the Planck constant and ν is the frequency of the excitation laser.

Extinction coefficient of Texas Red molecule is 85,000 liter/mole-cm which is typical of efficient dye molecules. This corresponds to the absorption cross-section σ of 1.4 $Å^2$ and the absorption yield, approximated by the ratio between the molecular absorption cross-section and the excitation spot size, or σ / A is $5 * 10^{-6}$ for the near-field case and $3 * 10^{-7}$ for the far-field case. For the typical excitation intensity shown in Table.4.1., roughly one million photons per second are absorbed by the molecule. With 0.5 quantum yield ϕ for emission and 10% detection efficiency η, up to 50 counts/ms of count rate is expected from a single molecule. At a low count level, an important source of noise is shot noise. Shot noise results from the statistical variation in the number of detected photons, which obeys a Poisson distribution. The Poisson distribution has the property that its mean is equal to its variance and the noise given by the square root of the variance, is $N_d^{1/2}$. For 5ms integration time, the resulting count N_d will be 250. If the background noise is negligible, the signal to noise ratio, S/N, is $N_d/N_d^{1/2}$ or $N_d^{1/2}$~16. So it is quite possible to detect single molecules with the excitation level attainable by near-field probe, and S/N better than 10 is expected with 5ms second integration time when only shot noise is included.

Table4.1. Comparison of single molecule excitation in the near and far-field.

	Power (@515nm)	*Intensity (@515nm)*	*Photon flux*	*Absorption yields*	*Excitation rate*
Near-field (100nm spot)	90nW	1.1kW/cm^2	$2 * 10^{11}$ /sec	$5 * 10^{-6}$	$1.0 * 10^6$ /sec
Far-field (400nm spot)	1μW	0.8kW/cm^2	$2.5 * 10^{12}$ /sec	$3 * 10^{-7}$	$7.5 * 10^5$ /sec

When additional sources of background noise, intensity dependent or non-dependent, are included, the signal to noise ratio takes the following form,

$$S/N = \frac{\eta \cdot \phi \cdot \sigma \cdot P_0 \cdot \tau / A \cdot h \cdot \nu}{\sqrt{\eta \cdot \phi \cdot \sigma \cdot P_0 \cdot \tau / A \cdot h \cdot \nu + C \cdot P_0 \cdot \tau + N_{dark} \cdot \tau}} \tag{4.2}$$

where C is the laser induced background count per unit excitation power, and N_{dark} is the dark count rate. From the above equation, there are several important criteria that have to be fulfilled for good S/N detection of single fluorescent molecules. 1) Total detection efficiency has to be optimized. Use of the high numerical aperture objective and detectors with good quantum efficiency makes it possible to obtain η higher than 10%. In low temperature SMS, both collection and detection suffer because a proper imaging of the sample area onto a small area detector is very difficult. 2) Fluorescence quantum yield needs to be high which is true for most molecules under study both at room temperature and low temperature. 3) Absorption cross section for good dye molecules is on the oder of a few angstrom^2. At low temperature SMS, the absorption line width of those specially selected systems is very narrow (<10MHz), effectively limited by lifetime broadening, resulting in the concentration of the oscillator strength and σ of up to (300Å)^2. 4) Increase of power also improve S/N, but the absorption cross section drops for high excitation intensity because of the saturation due to triplet state. Molecules with high transition rate to the triplet state and long triplet lifetime need be avoided. 5) The area of the excitation spot A at the sample plane should be as small as possible. For far-field excitation, the smallest A is limited by diffraction. For near-field excitation, a compromise between the spot size and the total throughput has to be made because of the a^6 dependence of the throughput, where a is the diameter of the aperture. 6) Background arising from substrate, fiber, and optical elements need be minimized. 7) Finally, detectors with low dark count rate should be used. Silicon Avalanche photodiodes (APD)

have dark count rate smaller than 10 counts / sec way below the usual single molecule count rate.

4.3. Single molecule detection

4.3.1. Single molecule imaging

Typical sample preparation for single molecule spectroscopy includes conjugation of fluorophores to single strands of DNA molecules. For dual color spectroscopies, two complementary DNA strands with different conjugated fluorophores are hybridized. A glass coverslip is cleaned in HF solution to remove impurities and is silanized in 2% 3-aminopropyl-triethoxysilane (United Chemical Technologies) solution by dipping for two minutes. 1μL of dilute DNA solution (with concentration of 1nM to 100nM) is spread on the coverslip and then washed away in distilled water. This procedure ensures the adsorption of the DNA-fluorophore complex on the silanized surface.

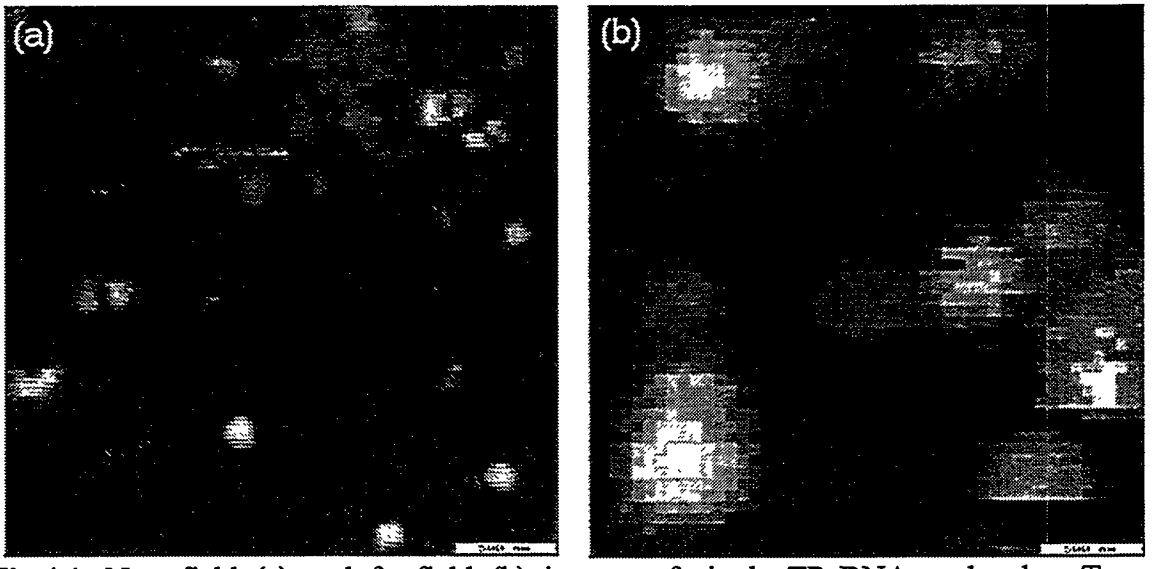

Fig.4.1. Near-field (a) and far-field (b) images of single TR-DNA molecules. Two figures are on the same scale, and the scale bar is 500nm. Linearly polarized light along the horizontal axis was used for excitation.

In Fig.4.1, we present fluorescence images of TR-DNA molecules on a dry silanized surface obtained with near-field excitation (a) and far-field excitation (b). Different samples were used for two images. Images were taken by scanning the sample with respect to near-field fiber probe or the focused laser spot and the resulting emission is recorded using an APD as a function of sample position, and this map results in the image. Since the physical dimension of the molecule is smaller than the laser spot, it acts as a point dipole mapping the electric field distribution near the tip or near the focal spot. Note that the spot size is 4 times larger for far-field case, and larger average separation between molecules is required, that is, 16 times more dilute sample is needed.. For a single pair of molecules used in Chap.6, two complementary single strand DNA molecules are hybridized to form the pair complex in the buffer solution. Since the hybridization is a dynamic equilibrium process, molar density above 200nM is necessary to insure good hybridization. The resulting density on the coverslip is too high even for near-field measurement, and lower concentration solution has to be spread in a cold room.

Tip morphology plays an important role in the point response function of a single molecule, and an example is shown in Fig.4.2. For different imaging conditions, spots have different shapes sometimes yielding higher resolution than the nominal aperture size. These images were taken on Coumarin 540 molecules dispersed on PMMA coated glass coverslip, the first single molecules we studied. In that stage of development, we did not know how to make good quality tips and very often we obtained tips with low enough background level and high enough throughput but with poor morphology. In Fig.4.2, single molecule response is a spot with 150nm width for one excitation polarization (a), but the response becomes more complicated for another excitation polarization (b). While some molecules have similar responses as in (a), some show up as two very small spots each of 35nm width. Even though we may get unusually high spatial resolution with a non-ideal tip under certain conditions, the interpretation of the image is complicated.

Furthermore, one cannot hope to reproduce the tips with the same morphology even if the electric field distribution around the tip is well understood. Note that two spots are all aligned for each molecule on the image that display two spots. Excitation polarization was not measured and the arrows are shown on two images just to show that the input polarization was changed.

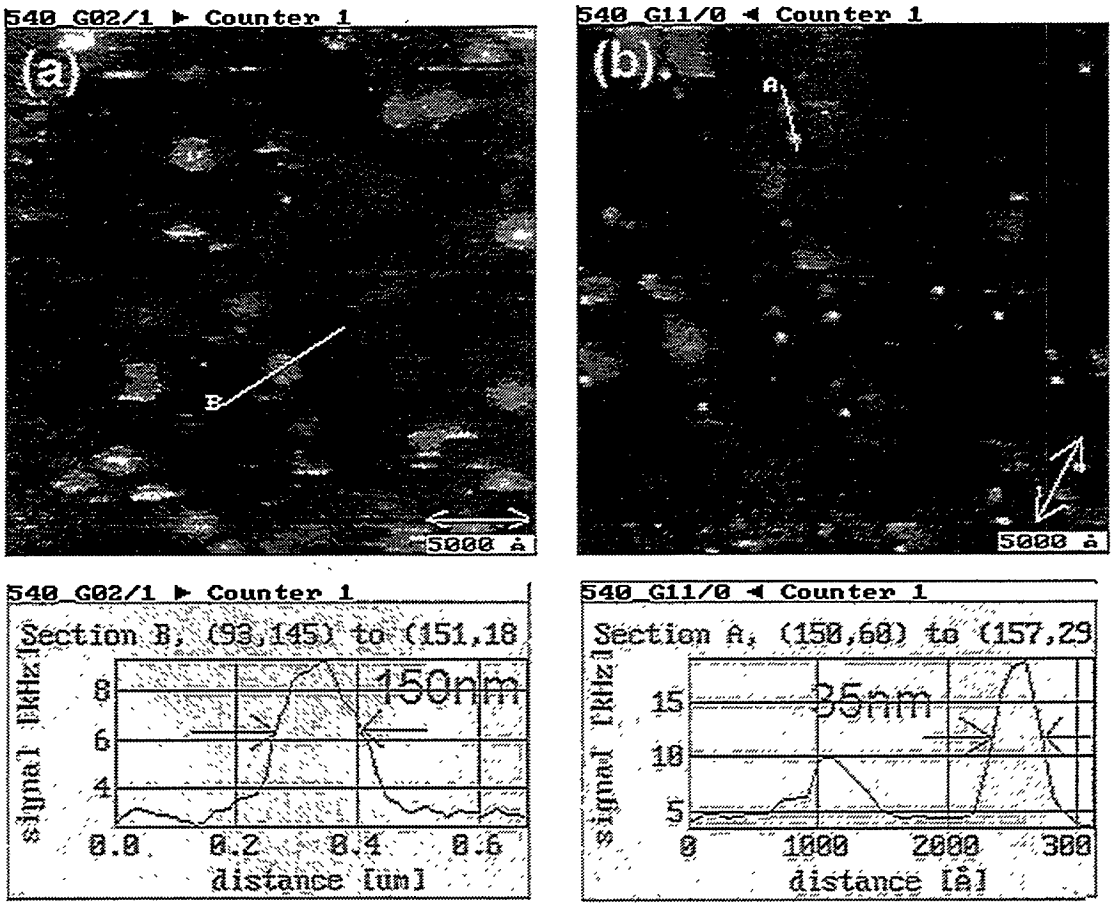

Fig.4.2. Artifacts due to imperfect morphology of NSOM tip. On one polarization of excitation (a), single molecules show up as 150nm spot, while on the other polarization (b), some molecules show up as two spots of each 35nm size.

These complicated responses are likely due to the bad coatings with aluminum resulting in clumps and molecules with various dipole orientation will sample the electric field near the tip differently. Two different responses in (b), single large spot and double tiny spots, are resulting from two different dipole orientations. However, the exact dipole orientation for each case cannot be known because the morphology of the tip, hence the

electric field distribution around the tip, is not known. Tips with better defined morphology can actually map the molecular dipole moment. The z-component or surface normal component of the dipole moment samples the evanescent field near the tip which is orthogonal to the propagation direction. It was shown by Betzig that the dipole orientation can be fully determined in three dimension by analyzing the images for a few different excitation polarizations (Betzig and Chichester 1993). In this kind of analysis, the electric field distribution around an aperture on a perfectly conducting and infinitesimally thin screen calculated by Bethe (Bethe 1944) is used to reproduce the experimental result. As an example, in Fig.4.1a, we see two lobed structures along the direction of linear polarization. This means that these molecule have dipole mostly normal to the surface. Trautman et al. (Trautman and Macklin 1996) took both near-field and far-field images of the same set of molecules and the molecules showing two lobes in the near-field image showed up as weak disks consistent with the primarily surface normal dipole orientation.

4.3.2. Proof of single molecule

Betzig's criteria for single molecule detection (Betzig and Chichester 1993) include: (1) measured areal density of fluorescence spots consistent with the sample preparation; (2) signal level comparable to what is expected from the known extinction coefficient of the molecule; (3) Strong polarization effects indicating single molecular dipole moment; (4) sudden photodestruction.

The first criterion is only half satisfied because the sample preparation itself is not well understood. We spread a dilute solution of fluorophore-DNA molecules on a silanized surface and wash away unbound molecules with water. Since we do not know the binding yield, we have no way of estimating the areal density a priori. However, as we

scale down the density in solution all the way down to the level where no aggregates can be formed at all in solution, the areal density of the molecules in the image scale linearly with the solution density.

Signal level for typical excitation intensity is around 20 counts/ms, more or less consistent with the expected signal level calculated before, but with a strong variation among molecules mainly due to differences in the spectrum and the dipole orientation. In the far-field case, the background is about 0.5 counts/ms and is likely due to the auto-fluorescence from the glass coverslip. Background fluorescence from other optical elements are negligible because in con-focal detection scheme, only photons arising from the focal spot is imaged on the detector. For this background level, shot noise limited single molecule detection is possible within 5ms integration time. In the near-field case, the background is usually above 1 counts/ms and sometimes as high as 50 counts/ms strongly dependent on the tip. Luminescence from the fiber polymer coating and silica Raman from the optical fiber itself are likely sources of these background and they can completely dominate the signal from a single molecule. So far, we have not been able to control the level of this background in a reproducible way. Unlimited excitation intensity, the excellent S/N and the ease of use are reasons why the far-field excitation is favored over the near-field excitation when the extra spatial resolution of the near-field case is not necessary.

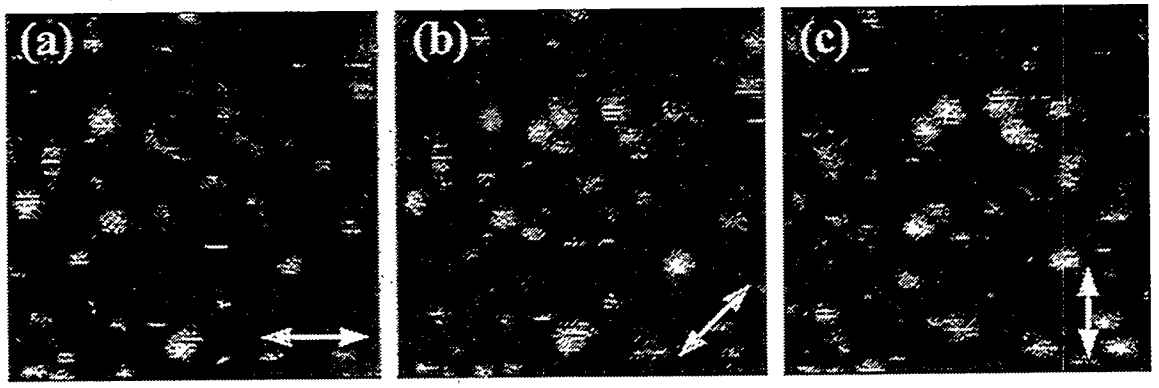

Fig.4.3. Polarization dependence of molecular excitation. Three simultaneous images of TR-DNA molecules taken with three different excitation polarizations (arrows).. Each polarization selects a different set of molecules.

Strong dipole dependency can be seen in images taken with different excitation polarizations. Fluorophores preferentially absorb or emit photons polarized along the transition dipole moments. The transition dipole moments in the absorption and in the emission in general differ by a small angle, (for example, the angle is 13° for rhodamine 6G) and both dipole moments are likely lying on the molecular plane. Below, "dipole moment" means the transition dipole moment in absorption unless specified otherwise. In Fig.4.4, three fluorescence images of single TR-DNA molecules on silanized glass coverslip taken with three different polarizations (0°, 45°, 90°) are shown. The images are taken in parallel, each line being scanned three times, once for each polarization, before the next line is scanned. This insures that the contrast is not due to mechanical drift. Different sets of molecules are selected for each image. Because of the unique dipole moment of each molecule, the in-plane component of the dipole orientation, θ, may be unambiguously determined in the following way.

$$|\tan\theta| = \sqrt{\left| I_y / I_x \right|} \tag{4.3}$$

where I_x, and I_y are signal intensities for x (0°) and y (90°) polarized excitation. θ is measured relative to x direction. Ambiguity in the sign determination is resolved by signal intensity for 45° polarized excitation. When the z component of the dipole is not negligible, it should be possible to determine that component by near-field imaging with a well-characterized tip. Total detection efficiency of the fluorescence emission, especially the collection efficiency with the objective, can depend on the emission dipole orientation. However, for high numerical aperture objective, the collection efficiency is known to be nearly independent of the emission dipole orientation. Therefore, the z component of the dipole moment could be inferred from the detected emission intensity if

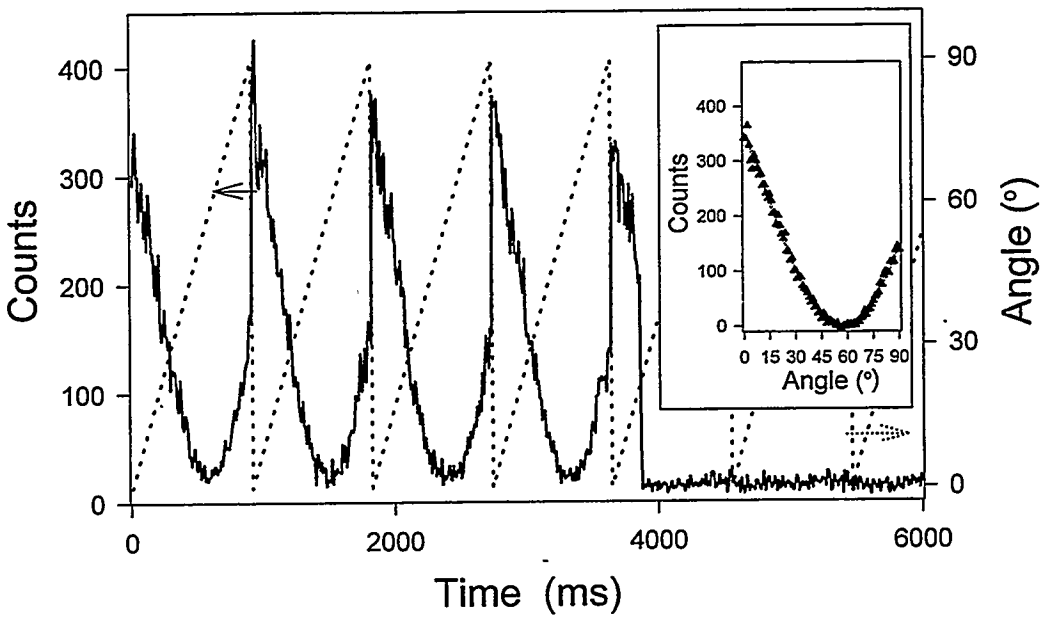

Fig.4.4. Fluorescence time trace of a single TR-DNA molecule (solid line) and instantaneous excitation polarization angle (dotted line). For each period, the signal follows the expected cosine square function. The emission stopped during the fifth period because of photodestruction. The inset shows the average over the first four periods together with the fit to the cosine square function.

other conditions such as absorption cross section and quantum yield are the same. Macklin et al. (Macklin et al. 1996) estimated the absorption dipole orientations relative to the plane based on the peak intensity for molecules with the same emission spectral peak position. They found a good agreement with the emission dipole orientation determined from the fluorescence lifetime.

Another way of measuring dipole orientation is to measure the signal as a function of polarization when the molecule is under the excitation spot. Güttler et al. (Guttler et al. 1993) used polarization modulation in excitation spectroscopy of pentacene molecules in p-terphenyl to distinguish between two different defect sites in the crystal. Only in-plane component can be measured, but this can provide a good way of studying the dynamics.

In Fig.4.4, an emission time trace (solid black line) from a single TR-DNA molecule is recorded while the linear excitation polarization is repeatedly rotated from 0° to 90° (Ha et al. 1996c). The intensity of the emission signal is proportional to the absorption, which, according to the dipole approximation, is proportional to $|\vec{\mu}\cdot\vec{E}|^2$ where $\vec{\mu}$ is the molecular absorption transition dipole and $\vec{E}$ is the laser field. The data follows the cosine square function very well indicating a fixed orientation of a single dipole moment. In fact, most of the molecules (>97%) studied in this way showed the fixed dipole moment throughout the observation period suggesting that the binding of the molecule to the surface is stronger than the thermal energy at the room temperature. Occasionally, we do see cases where a molecule desorb from the surface and readsorb with a different orientation after a period of free rotation. This could be due to the weak binding that can be easily perturbed either by the thermal energy or by the laser induced conformational change or heating. This technique can be used to unambiguously distinguish between different types of dynamic events and to understand the nature of the rotational jumps (See Chapter 5). While it is possible to get an apparent single dipole effect from self-aligned aggregates of molecules, the degradation of the emission due to photodestruction from such aggregates is gradual because the photodestruction happens at different times for each molecule. In contrast, for the photodestruction of a single molecule, the time trace data shows sudden and complete drop of the emission to the background level.

Photodestruction of fluorophores is one of the most important yet least understood process that impact the application of fluorescence in biology. Photodestruction is often dependent on the presence of molecular oxygen that reacts with the triplet excited states to produce highly reactive singlet oxygen. To decrease the photodestruction yield, it has been common practice to reduce the concentration of oxygen, for example by adding antioxidants. Photodestruction quantum yield of 10^{-5} to 10^{-7} is common for fluorophores in various environments. Photodestruction quantum yield should be independent of the excitation intensity unless there is an accumulative effect. In fact, Trautman et al.

(Trautman and Macklin 1996) found out that the yield increases with intensity for near-field excitation, presumably due to the increased temperature of the probe tip. At the typical emission rate, many molecules do not survive more than a second of exposure, while some molecules live as long as a few minutes showing strong inhomogeneity in the photodestruction lifetime. The effect of sudden photodestruction shows up in scanned images as incomplete spots(Fig.4.1).

4.4. Single molecule spectroscopy

4.4.1. Introduction

Some molecules live long enough for the emission spectrum to be measured. To get reasonable spectra, a large number of photons need to be detected. For example, to record a 40nm width spectra with 1nm spectral resolution and with 200 counts maximum, roughly 8,000 counts have to be registered by the CCD camera. Total detection efficiency, defined as the number of TTL pulses generated by the avalanche photodiode per an emitted photon, is about 10% in our system. For CCD, the efficiency is reduced by a factor of 10, because half of the photons are lost inside the spectrometer and only one count is registered for five photons detected. Therefore, it takes close to 1 million emitted photons to measure a good emission spectrum. Since typical signal level at APD for near-field excitation is on the order of 10 counts/ms, or 100,000 photons emitted per second, the integration time has to be on the order of 10 seconds. The first single molecule emission spectra were taken with 1 minute integration time at a lower intensity to avoid any overheating effect on the near-field tip (Trautman et al. 1994). We were able to get good quality spectra with 5 second integration time with the near-field excitation (Ha et al. 1996e), and better time resolution is expected in the far-field excitation. Good time

resolution is required to study dynamics happening on a short time scale. But, if the dynamics is light induced, not much is gained by going to higher excitation rate. On the other hand, if the spectral change is independent of the excitation, and is rather controlled by other factors such as biochemical reactions, a lot more can be learned by using high excitation and short integration time.

Unlike in low temperature SMS, the emission spectra of single molecules are broad, and in fact, almost as broad as that of many molecules in solution. This is due to the fact many nearby vibrational and rotational levels of the multi-atom system contribute to the main electronic transition.

4.4.2. Single molecule emission spectrum

To take a single molecule emission spectrum, the molecule has to be located under the near-field tip or within the confocal spot. Both manual and automatic positioning have been used to locate molecules. Since automatic positioning takes far less time, and therefore, less excitations, more molecules can be studied before the photodestruction. With automated positioning that we have developed (see Appendix A), we were able to investigate molecules in less stable environments, shorter photobleaching lifetime and more frequent spectral jumps. (See Appendix A)

A scheme of taking single molecule emission spectra manually is shown in Fig.4.5. First, an image is taken to make sure that the molecule of interest (molecule B in this case) is well isolated from others. Then the sample is moved to bring the molecule under the tip. The signal level must be monitored during this process because of the scanner hysteris. Then, the flipping mirror after the pinhole of the microscope is turned toward the spectrometer, and a series of emission spectra are taken until the acquisition is manually stopped after the molecule photobleaches. An electronic shutter at the laser path is

synchronized with the spectrum acquisition to minimize unnecessary exposure during the data transfer and display. Another image of the same area is taken and shows that indeed the molecule B is missing from the image.

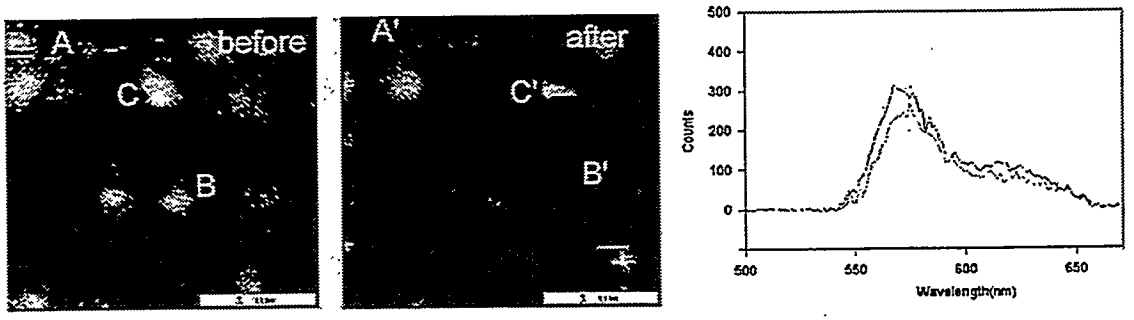

Fig.4.5. Acquisition of single molecule emission spectrum. After the first image on the left hand side, a series of emission spectra are taken on the molecule B until it photobleached. On the next image, the molecule B is missing. Molecule A photobleached within the first image, and the molecule C died in the middle of the second image.

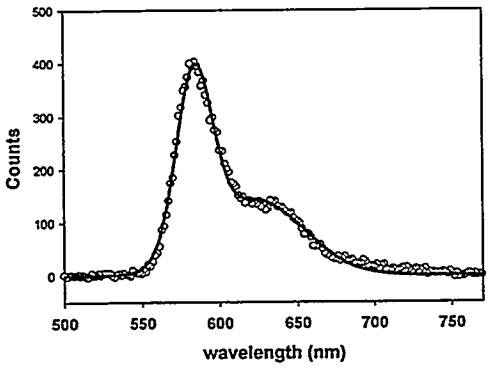

Fig.4.6. Emission spectrum of a single TR-DNA (empty circles). Solid line is a two-gaussian fit to the data. Integration time = 5s.

A typical emission spectrum of a single TR-DNA molecule is shown in Fig.4.6. In general, the spectrum is not symmetric and has a long wavelength hump due to a vibronic band. The spectrum can be fit well by a combination of two gaussians for the main and vibronic band transitions. Strength of the vibronic band relative to the main transition varies among molecules, and exemplifies the difference in the coupling between the electronic and nuclear degrees of freedom in different local environments.

The main peak position has variations up to 50nm among molecules or within the same molecule as a function of time. Full width half maximum of the main peak ranges

from 20nm to 40nm, and part of the broadening could be due to multiple spectral jumps within the integration time.

The emission spectra measured on single molecules have peaks at higher energies than in ensemble measurement in solution. In solution, the solvent rearranges in reaction to the increased dipole moment of the fluorophore after absorption. If the solvent rearrangement happens faster than the emission lifetime, equilibrium state of the surrounding solvent molecules can be reached within the excited state lifetime, and this results in additional red shift of the emission. However, if solvent relaxation is comparable or slower than the excited state lifetime, one can observe different spectra that are less red shifted and often broadened. This effect can be best seen in vitrified solvents at low temperatures. For molecules at the air-solid interface, such solvent relaxation in the literal sense should not occur, explaining the blue shift of the emission relative to that of the solution. We will discuss spectral jumps in Chapter 5. Pure change of solvent relaxation rate would not change the absorption spectrum because the absorption occurs in a shorter time scale ($< 10^{-15}$ s). However, we almost always observe that the spectral jump also changes the total signal or absorption cross section at the excitation wavelength. Therefore, we eliminate the change of solvent relaxation as the possible source of spectral jumps.

5. SINGLE MOLECULE DYNAMICS

5.1. Introduction

The room temperature laser induced fluorescence (LIF) spectroscopy of immobilized single molecules was recently made possible with near-field and far-field excitations (Ambrose et al. 1994a; Ambrose et al. 1994b; Betzig and Chichester 1993; Bian et al. 1995; Ha et al. 1996c; Ha et al. 1996e; Meixner et al. 1995; Trautman et al. 1994; Xie and Dunn 1994). The dynamic aspects of single molecule spectroscopy (SMS) are of particular interest for many applications including biology. It has long been suggested, and to some degree demonstrated, that single fluorophores can act as molecular probes by "reporting" on their immediate environment. Unlike in ensemble fluorescence measurements, where dynamics is washed out due to averaging over many molecules, individual dynamic events involving single fluorescent labels such as conformational changes of a biological macromolecule should be observable. However, fluorescence from a single fluorophore displays rich dynamics associated with its own molecular properties, and extreme care must be taken before SMS can be applied for dynamical studies of biological macromolecules. It is therefore important to understand the properties and the dynamics of single fluorophores under ambient condition. Such understanding will provide the tools to distinguish fluorophore dynamics from macromolecule dynamics.

In this chapter, we discuss the dynamics of single fluorophores bound to silanized glass surface by DNA molecule. Dark state, spectral jumps, individually resolved quantum jumps to triplet state, and rotational jumps are reported. Polarization modulation technique help us understand these processes, and such capability of observing and

identifying various dynamic processes should prove useful in the future applications of single molecule spectroscopy.

5.2. Dark state and spectral jumps.

5.2.1. General background

Spectral drift of single molecules has been studied intensively for single molecules at cryogenic temperatures, and the underlying mechanism is well understood. Ambrose et al. (Ambrose and Moerner 1991) measured fluorescence excitation spectra of single pentacence molecules doped into p-terphenyl crystal and found out that the transition frequency of some of the individual pentacene molecules fluctuated on the time scale of seconds. This spectral diffusion behavior was found independent of the excitation intensity, and therefore, it was concluded that it was spontaneous and not light-induced. Reilly et al. (Reilly and Skinner 1993) developed a model in which each configuration of the central phenyl ring of p-terphenyl molecule is discussed as a two level system (TLS). Their model of surrounding TLSs, affecting the resonance frequency, accounts for the experimental observation qualitatively. The spectral diffusion is caused by the reorientation of the central phenyl ring and this reorientation can only occur at a wall between domains of different central phenyl ring ordering.

Another class of spectral changes, often referred as hole burning, was observed for low temperature single molecule studies in amorphous solid (Basche and Moerner 1992). In hole burning process, the absorption line simply appears to vanish as the resonance frequency shifts way from the laser frequency. Hole burning is light-driven in contrast to the spontaenous spectral diffusion. The amount of spectral shift due to hole-burning is usually very large ($>100cm^{-1}$).

Spectral jumps of single fluorescent molecules have also been observed at room temperature and their mechanism have not been well understood. In the first SMS at room temperature, Trautman et al. (Trautman et al. 1994) showed that the emission spectrum shifts up to 10nm for DiI molecules on PMMA matrix. Xie et al. (Xie and Dunn 1994) initially reported the fluctuation of single molecule emission intensity which they conclude to be due to spectral shift. They eliminated the possibility of molecular reorientaion as a possible source by modulating the excitation polarization between two discrete values 0° to 90°.

Dark state of single molecule emission is a reversible cessation of the emission for a time scale ranging from a millisecond to a few second. It has a similar characteristics as the hole burning at low temperature SMS, and has been seen by a number of researchers (Ambrose et al. 1994a; Ha et al. 1996c; Trautman and Macklin 1996).

Spectral jumps and dark states are the main sources of molecular emission fluctuations. To study them, we have developed two distinct and complementary techniques: emission spectroscopy and two channel time traces.

5.2.2. Two types of spectral changes: Emission spectrum.

Spectral changes of single molecule emission can be seen the best by measuring the fluorescence emission spectrum using a spectrometer and a CCD camera. It takes about 5 seconds to obtain reasonable spectrum under near-field excitation, and if the spectral changes are happening on a comparable or longer time scale, they can be observed in a series of emission spectra taken consecutively (Fig.5.1). If the spectral changes are happening spontaneously, independently of the excitation intensity, those with shorter time scale can be observed by reducing the integration time and increasing the excitation intensity. But, if these changes are light induced, this approach does not work. Therefore,

in an attempt to observe spectral changes of shorter time scale, we employed a new approach using two channel detection (Fig.5.3).

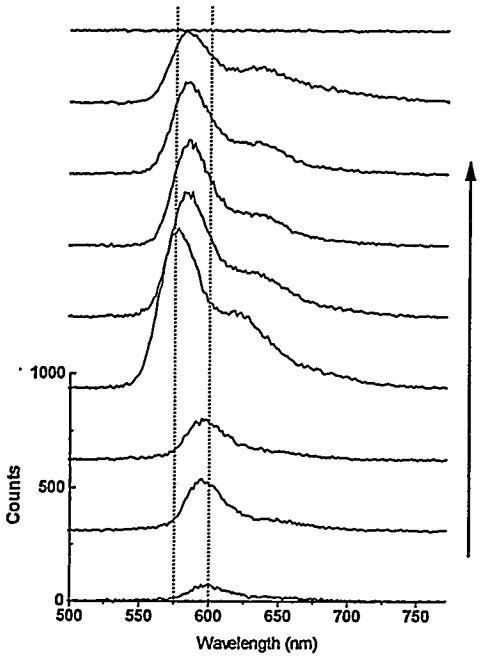

Fig.5.1. Spectral drift of single TR-DNA molecule. Consecutive emission spectra of 5 sec duration are obtained until the photobleaching. The arrow denotes the direction of time. Two dotted vertical lines at 575nm and 600nm represent the extremes of the peak position.

The molecule in Fig.5.1 shows a series of spectral jumps toward blue and toward red before the photodestruction in the 8th scan. The general shape of the spectrum, the peak position and the total intensity change as a function of time. In particular, the bluer the spectrum is, the higher is the total intensity. This is evidence that the absorption spectrum follow the emission spectrum. The laser line excite the molecule at the short wavelength tail of the absorption curve, and the blue shift of the absorption brings the laser line closer to the absorption maximum. Therefore, the absorption, and hence the total signal, increases for blue shift.

A spectral change of a different type is shown for the molecule in Fig.5.2. The spectrum did not change between scan 1 and 2, but changed between scan 2 and 3. It then stayed the same during scan 3, 4 and 5. Averaged spectra for scan 1, 2 and scan 3, 4, 5 are plotted. The secondary peak is very pronounced in this case, and the relative weight between the main peak and the secondary peak changed abruptly between scan 2 and 3. The main peak decreased while the secondary peak increased. The total emission intensity stayed roughly the same, suggesting that the absorption cross section at the laser wavelength did not change, or that the absorption spectrum did not move.

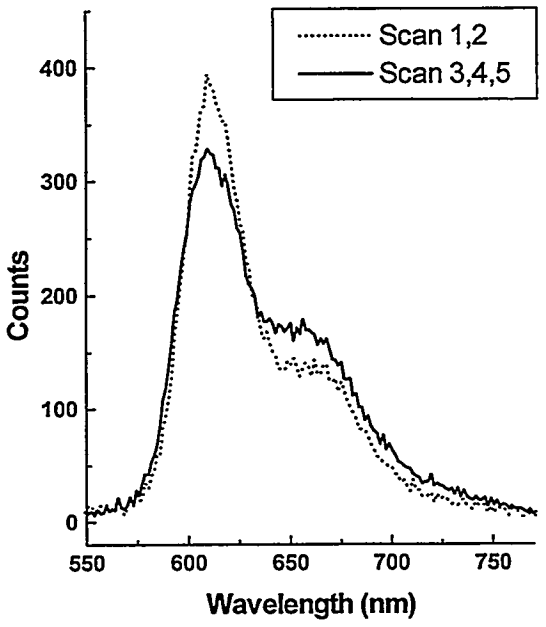

Fig.5.2. Competition between two components.

These data (Fig.5.1 and Fig.5.2) were taken with near-field excitation and manual positioning of molecules under the tip. Since the amount of exposure required for manual positioning is enough to destroy a molecule before any spectrum is taken, these spectra were taken on molecules with exceptionally stable environment. Even in these cases, we often see spectral broadening likely due to multiple spectral jumps within the integration time. Also, the interpretation of the intensity of the spectrum is often tricky because unresolved dark states, rather than absorption quantum yield changes, could produce intensity fluctuations. Therefore, there is definitely a need for a method capable of studying spectral changes with better time resolution.

5.2.3. Correlated dark state and spectral jump: Two channel detection

To study the spectral jumps and dark states and possibly correlation between them, we used two channel detection. This is performed by splitting the emission with a dichroic mirror centered at the peak of the average emission spectrum (See Fig.5.5c for illustration). To study even the flickering molecules, automated search was done at low intensity using long integration time (10 ms) (See Appendix A). Once the molecule is located, the intensity is increased ten fold and emission is measured in two channels (long wavelength and short wavelength) with 1 ms integration time.

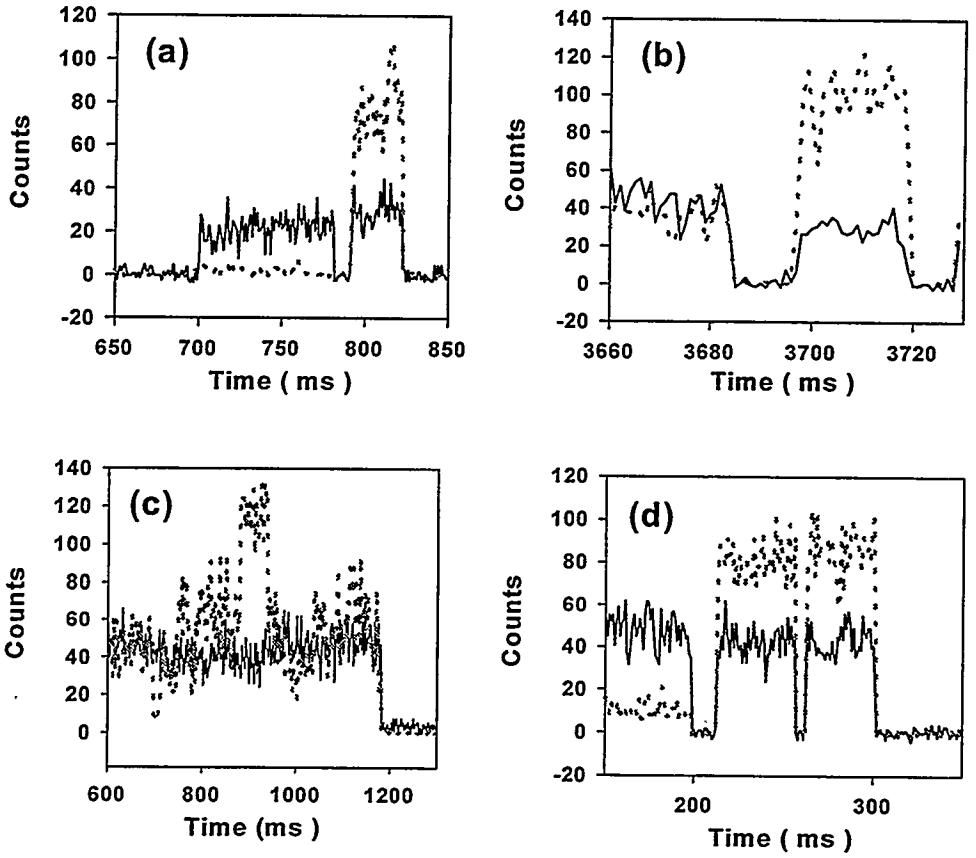

Fig.5.3. Spectral jumps and dark states. Time evolution of a single TR-DNA measured in two channels (long wavelength channel in solid lines and short wavelength channel in dotted lines). The change in the ratio means a spectral jump. Spectral jumps are often accompanied by trips to dark states.

Typical data is shown in Fig.5.3. Ratio between the short wavelength channel and the long wavelength channel increased when the molecule returns from the initial dark state in (a), (b) and (d) indicating that the emission shifted toward blue.

Note the increase of total emission upon blue shift again suggests that the absorption spectrum shifted toward blue as well. These spectral changes happen instantaneously within the time resolution. The correlation between the dark state and the spectral jump suggests that this type of spectral jump is related to the dark state. The correlation is not

perfect since there are discrete spectral jumps with no apparent dark states (c) and dark states without spectral jumps (d).

5.2.4. Dichroic mirror response

Two channel detection, utilizing dichroic mirror, is helpful for studying fast spectral jumps although spectral resolution is sacrificed. If we know a spectral shape, however, we can model the dichroic response for a dipole orientation and a spectral peak position. This in turn can be used to deduce the peak wavelength from the observed two channel signal.

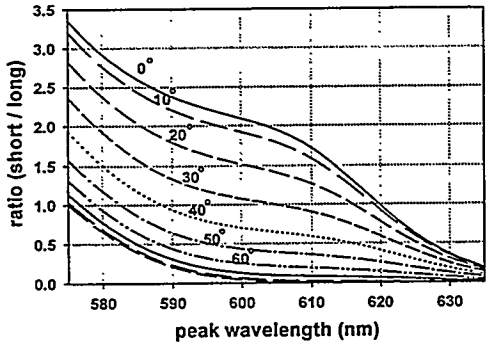

Fig.5.4. The response of the dichroic mirror for the molecular emission. The curves are plotted for every 10 degree from 0 to 90 degree.

Fig. 5.4 shows the dichroic mirror response curves. There are ten curves for ten different dipole orientations, θs ranging from 0° to 90°. Each curve represents the ratio between two channel signal vs. peak wavelength of the emission spectrum, λ_{peak}.

We have modeled the emission spectrum as the sum of two gaussian peaks, main peak at λ_{peak} with a width of 25nm and the second peak at (λ_{peak} + 60nm) with a width of 50nm and 25% of the first peak intensity. For the dichroic response, two different transmission curves for s and p polarizations are approximated by piece-wise straight lines. We also assume that the emission from the molecule is fully polarized along the emission dipole moment direction. To obtain the integrated transmission and reflection of the emission for each λ_{peak} and θ, the transmission/reflection for the s and p component of the emission are independently evaluated. The result immediately tells us that the ratio signal is extremely

sensitive to the angle and even more so close the dichroic cutoff. Unless θ is known, λ_{peak} cannot be deduced from the ratio alone.

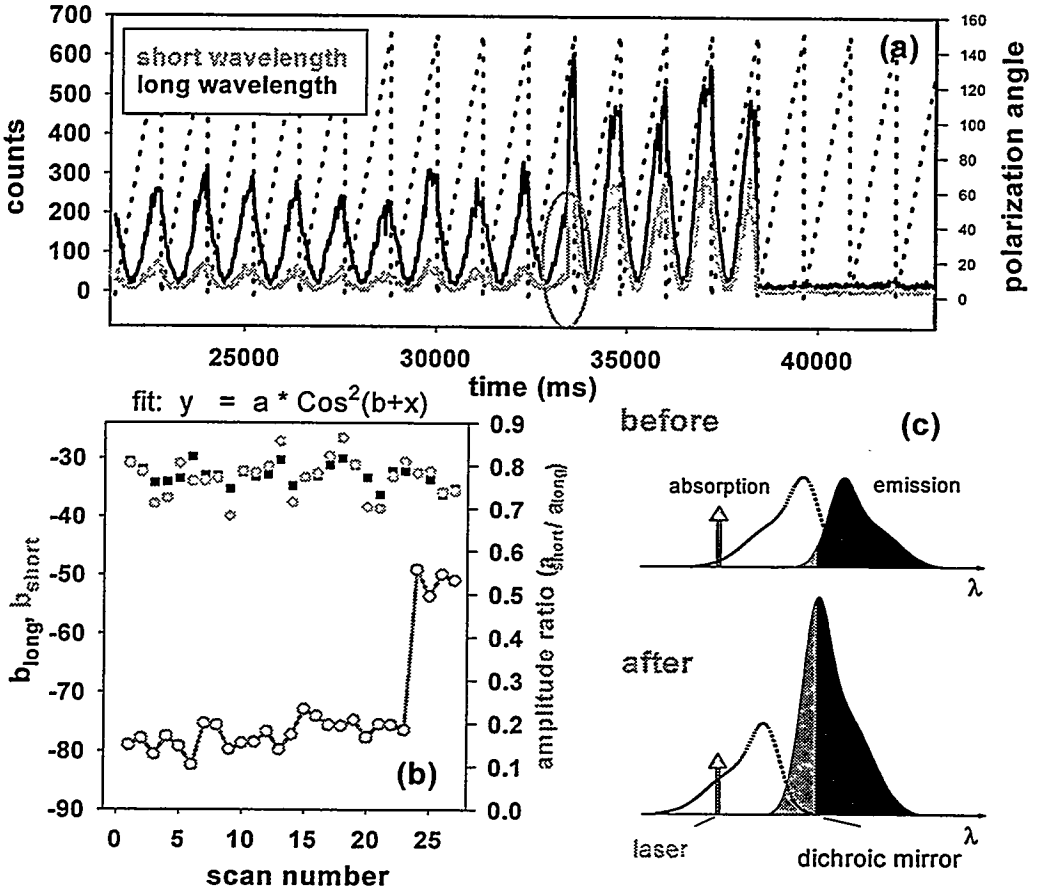

Fig.5.5. Spectral jump independent of rotation. Single TR-DNA emission is monitored in two channels (long wavelength channel in black and short wavelength channel in gray) as the excitation polarization is repeatedly modulated (a). Each curve follows the expected cosine square curve and after fitting each period to a* $\cos^2$(b+x), the resulting phase b for each channel and the amplitude a ratio is plotted in (b) as a function of the scan number. After a spectral jump toward blue at about 34th second, the ratio jumped from 0.2 to 0.5 and the total signal increased threefold while the phase didn't change. The increase of the total emission upon blue shift can be explained by the increase of the absorption. (c)

5.2.5. Spectral jump is not caused by physical rotation.

Fig.5.5 is an example for a spectral jump, which can unambiguously be distinguished from dipole rotation. The emission of a single TR molecule was separated by a dichroic

mirror and was simultaneously monitored in two channels while the excitation polarization was modulated. Fig.5.5a shows the two time traces, starting at scan 15. The signals on both channels were fit to $a*\cos^2(x + b) + c$ for each modulation period. In Fig.5.5b, the ratio a_{short}/a_{long} (solid line, filled circles) is plotted as function of the modulation period number. The phases of both signals, b_{short} and b_{long} are also plotted in black squares and gray triangles respectively. In scan 24, the total emission from the molecule increased threefold and the amplitude ratio abruptly changed from 0.2 to 0.5 with no apparent change in the phase (and hence, no rotation). In general, a change in the counts ratio can come either from spectral changes or from reorientation of the dipole moment (see Fig.5.4). This latter case is due to the strong polarization dependence of the dichroic mirror. While spectral jumps exhibit only a change in the relative intensity between the two channels, dipole reorientation exhibits a change in the phase of the modulated signal as well, as shown below in Fig.5.19. Therefore, the modulation technique can distinguish between spectral jumps and orientational effects. Since the dipole did not rotate, the data can only be explained by a spectral jump toward the blue. Fig.5.5c illustrate the relative alignment of the absorption and emission lines before and after the spectral jump, the excitation laser wavelength and the dichroic cut-off. The threefold increase in the total signal is due to the blue-shift in absorption, which increases the absorption at the excitation wavelength, and hence the total emission. As the emission also blue-shifts, the intensity in the short-wavelength channel increases more than in the long-wavelength channel, and therefore increases the ratio a_{short}/a_{long}. Moreover, by using the dichroic response curve generated for typical TR-DNA spectrum (Fig.5.4), we could extract the peak position of the emission spectrum from the measured absorption dipole orientation and from the measured ratio between the two channels (here we assume that the absorption dipole and the emission dipole are closely aligned). From this analysis, we conclude that the peak position of the emission spectrum jumped from 633 nm to 623nm.

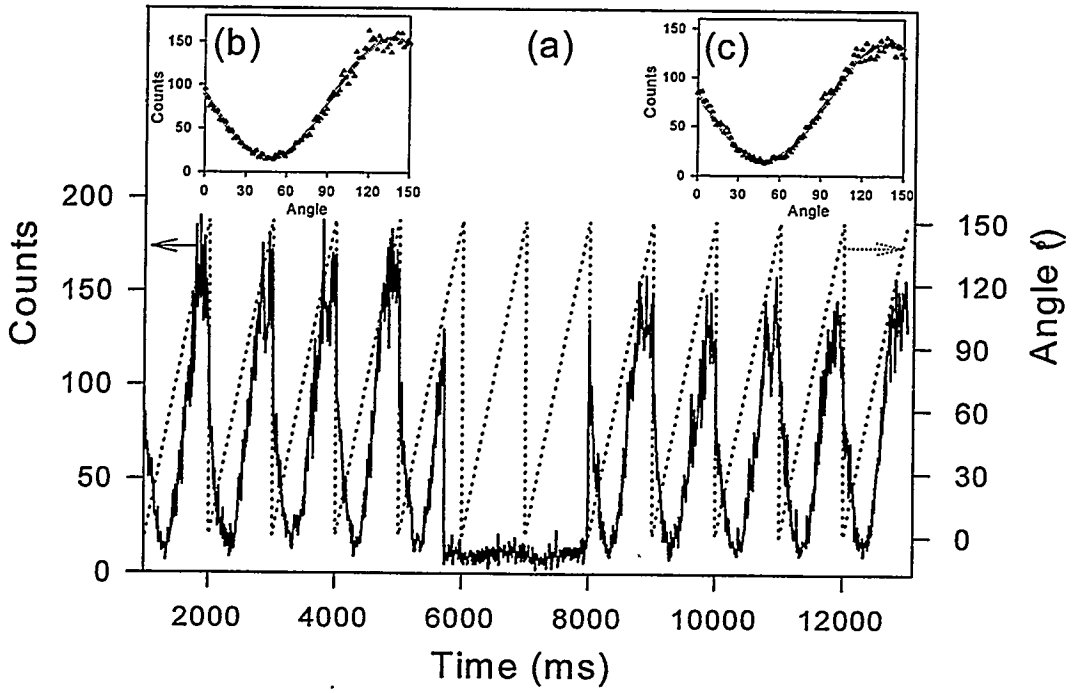

Fig.5.6. Dark state doesn't involve rotation. (a)Total emission of a TR-DNA molecule is recorded as the excitation polarization is rotated from 0 to 150 degree repeatedly. The emission is interrupted due to a dark state for about 2 seconds, and when the emission resumes, the phase, or the orientation of the molecule didn't change. In the inset, the average signal with the fit before the dark state (b) (c) for after the dark state.

5.2.6. Dark state is not caused by physical rotation.

There are several possible causes for the interruption of emission. Spectral diffusion leading to zero absorption, often observed for extremely narrow absorption lines at the low temperature is unlikely at room temperature. We have found spectral diffusion is in general 10-25 nm or less and is smaller than the width of the spectrum. Hence, the spectral changes can hardly stop the emission completely. Interaction with metal-coated tip used for excitation can affect the emission intensity. However, this is also not likely the cause of the dark-states since the tip-effect does not lead to such on/off behavior. In

addition, we see similar effects using far-field excitation. Rotation that bring the molecular dipole completely out of excitation polarization plane could result in the dark state, but the following experiment rules out that possibility.

Fig.5.6a shows an emission time trace of a TMR molecule (solid line) which undergoes a transition to a dark state. The molecule stopped emitting light from 5.7 sec to 8 sec. The average of the first 4 modulation periods before, and the last 4 periods after the dark state, are plotted in insets Fig.5.6b and Fig.5.6c, respectively, along with curve fits. The data clearly demonstrates that the phase of the modulated signal is the same before (b = -42.8±0.8°) and after (b = -41.3±0.8°) the transition to the dark state. This shows that the dark period does not originate from a rotation, but from a transition to a non-emitting state.

The exact nature of this dark-state is not well understood, although it is probably not a metastable triplet state since these have lifetimes in the millisecond not in the second range. It is likely that the fluorophore undergoes a reversible chemical reaction — possibly oxidation or proton abstraction which reduces the oscillator strength of the molecule but does not cause irreversible bond-breakage of the conjugated aromatic system.

5.2.7. Light induced or spontaneous?

The origin of the spectral jumps and dark states is not understood at the moment. They could be due to spontaneous or thermally activated changes of the environment, or light induced conformational changes. Although the detailed mechanism is not known, one can wonder if these events are light induced or spontaneous. An ideal measurement would be to measure these events from the same molecule for different excitation intensities. Such measurement is, however, difficult to perform because the poor

photostability does not allow for multiple exposures. Here, we present an alternative way to address this question.

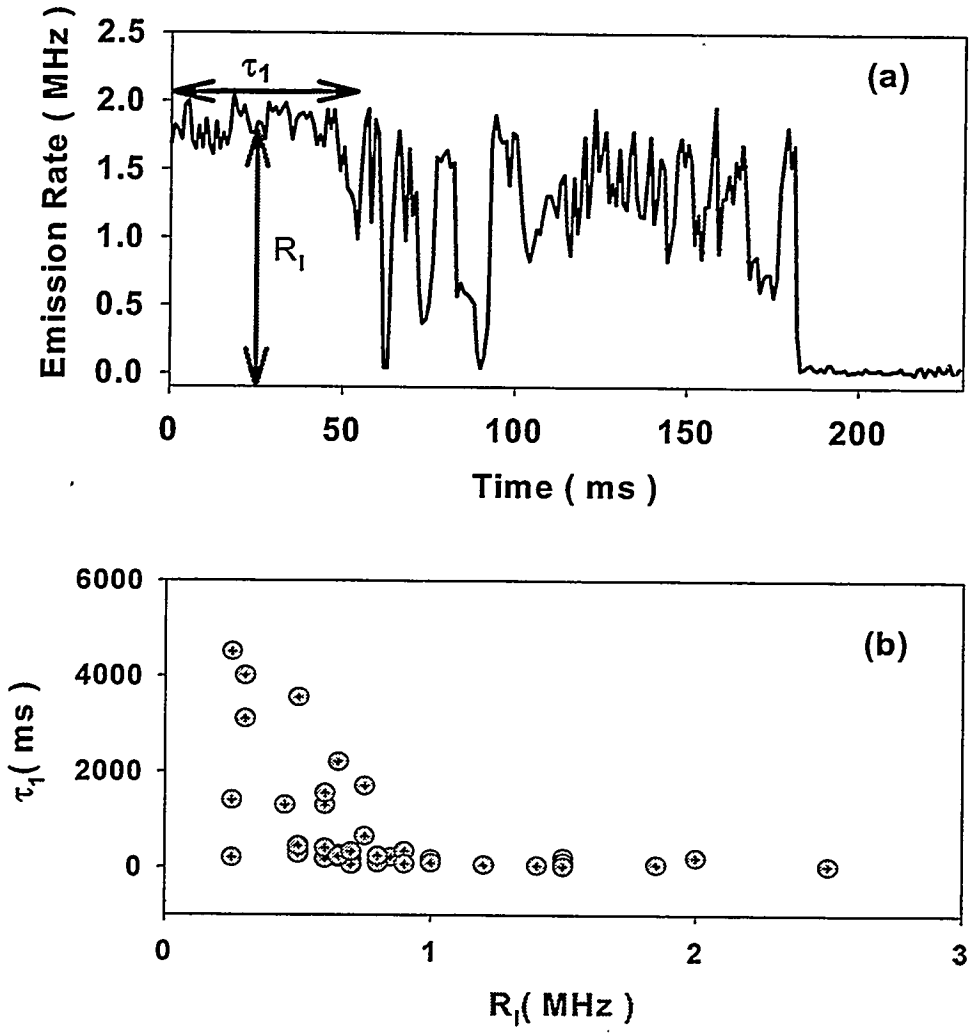

Fig.5.7. Top curve (a) shows the total emission from a TR-DNA molecule monitored until the photobleaching. The initial emission rate R_I and the time it takes until the first event τ_1, spectral jump or dark state, are measured for 42 molecules and the result is plotted on the bottom curve (b). Each point comes from one data trace such as shown on the top graph.

About 60 % of the molecules experience this type of dark states or discrete spectral jumps before permanent photodestruction. Fig.5.7a shows the total emission from a TR-DNA molecule monitored until the photobleaching. While it starts with relatively quiet signal, after 50ms the emission shows large fluctuations due to dark states and spectral

jumps. Such a change from quiet to noisy behavior was seen on many molecules. Two parameters are extract from Fig.5.7a: The initial emission rate, R_I, and the time it takes until the first event, τ_1. The histogram $R_I(\tau_1)$ obtained from 42 molecules is plotted in Fig.5.7b. It is evident that the lower the initial emission intensity is, the longer it takes until the first event. It suggests that these processes are light driven.

5.2.8. A single molecule showing two types of spectral characteristics.

If the spectrum of the emission remains constant, there is a well defined and monotonic relation between the total signal and the spectral peak position. In the two channel measurement, the total signal is the sum of two channels, $\boldsymbol{S}$, and the spectral peak position, λ_{peak}, is related to the ratio between two channels, ρ. For example, we show the $\boldsymbol{S}(\rho)$ plots for a molecule in Fig.5.8a for the first 1.6s, Fig.5.8b for the next 2.4s and Fig.5.8c for the remainder of the measurement. The raw data is shown in Fig.5.8d for $\boldsymbol{S}$ and in Fig.5.8e for ρ. Initially, $\boldsymbol{S}(\rho)$ has a small slope. The total signal changes only slightly when the ratio changes by a factor of four. Spectral changes of the type shown in Fig.5.2, where the relative weight of the contributions from two peaks change while maintaining the total signal, can explain this behavior. After 1.6s, $\boldsymbol{S}(\rho)$ shows a completely different and much steeper slope. Change in the ratio also involves large change in the total signal. Spectral changes of the type shown in Fig.5.1, where λ_{peak} changes, could result in this behavior. Rotational jump could also explain for this change of behavior, because, depending on the dipole orientation, the same amount of spectral jump could show up differently on the ratio. However, this alternative explanation is unlikely because the range of the ratio did not change much. The main difference between Fig.5.8b and Fig.5.8c is the island with $\boldsymbol{S} \sim 0.2$ that shows up only on Fig.5.8b. This island is due to the recurring trips to a state with low emission intensity and red shifted

emission (small ρ), that can be better seen in the zoom-in Fig.5.8f. This state has a similarity to the dark state in that the molecule revisits the state repeatedly, but is fluorescent.

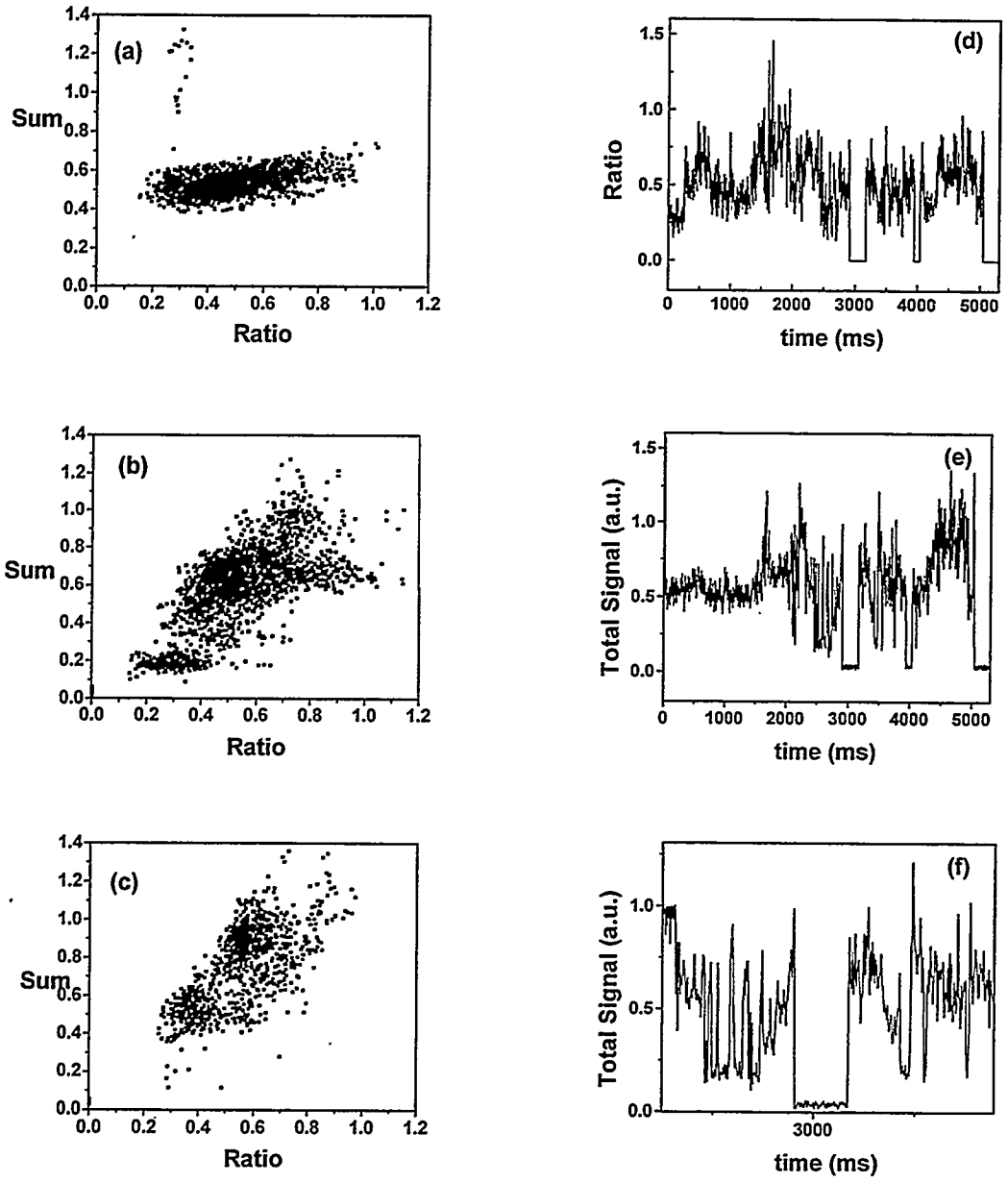

Fig.5.8. Relation between the total signal and the ratio between two channels. Total signal (e) from a single TR-DNA and the ratio (d) are plotted as a function of time (1ms integration time). Data can be visualized in another way by plotting the sum vs. the ratio for each data point. (a) is for the first 1.6 s, (b) is for the next 2.4 s and (c) is for the rest of the data. An island of points in (b) with sum ~ 0.2 is due to the frequent jumps to the state shown in (f).

5.3. Quantum Jumps

5.3.1 Introduction

In 1913, Bohr suggested that the light-matter interaction happens in such a way that an atom undergoes instantaneous transitions of its internal electronic states upon the emission or absorption of a photon, or "quantum jumps". At that time, it was considered to be an artifact of Bohr's theory of atom. And furthermore, such jumps could not be measured on large ensemble of atoms. With the advent of optical cooling and radio frequency traps, it became possible to capture a single ion and observe it. Quantum jumps were observed for single ions in radio-frequency traps by several groups (Bergquist et al. 1986; Nagourney et al. 1986; Sauter et al. 1986b). More recently, quantum jumps have been observed on a more complex system, single terrylene molecules in a solid matrix at liquid helium temperature (Basche et al. 1995). In these experiments, the fluorescence of a strongly allowed electronic transition was shown to cease abruptly due to quantum jumps into a metastable state. These jumps are the direct manifestation of quantum mechanics and their observation is fascinating because it allows one to watch the collapse of the wave function. Previous studies were done at very low temperatures (< 25mK for ions and < 4K for molecules), and a question arises: is low temperature necessary for the observation of quantum jumps?

Fluorescence dye molecules exhibit intersystem crossing (ISC) to the triplet state (T_1) (see Fig.5.9.). While cycling through the singlet transition (S_0<==>S_1), photons are emitted until intersystem crossing occurs.

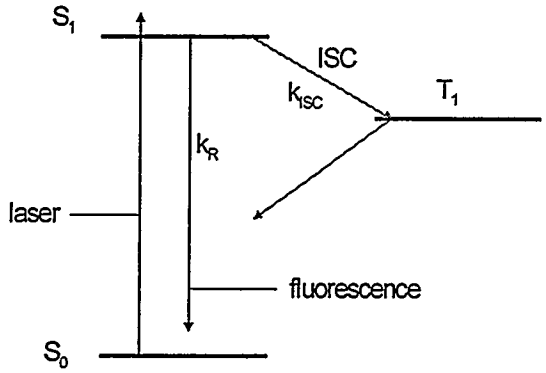

Fig.5.9. Energy level diagram for typical fluorescent molecules. Main transitions happen between singlet ground state (S_0) and singlet excited state (S_1). Spin forbidden transition to the triplet state (T_1) or intersystem crossing (ISC) happens with a low probability. The molecule returns to the singlet ground state via intersystem crossing or phosphorescence.

Because the ISC yield Y_{ISC} ~ 0.1%, on average a few hundred photons are emitted before a dark period of duration τ_{off}. The effect causes "bunching" of the emitted photons, a different way of looking at quantum jumps. Direct real time observation of bunching or quantum jump has been very difficult for single molecules because in general τ_{off} is short (~μs) and because the detection efficiency of the emitted photons is very low (<1%). Indirect evidence of bunching could be obtained by measuring the autocorrelation function of the fluorescence emission. The intensity dependent measurements of the autocorrelation function of a single molecule would yield τ_{off} and Y_{ISC}. First direct observation of quantum jumps in polyatomic molecules was performed on terrylene ($C_{30}H_{16}$) in p-terphenyl that has favorable τ_{off} = 0.5ms and $Y_{ISC} < 10^{-6}$. In such a system, a few thousand photons can be detected to be bunched together, with easily detectable dark periods of 0.5ms. Although the short dark-state lifetime in solution prevented direct measurement of these states, recent studies using far-field excitation of individual molecules (in solution) at room temperature have indirectly inferred ICS via correlation analysis (Widengren et al. 1994) or via saturation effects leading to reduced emission intensity (Nie et al. 1994, Schmidt, 1995 #682) It is known that fluorescence dye molecules have the triplet state lifetime τ_{off} as long as a few milliseconds in deoxygenated environments or on a dry surface at room temperature. This, combined with the optimized detection efficiency of fluorescence photons (>10%), ISC in a single fluorescence dye molecule is a good candidate for a model system in which the quantum jumps can be directly seen in ambient conditions.

In this work, we used far-field excitation to probe the single molecule quantum jumps at room temperature. Far-field excitation makes it possible to space the detected fluorescent photons closer to each other than the triplet state lifetime, therefore we find: (i) Quantum jumps can be directly observed at room temperature; (ii) Strong inhomogeneity in τ_{off} and Y_{ISC}, in contrast to low-temperature work on molecules in a crystal where ICS parameters are similar for all molecules (Basche et al. 1995; Vogel et al. 1995).The inhomogeneity in these parameters is likely due to different local surroundings; (iii) Individual molecules often exhibit abrupt changes in τ_{off} and Y_{ISC} that are correlated with spectral change.

5.3.2 Individually resolved quantum jumps to triplet state

The time evolution of fluorescence emission of single Texas Red (TR) fluorophores linked to individual DNA strands (TR-DNA) was studied using far-field laser scanning confocal microscopy. Single molecules were adsorbed on silanized glass surface with areal concentration of 0.5 molecules/μm^2 such that the average distance between molecules was greater than the diffraction limited laser excitation spot. The molecular emission was collected with a 1.4 NA objective and imaged on two silicon avalanche photodiodes. A dichroic mirror with a cutoff frequency at the peak of the ensemble emission spectrum (600 nm) was used to split the emission into the two detectors. The count rates of both detectors were simultaneously recorded as a function of time with 200 μs integration time. Due to the limitation of hardware, shorter integration was not possible. The excitation beam was circularly polarized and had a power of 9 μW at the sample plane. Each data trace is obtained after locating a molecule using the automated search with lower excitation intensity.

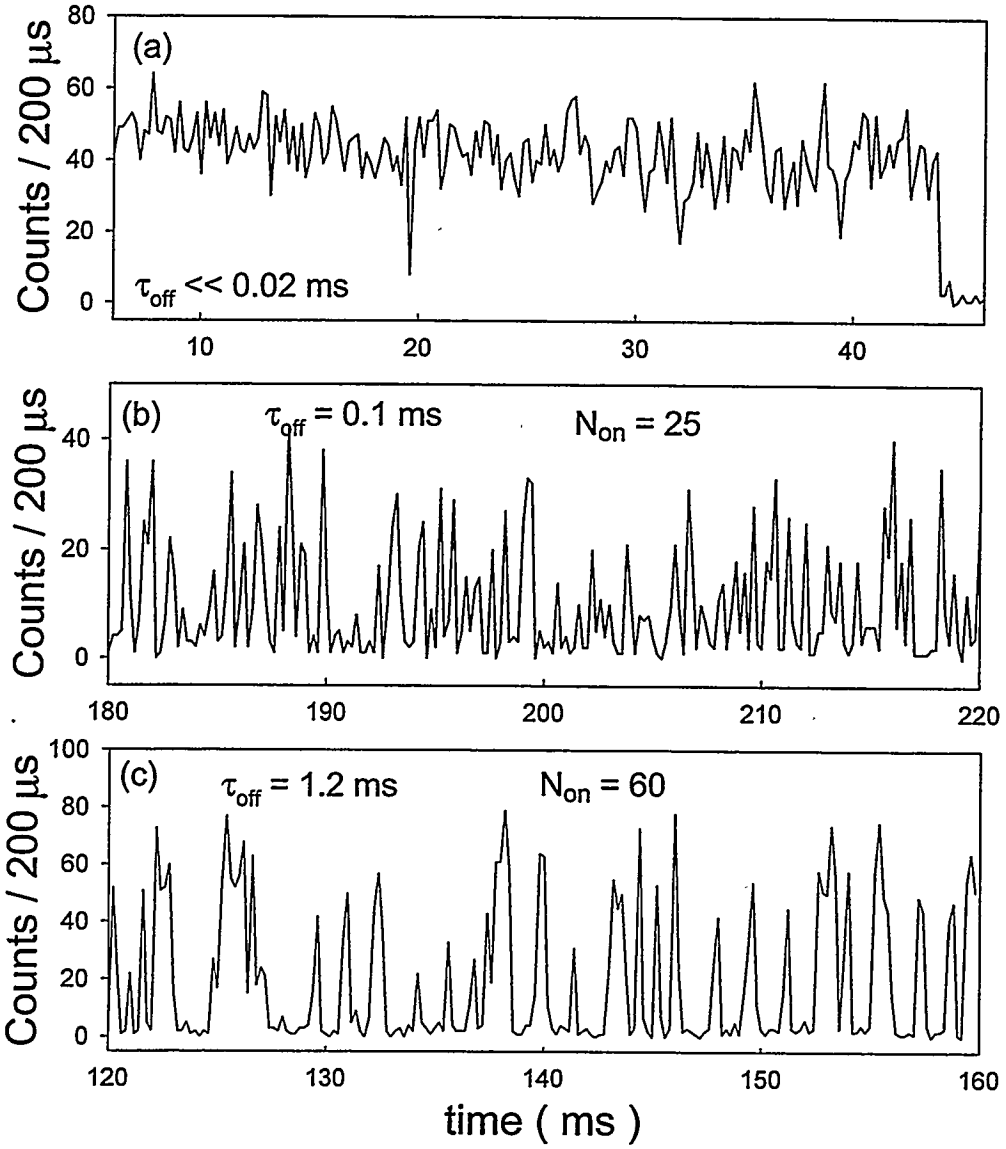

Fig.5.10. Time traces of three TR-DNA moleculés measured with the far-field excitation. (a) Relatively quiet emission meaning triplet state lifetime much shorter than 0.02ms. Telegraph noise, arising from on-off transitions is evident in (b) and (c). τ_{off} and N_{on} are estimated by building histograms of on-state counts and off-state duration..

Fig.5.10 shows three time-traces of the molecular emission intensities (sum of two channels) from three individual TR-DNA molecules. While the emission of molecule a is relatively quiet , the emission time traces of molecule b and molecule c show larger fluctuations. Qualitatively, these fluctuations have the characteristic of "telegraph" on/off

noise, i.e. arising from two states, one fluorescent, the other dark. Due to the finite time resolution of the measurement, some data points reside between the two states.

In order to test the assumption of telegraph noise, and to quantitatively analyze the data, we modeled the molecular emission as arising from two states: an "on" state with τ_{on} and an "off" state with τ_{off} duration. Since the "on" state in most observed molecules did not last longer than the integration time, a parameter more meaningful than τ_{on} is the total number of counted photons during the "on" state.

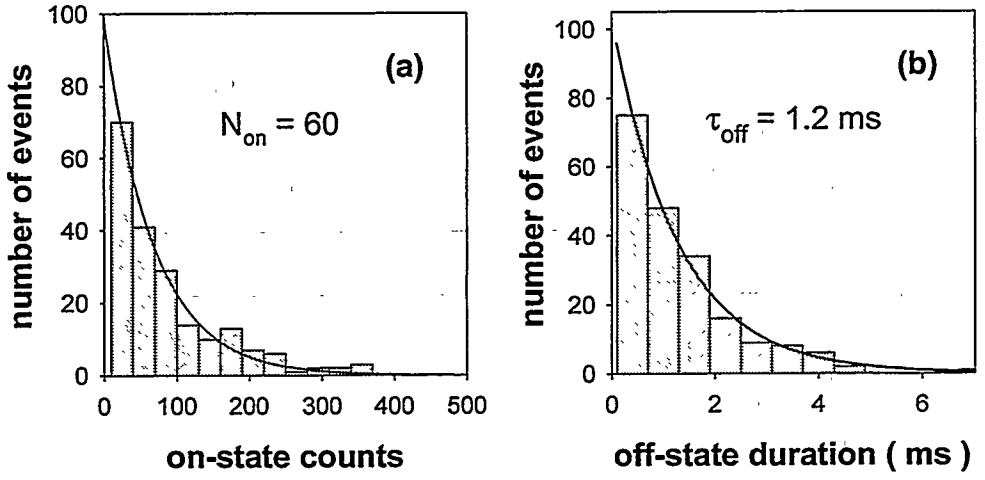

Fig.5.11. Histograms of on-state counts (a) and off-state duration (b) for the data shown in Fig.5.14c. Curve-fits to exponential decay are shown as well. From the curve-fits, the on-state average counts (N_{on}) and the off-state lifetime (τ_{off}) are extracted.

The data was analyzed in the following way: for each event (transition from "on" state to "off" state), we measured the number of counts in the "on" state, and the duration of the "off" state and two histograms (distribution of "on" counts and "off" duration) were constructed for each molecule. As an example, the histograms for molecule c in Fig.5.10 are shown in Fig.5.11. Each histogram can be fit very well with a single exponential. This analysis yields for that molecule, τ_{off} of 1.2 millisecond and an "on" state average counts

N_{on} of 60 ±10. The quality of the fits are evidence for the underlying Poisson statistics governing the random transitions between the two states.

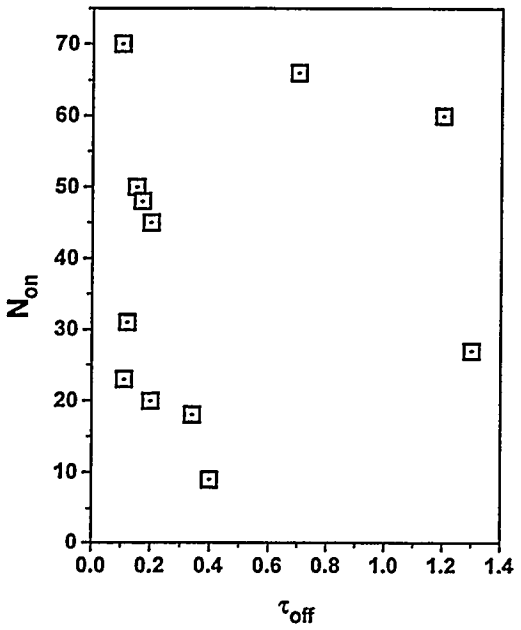

Fig.5.12. Relation between t_{off} and N_{on}. For each molecule with measurable t_{off} and N_{on}, a square is plotted. No simple relation between them could be found.

This analysis and fits could be performed only when τ_{off} was long enough compared to the integration time, allowing us to resolve individual jumps. When τ_{off} was too short to be resolved, a rough estimate for its value was obtained from a simple simulation that was describe for the near-field measurement. For example, from such simulations it was possible to deduce that the molecule c in Fig.5.10 had τ_{off} shorter than 0.02 millisecond. Out of 40 molecules examined, 20 molecules displayed fully resolvable jumps with τ_{off} longer than 0.1 millisecond. The large distribution in dark-state lifetime is likely due to different surface-fluorophore, and DNA-fluorophore interactions as well as different local environment. No systematic relation, however, between τ_{off} and N_{on} was found (Fig.5.12). While τ_{off} spans almost two orders of magnitude (from below 0.02 ms to 1.3 ms), the values for N_{on} have smaller scatter (50 ±20 counts). The transition efficiency, Y_{ISC}, defined as the inverse of the average number of emitted photons during the "on" state (N_{on} divided by the total detection efficiency of 10%) was estimated to be about 0.2%.

These dark-state transition efficiencies and lifetimes are consistent with the dark state being a triplet state. The transition efficiencies are in good agreement with the estimated intersystem crossing efficiencies of less than 1% for rhodamines (Johnson and Garland 1982; Kasche and Lindqvist 1964). The dark-state lifetimes are also consistent with a

triplet state that is not accessible to oxygen. Triplet-state lifetimes of 1-5 milliseconds, for example, were reported for rhodamine in deoxygenated solution (Kasche and Lindqvist 1964). While oxygen is a highly efficient quencher of triplet states in solution (Asimov et al. 1990), the efficiency may decrease at a solid-air interface, as present here. Indeed, dramatic increases in triplet-state lifetimes under dry conditions compared to that in solution have been found for molecules adsorbed on air-solid interfaces (Scalettar et al. 1990). Since triplet state lifetimes are highly sensitive to oxygen concentration and accessibility, the observed distribution in τ_{off} could be affected by local variations in this factor.

Because of the extended triplet-state lifetime in the dry-state, the emission is expected to saturate at intensities lower than in solution. This is demonstrated in Fig.5.13. The emission rate from a single molecule was recorded while the excitation intensity was repeatedly modulated from I_0 to 20 I_0 (I_0 = 2.5 kW/cm^2). The data from 13 modulation periods was averaged (filled circles) and fitted (solid line) to $R = a \cdot I / (1 + I / I_S)$ where I is the excitation intensity, I_S is the saturation intensity and R is the emission rate. We find that the saturation emission rate R_S, defined as $R(I = I_s)$ is 6.5 MHz. The measurements were repeated on several single molecules yielding 2MHz $\leq R_S \leq$ 20MHz (Fig.5.13c). Since $\tau_{off} = [Y_{ISC} \cdot R_S]^{-1}$, a second estimate for its value can be obtained from the saturation data (and the measured Y_{ISC}) and compared to the time resolved data of Fig.5.10. Y_{ISC} was found to be 0.2% on average with a relatively small scatter and therefore is assumed to be more-or-less constant. With this assumption, τ_{off} is found to range from 0.3 ms to below 0.03 ms. These numbers correspond well to the numbers directly extracted from the time resolved emission data and prove that τ_{off} is longer than in aerated solution. Note that the saturation behavior demonstrates that the above dark state is an excited-state product, i.e. its population is a function of excitation intensity. This rules out the dark-state being a ground-state phenomenon, such as a non-fluorescing twisted-state (Vamosi et al. 1996).

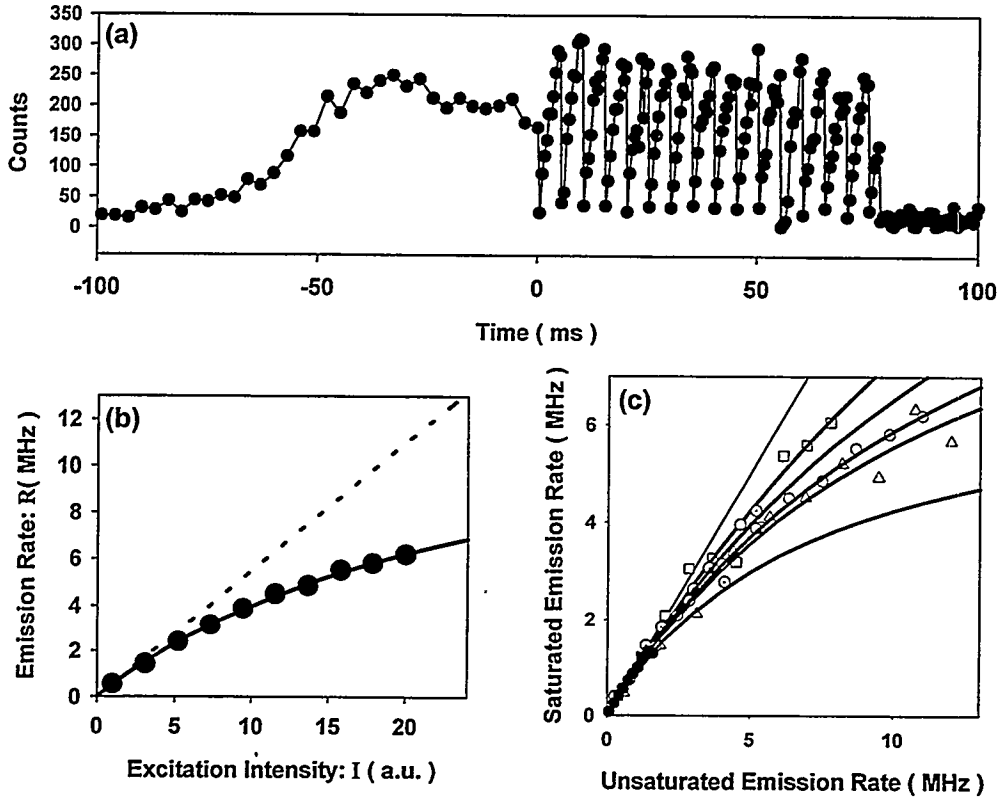

Fig.5.13. Saturation of single molecule emission due to triplet state. (a) After an automated search, intensity modulation up to 20 fold is performed until the photodestruction. (b) Intensity dependent emission rate showing clear saturation (filled circles). The data is obtained by averaging the first 13 modulation periods in (a). The data is fit to the saturation equation discussed in the text. From the curve-fit, a saturation emission rate of 6.5 Mhz is extracted. Detector response and detection efficiency are corrected for. The straight line is the emission level expected without saturation due to the triplet state. (c) The result of saturation measurements on six molecules are shown with the saturation curves. The excitation intensity is normalized to the emission rate expected without saturation.

In addition to quantum jumps to triplet states, we often observed dark states with longer duration, ranging from milliseconds to seconds. They are distinguished from triplet state by very low transition efficiencies ($<10^{-5}$). Although the origin of this dark-state is not known, it is possible that it is due to a twisted conformation, some of which are known to be non-fluorescent (Vamosi et al. 1996). The recovery of the molecular emission from these long dark states was often accompanied by spectral changes in the

fluorescence emission, as determined by a sudden jump in the ratio between the two channels (Ha et al. 1996d).

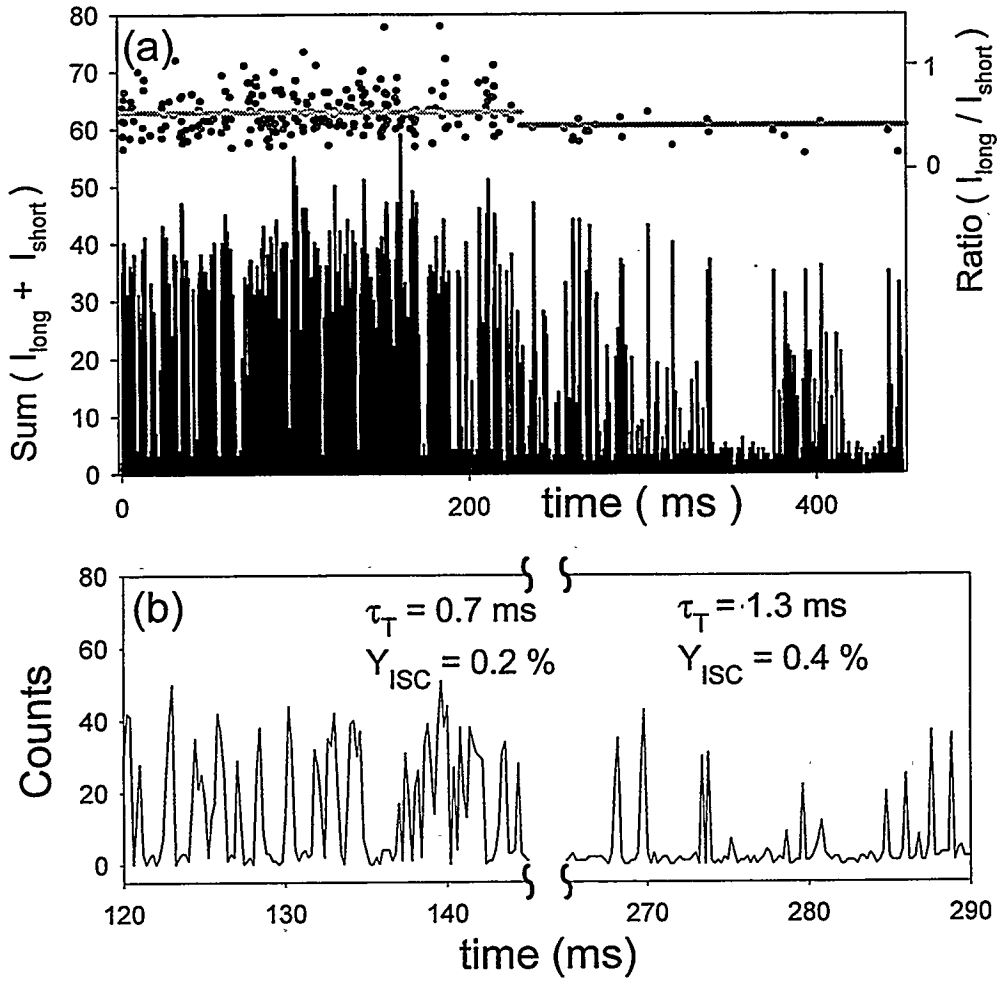

Fig.5.14. (a) Time traces of single molecule total emission (bottom curve) and the ratio between two channels (top curve). The bottom curve shows long dark states with duration up to 400 milliseconds. The ratio signal decreased abruptly at 230 millisecond, indicating a spectral jump towards blue (the ratio is plotted only for points with total counts above 30). Gray guide lines denote the average of the ratio before and after the spectral jump. (b) Zoom in figure showing individual quantum jumps before and after the spectral jump. Triplet state lifetime and intersystem crossing rate are noted in the figure.

The data shown in Fig.5.10 demonstrates not only spectral changes, but also correlated changes in ISC parameters. By piece-wise analyzing that data as we did for Fig.5.10 and Fig.5.11, we found that τ_{off} increased from 0.7 millisecond to 1.3

millisecond and Y_{ISC} increased from 0.2% to 0.4% after a spectral jump towards blue (at 230 millisecond). Out of 40 molecules, 4 molecules displayed similar behavior where spectral and ISC parameters underwent correlated and sudden changes. In all four cases, blue shifts resulted in an increase in Y_{ISC}. Changes in τ_{off} , however, did not show a simple dependence on the spectral changes.

The relatively small spread of Y_{ISC} among molecules is likely not coincidental. If the excited singlet state has nanosecond lifetime, then the intersystem crossing rate (k_{ISC}) is on the order of 1/1μs. This rate, dominated by the structure of the dye, is shorter than $1/\tau_{off}$, and hence less susceptible to diffusional interactions and therefore less environmentally sensitive than the triplet lifetime.

The ability to see quantum jumps of single molecules at room temperature opens up the possibility of detecting quantum jumps of 2 (or a small number of) molecules placed in close proximity ($<<\lambda$). Cooperative effects, including correlated dark-state transitions and superradiance of such systems have been predicted theoretically and found experimentally for Ba^+ ions at very low temperature (Lewenstein and Javanainen 1987; Sauter et al. 1986a). The ability to place fluorescent molecules at well-defined, closely spaced intervals, is now routine and the experimental apparatus and analysis scheme outlined here is directly applicable to measuring such quantum effects in multi-body systems.

5.4. Rotational jumps : Observation of single desorption and re-adsorption event

5.4.1. Introduction

In this work, we used the polarization modulation technique to study dipole rotation of fluorophores linked to a short single strand DNA (ssDNA) molecule which was

attached to a silanized glass surface. We interpret the rotational jump as the result of desorption and re-adsorption of the fluorophore from and onto the surface accompanied by a transition period during which the fluorophore undergoes virtually free rotation.

5.4.2. Rotational jumps

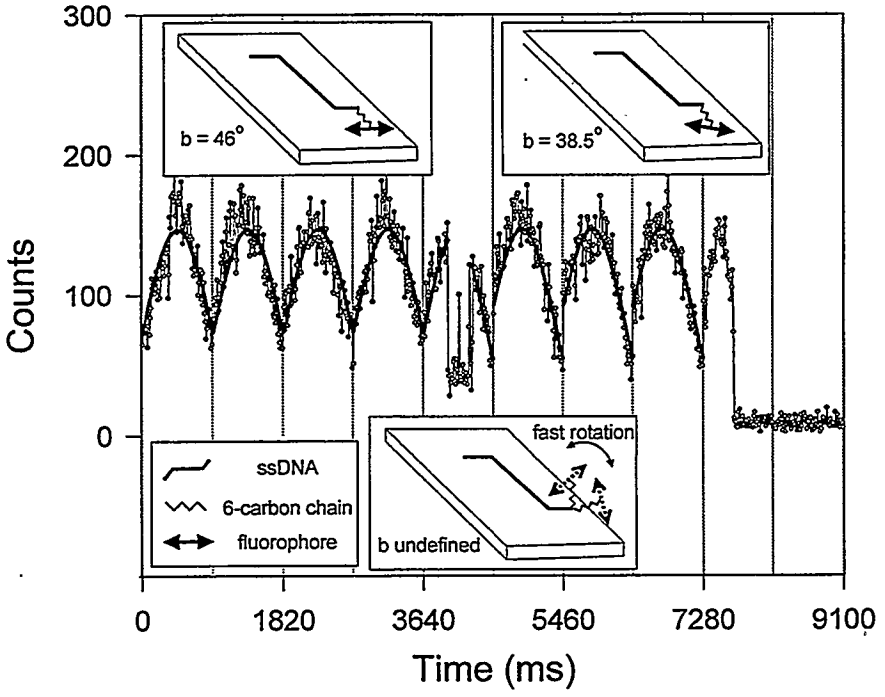

Fig.5.15. A 7.5° in-plane rotational jump of a TR molecule. Solid line is the fit to the data before and after the interruption. Vertical lines separate each modulation period from 0 to 90 degree. Insets show a model for the rotational jump.

We excite single molecules in the far-field with linearly-polarized light whose polarization angle is continuously modulated, on a ms time scale. The fluorescence of the molecules is measured as a function of time. A 515nm laser beam was introduced through the epi-illumination path of a fluorescence microscope and the polarization was modulated with an electro-optic modulator. The resulting linear polarization (modulated in time) at the sample plane was better than 100 to 1. The measurements were made on

over 200 individual TR molecules. Most (over 97 %) of the molecules showed stationary dipoles (see previous sections). Out of more than 200 molecules examined, 5 molecules displayed rotational jumps that changed the dipole orientation. Fig.5.15 shows an emission time trace of a TR-DNA molecule, measured with a single detector. For the first 4 polarization scans, the dipole orientation is static. In the fifth scan, there is an interruption in the molecular emission. After the interruption, the emission signal resumes its initial value, but the phase changed. It was found that after the interruption, the molecule changed its in-plane orientation by $7.5° \pm 0.4°$. Because the peak intensity remained the same, we deduce that the out-of-plane dipole component did not change. Similar to Fig.5.15, all observed rotational jumps followed a transition period in the molecular emission (0.1 s to 1.3 s long) that showed up as an interruption in the well behaved series of sinusoidal curves.

The data shown in Fig.5.16 was acquired with the two-color detection scheme, as in Fig.5.5. The sum of the counts on the short and long wavelength channels, from another TR-DNA molecule is shown (solid line, bottom curve). The molecular emission exhibits a sinusoidal signal in time, which is interrupted three times. The three transition periods (labeled "1", "2" and "3" in the figure), are characterized by noisy and unmodulated molecular emission. In these periods, the molecule has no stationary dipole. The signal in the stationary periods was fit and the dipole angle was deduced (noted in the figure). A change in dipole orientation followed each interruption in the emission. Also shown in Fig.5.16 is the ratio between the two channels counts (filled circles, top curve). For the stationary dipole periods, the ratio is fixed and featureless.

A likely explanation for the nature of the transition periods in Fig.5.15 and Fig.5.16 is desorption of the fluorophore from and re-adsorption to the surface (see insets in Fig.5.15). The treatment of the glass surface ensures the binding of the DNA. The fluorophore, linked to the DNA through a flexible 6-carbon chain, is most likely bound flat to the surface (near-field imaging of identically prepared samples revealed no z-

component of the dipole). However, if the fluorophore is only loosely bound to the surface, it can desorb from the surface and rapidly rotate along the linker, before it is re-adsorbed at another site with different orientation. The desorption process might be thermally activated, if the binding energy to the surface is comparable to k_BT, or may be the result of a light induced process (such as conformational change of the molecule). The mechanism for desorption will be the subject of future investigations.

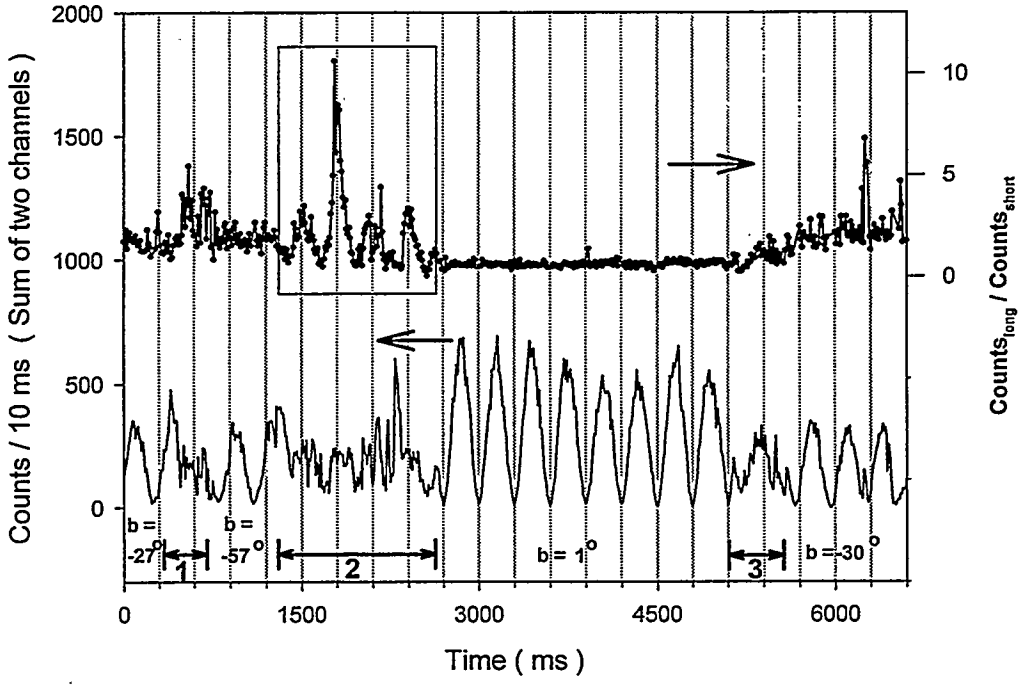

Fig. 5.16. The ratio and sum of two channel counts from a single TR-DNA that shows multiple rotational jumps. The transition periods of three rotational jumps are marked with 1,2,3. Modulation was done from -81° to 81° where 0° is when the excitation was s-polarized with respect to the dichroic beam splitter.

When the fluorophore is free to rotate rapidly and sample many solid angles, the emission intensity is reduced, as clearly shown in Fig.5.15.

For completely free, unrestricted rotation, the signal level is expected to be 1/3 of the peak signal obtained when the dipole moment is aligned with the excitation polarization (average of $cos^2\theta$ over 4π sterradian is 1/3 where θ is the angle between the instantaneous

molecular dipole moment and the excitation electric field vector) In Fig.5.15, the signal level during the transition period is about 30% of the maximum, supporting the free rotation model.

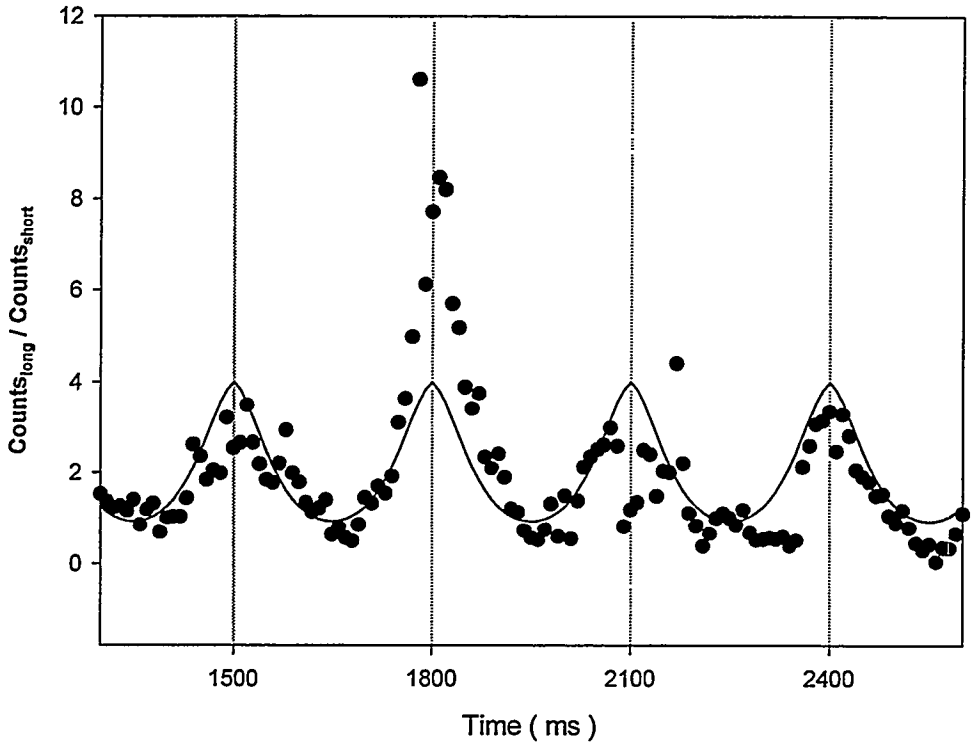

Fig. 5. 17. Zoom-in to the boxed area in Fig.5.16. Solid line is the fit under the assumption that the molecule rotates freely during the transition period.

Another, very strong support for this model is obtained from the modulated ratio signal during the transition periods in Fig.5.16. During transition period "2" (zoom-in is shown in Fig.5.17.), the ratio displays a clear modulation with the same period as of the excitation polarization. Barring the unlikely possibility of spectral jumps exactly in phase with the excitation polarization, this data gives evidence for rapid and free rotation of the fluorophore during the transition period. Free rotation on a time scale faster than the integration time (10 ms) but slower than radiative lifetime (~ ns) will result in partially polarized emission along the excitation polarization. Because of the polarization

dependence of the dichroic mirror, the ratio signal between the two channels will follow the excitation polarization, and hence will be modulated with the same modulation period. Using the same model as in Fig.5.4, and assuming full random rotation over all angles, the data in Fig.5.17 was fit with a single fitting parameter - the spectral peak position - that was determined to be 600 nm. Deviations from the fit are probably due to spectral jumps or hindered motions resulting from brief visits to loosely bound sites within the transition period.

6. DUAL MOLECULE SPECTROSCOPY

6.1. Introduction

The spectroscopic signature of fluorescence from two molecules carries with it a wealth of information about the distance, orientation and relative dynamics between the two sites at which the two molecules reside. Thus, differential measurements between two sites of a macromolecule can be performed. Adopting the notion that *two are better than one*, we have developed two techniques which are based not on *single* molecule but on the detection and spectroscopy of *two close-by* molecules.

Both techniques rely on labeling the two points of interest (on a *single* macromolecule, or between *two* interacting molecules) with two different dye molecules, which fluoresce at two different colors (dual-color labeling).

In the first, which we call single-pair fluorescence resonance energy transfer (spFRET), one point is labeled with a donor fluorescent fluorophore, and the second point is labeled with an acceptor fluorophore. The dyes are chosen such that the acceptor's absorption overlaps, or is in resonance with, the donor emission. Due to the dipole-dipole interaction, energy is transferred from the donor to the acceptor. The distance between the two points is determined by measuring the extent of transferred energy. More importantly, changes in distance between the two points, due to conformation changes, may be detected by monitoring the changes in the amount of transferred energy as function of time.

In the second scheme, the absorption and emission spectra of the two dyes do not overlap, and energy transfer is not present. We call this non-resonant dual-color imaging (NRDCI). Images of each fluorophore are simultaneously, but separately acquired, by exciting the two molecules with two different excitation beams which share the same

volume of excitation, and separating the emission of the two dyes. Each fluorophore produces an image with a width determined by the point-spread function (PSF) of the microscope (diffraction limit in conventional microscopy, aperture diameter in NSOM). The position of each dye, and more importantly, the distance between the two fluorophores, is determined with accuracy which is much better than the PSF extent itself.

6.2. Single pair Fluorescence Resonance Energy Transfer (spFRET)

6.2.1. Conventional ensemble Fluorescence Resonance Energy Transfer

Fluorescence Resonance Energy Transfer (FRET) (Forster 1948) has proven to be a useful spectroscopic technique for measuring distances in the 10-75 Å range. The technique is valuable because measurements can be made under physiological (or other) conditions with near- Å resolution, over biologically-relevant distances, and with the exquisite sensitivity of fluorescence measurements. For these reasons FRET has found wide use in structural biology, biochemistry and polymer science.

The idea behind the technique is to label the two points of interest with different dyes, one, which is fluorescent and is called the donor, and the other, which must have an appropriate absorption, is called the acceptor. The acceptor is chosen such that its absorption overlaps significantly with the donor emission and is often fluorescent as well, though not necessarily so (Fig.6.1). By choosing dyes with the appropriate spectral characteristics, after the donor is excited by light, it can transfer energy to the acceptor via induce dipole-induced-dipole interaction. The efficiency of energy transfer depends on the inverse sixth power of the distance between the dyes. The acceptor must be within 10-75Å to get reasonable energy transfer. The exact range depends on the dyes chosen.

The Hamiltonian , or energy of interaction between the donor and acceptor is:

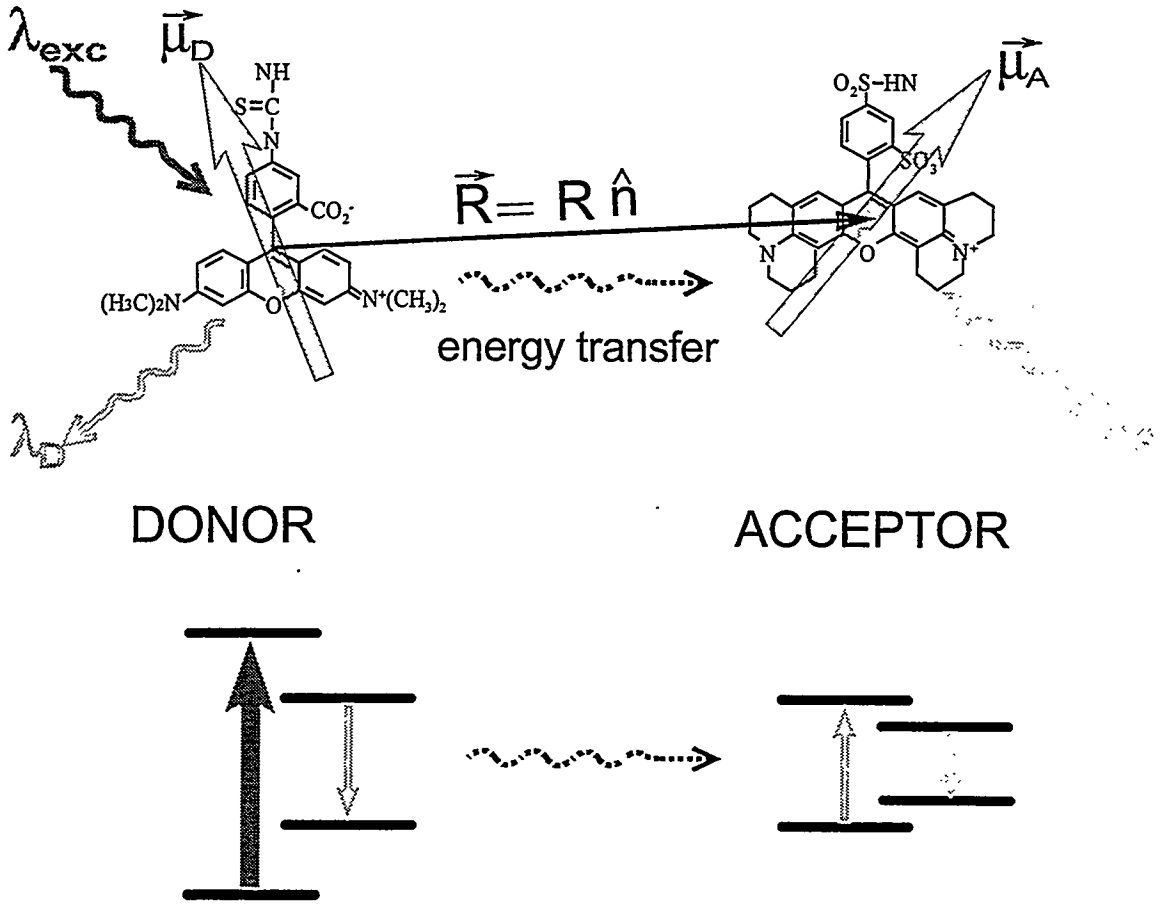

Fig.6.1. Fluorescence resonance energy transfer (FRET) between a donor molecule and an acceptor molecule, via dipole-dipole interaction. The two shaded arrows denote the molecular dipole moments. Energy transfer efficiency strongly depends on the three vectors ($\vec{\mu}_D$, $\vec{\mu}_A$ and $\vec{R}$). The resonance between the donor emission and the acceptor absorption (bottom of the figure) is required for efficient energy transfer.

$$H = \vec{\mu}_D \cdot \vec{\mu}_A / R^3 - 3(\vec{\mu}_D \cdot \vec{R})(\vec{\mu}_A \cdot \vec{R})/R^5 \qquad (6.1)$$

$\vec{\mu}_D$ ($\vec{\mu}_A$) is the transition dipole moment of the donor (acceptor) and $\vec{R}$ is the vector separating their centers. According to Fermi's Golden Rule, the rate of transition is proportional to the square of the Hamiltonian matrix element between final and initial states.

$$k_t \propto \left| \langle D^*, A | \vec{\mu}_D \cdot \vec{\mu}_A / R^3 - 3(\vec{\mu}_D \cdot \vec{R})(\vec{\mu}_A \cdot \vec{R})/R^5 | D, A^* \rangle \right|^2 \qquad (6.2)$$

where the initial state is the product of the excited state of the donor (<D*|) and the ground state of the acceptor (<A|) and the final state is the product of the donor ground state (|D>) and acceptor excited state (|A*>). Therefore, the rate of energy transfer

depends on the inverse-sixth power of the distance between the donor and acceptor and on their relative oscillator strengths.

The rate of decay of the donor excited state is just the sum of all decay rate pathways, $k_r + k_{nr} + k_t$, where k_r is the radiative decay rate, k_t is the decay rate due to energy transfer to the acceptor and k_{nr} is the sum of all other non-radiative decay rates such as dissipation. The fraction of the donor excitation going to the acceptor (*E*, also called the efficiency of energy transfer) is therefore:

$$E = k_t/(k_t+k_r+k_{nr}) = 1/[1+(k_r+k_{nr})/k_t] \tag{6.3}$$

and combined with equation (6.2),

$$E = \frac{1}{1+\left(\frac{R}{R_0}\right)^6} \tag{6.4}$$

where *R* is the distance between the donor and acceptor and R_o is the distance at which 50% of the energy is transferred and is a function of the properties of the dyes:

$$R_o = \left(8.79\cdot 10^{-5} n^{-4}\cdot \phi_D \cdot J \cdot \kappa^2\right)^{1/6} [\text{Å}] \tag{6.5}$$

with *n* the index of refraction of the medium, ϕ_D the donor quantum yield, *J* the spectral overlap of donor emission and acceptor absorption $[nm^4M^{-1}cm^{-1}]$, and κ^2 the relative orientation of the two dipoles (Fig.6.1):

$$\kappa^2 = \left(\cos\theta_{DA} - 3\cos\theta_{DR}\cos\theta_{AR}\right)^2 \tag{6.6}$$

where θ_{DA} is the angle between donor dipole moment $\vec{\mu}_D$ and acceptor dipole moment $\vec{\mu}_A$, θ_{DR} is the angle between $\vec{\mu}_D$ and $\vec{R}$, and θ_{AR} is the angle between $\vec{\mu}_A$ and $\vec{R}$. With no *a-priori* knowledge of these angles, $0 < \kappa^2 < 4$.

The importance of the above equations is that *energy transfer can be used as a spectroscopic ruler*, as first convincingly shown by Stryer and Haugland (Stryer and Haugland 1967) i.e. one can determine distances by measuring the extent of energy transfer, assuming that R_0 is known.

Energy transfer can be measured in a number of ways: by a decrease in donor fluorescence intensity (because some of the energy is going to the acceptor, instead of into fluorescent photons), by a decrease in donor excited state lifetime (because energy transfer to the acceptor is an additional relaxation pathway of the donor excited state) or by an increase in acceptor fluorescence (Fig.6.2). Measured via donor properties, the efficiency of energy transfer is then:

$$E = (1 - I_{D_A}/I_D) = 1 - \tau_{D_A}/\tau_D \qquad (6.7)$$

where I_{D_A}, τ_{D_A} are the donor's intensity and excited state lifetime in the presence of acceptor, and I_D, and τ_D are the same parameters in the absence of acceptor. The extent of energy transfer can also be determined by measuring the increase in fluorescence of the acceptor due to energy transfer and comparing this to the residual donor emission:

$$E = [I_{A_D}/\phi_A]/[I_{D_A}/\phi_D + I_{A_D}/\phi_A] \qquad (6.8)$$

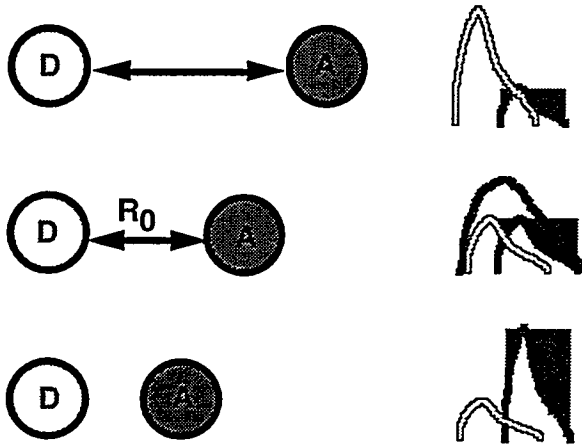

Fig.6.2. Distance dependent energy transfer. When donor (D) and acceptor (A) are far away from each other, donor emission (unshaded on the right) dominates. When they are closer than R_0, the acceptor emission (shaded) dominates.

where I_{D_A} is the integrated area under the donor emission curve in the presence of acceptor, I_{A_D} is the integrated area of the sensitized emission of the acceptor (i.e., not including the fluorescence due to direct excitation of the acceptor) and ϕ_D, ϕ_A are the quantum yield for donor or acceptor. The integrated areas are determined by curve fitting the spectrum to the sum of a donor-only and acceptor-only spectra.

When measuring the sensitized emission of the acceptor and using equation (6.8), one must subtract out the component of acceptor fluorescence due to direct excitation and also subtract out donor emission which overlaps in wavelength with acceptor emission.

This can be done by comparing multiple samples, labeled with donor-only, acceptor-only and donor-acceptor.

Once E is measured, n, ϕ_D and J are measured for their solution value. It is often assumed that the dipole moments of donor and acceptor are free to rotate in all direction, on a time scale much faster than their radiative lifetime. In this case, a geometrical averaging of the three angles results $\kappa^2 = 2/3$ (in many cases, however, the fluorophores interact with the macromolecule that they are attached to, thus restricting their motion and introducing uncertainty in the value of κ^2). Distance is then extracted by inverting equation (6.4).

6.2.2. Single pair FRET : motivation & considerations

The rationale for wedding FRET with near-field SMD was to explore the potential advantages of SMD together with the NSOM capability to determine dipole moment orientation in three dimension. The advantages for static distance measurements are: (1) Unlike in conventional (ensemble) FRET where great care must be taken to purify the complex labeled with both donor and acceptor, single pair FRET (spFRET) eliminates this problem because one complex is measured at a time, and the donor-acceptor labeled complex can be easily distinguished from single species by their characteristic spectral properties. (2) Since sample swapping which can induce fluctuations in concentrations is replaced by photodestruction (see below), higher sensitivity is expected.

On the other hand, spFRET has disadvantages with respect to static distance measurements. Here, we list several causes that can make the accurate distance determination difficult.

Such measurements will most probably be done on immobilized molecules, requiring an accurate measurement of κ^2 , since angular averaging is not possible. In principle, the

two vectors, $\vec{\mu}_D$ and $\vec{\mu}_A$, can be determined by near-field imaging with various excitation polarizations (Betzig and Chichester 1993), or by polarization modulation study (Ha et al. 1996c). However, the radius vector $\vec{R}$ cannot be determined and only one angle, θ_{DA}, will be accessible. Following simulations reveal that the knowledge of this angle restricts the range of κ^2 only very slightly compared to the case where all angles are not known.

For a given angle between two dipoles, one can calculate the range of κ^2 for all the possible angles of the radius vector. In fact, more useful number is $\kappa^{1/3}$ because the final distance determined will be proportional to $\kappa^{1/3}$, and this way we can rephrase the question to how much the knowledge of one angle restrict the range of distance error compared to the case where none of the angles are known.

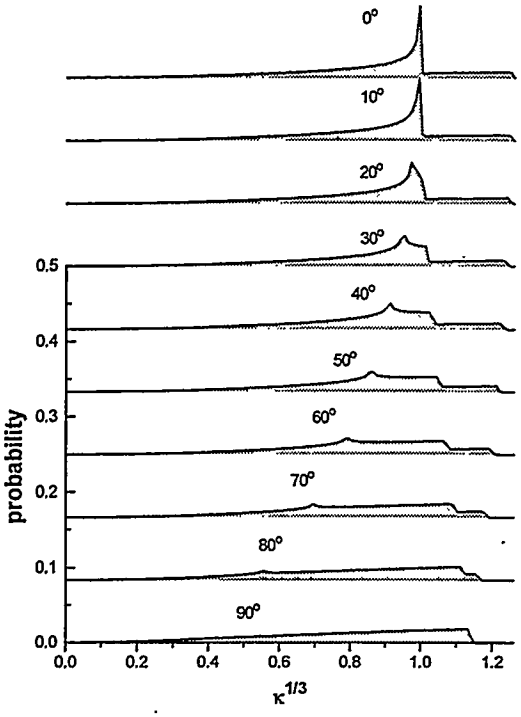

Fig.6.3. Probability distribution of $\kappa^{1/3}$ when the angle between two dipoles is known (0° to 90°) and no other information is available.

A simple calculation was performed to answer this question. The unit radius vector **r** connecting to dipoles can be represented with two angles ϕ and θ in the spherical coordinate defined relative to the unit vector along the donor dipole moment. Each coordinate is divided into 5,000 equal sized intervals. For a given angle θ_{DA} between the donor and the acceptor dipole, $\kappa^{1/3}$ can be calculated for each point in the (θ, ϕ) space. The range of $\kappa^{1/3}$ is also divided into 128 equal sized intervals in (0,1.26) or (0,$2^{1/3}$). Once $\kappa^{1/3}$ is obtained for each point in the (θ, ϕ) space, probability of finding $\kappa^{1/3}$ in the corresponding bin is increased by N*sin(θ). Here N is the normalization factor and sin(θ) is multiplied to account for the diminishing area as θ

approaches zero. In this way, the probability distribution of $\kappa^{1/3}$ is obtained for θ_{DA} =(0°,10° ,...,80°,90°). The result is shown in Fig.6.3.

One notices that the qualitative differences exist among different curves. More concentrated distribution with sharper peak can be seen for small angles between two dipoles. This could lead us to conclude that indeed the extra information of this angle can help us restrict the range of $\kappa^{1/3}$, but this is not the case as will be explained in the next paragraph. The apparent non-smoothness of the curves is not an artifact and multiple features in each curve is due to the fact that entirely different regions in the (θ, ϕ) space can give the same $\kappa^{1/3}$.

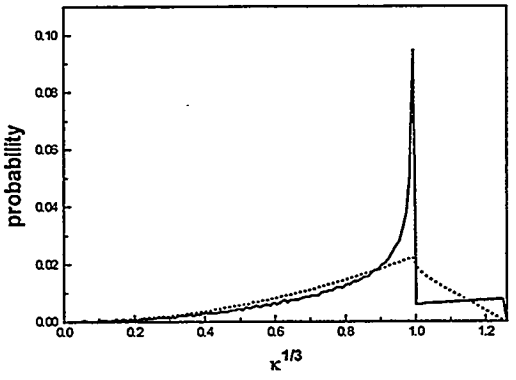

Fig.6.4. Probability distribution of $\kappa^{1/3}$ when no information is given (dotted line) and when the angle between two dipoles is known (0°).

To compare the above result with the case of completely unknown angles, a similar calculation is performed now in (θ_{DA} ,θ, ϕ) space. Each coordinate is divided into 100 equally sized intervals and the probability distribution is built by evaluating it for each point in (θ_{DA} ,θ, ϕ) space. Here, $\sin(\theta_{DA})$ is multiplied in addition to $\sin(\theta)$, for the same reason as described before. The result is shown as a dotted line in Fig.6.4. For comparison, the probability distribution for the case where θ_{DA} is known to be zero is also shown. Note that this is the most extreme case with the most narrow probability distribution among all cases. In evaluating the range of $\kappa^{1/3}$, we need to state the confidence level with which $\kappa^{1/3}$ falls within that range. When 76% of confidence level is sought (one standard deviation for the standard distribution), $0.62 < \kappa^{1/3} < 1.13$ when no information of angles is available, and $0.57 < \kappa^{1/3} < 1.08$ when θ_{DA} is known to be zero meaning that close to 100% error is possible for both cases. When 95% of confidence level is sought (two standard deviation for the standard distribution), even larger error up to 300% is possible

since $0.38 < \kappa^{1/3} < 1.20$ when no information of angles is available, and $0.44 < \kappa^{1/3} < 1.26$ when θ_{DA} is known to be zero. This result proves that the knowledge of one angle θ_{DA} does not help us reduce the uncertainly in the static distance determination.

If additional information is available due to particular interactions between fluorophores and the macromolecules or the surface, it could reduce the uncertainty in $\kappa^{1/3}$ significantly. For example, some fluorophores are known to intercalate between two strands of DNA in a specific way and others are known to bind to DNA along the minor groove. Although any specific example is not analyzed in this report, we believe that a certain information about the geometry can be beneficial in estimating the distance in some special cases. On the other hand, the knowledge of the dipole moment orientations can reveal important structural information about the macromolecule itself.

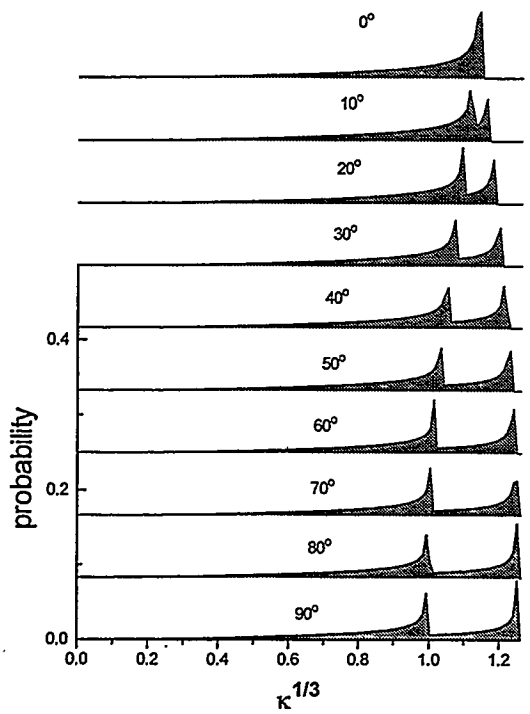

Fig.6.5. Probability distribution of $\kappa^{1/3}$ when the angle between two dipoles is known (0° to 90°) and two dipoles and radius vector are on the same plane.

In the sample preparation employed in this work, the surface normal component of the dipole moment is negligible because near-field imaging revealed no such features. Therefore, full determination of dipole orientation in the plane is enough for evaluating the angle between two dipoles. In addition, we may assume that the radius vector is in the plane. This is a reasonable assumption because two fluorophore are likely to be flat on the surface and the distance between them is around 5nm and is probably much larger than the height difference between two fluorophores. With this additional restriction, we calculated the probability distribution of $\kappa^{1/3}$ for a given angle θ_{DA} by evaluating $\kappa^{1/3}$ for each ϕ , the angle between the radius

vector and the donor dipole, in the range $0° < \phi < 180°$. The result is shown in Fig.6.5. Even though the result is quite distinct from the case of unknown radius vector in three dimensions shown before, the conclusion is the same. When the range of $\kappa^{1/3}$ is calculated with a confidence level of 76% or 95%, this knowledge of the angle between two dipoles and the assumption that the radius vector is in the plane hardly make any difference.

Another complication so far ignored is the fact that the absorption dipole moment is not always parallel to the dipole moment in emission.

Since the dipole dipole interaction in FRET involves the resonance between the donor emission and the acceptor absorption, the offset between the donor absorption and emission dipole orientation needs to be accounted for.

We conclude that for immobilized molecules, the orientational factor κ^2 has a larger uncertainty than in typical ensemble measurement in solution because time averaging is not possible and it cannot be fully determined.

The emission spectra are known to have distributions larger than the width of the individual spectral peak and there is no simple way of measuring absorption spectra. However, if there is a well defined relation between the emission and the absorption spectra of the acceptor molecules, *J*, the spectral overlap integral, can be estimated from the donor and acceptor emission spectra. This assumption is supported by the fact that when the emission spectrum shifts in wavelength, the total emission changes as well, suggesting that the absorption spectrum is closely coupled to the emission spectrum (see Chapter 5). It is still clear that the use of ensemble value of *J* is ill-advised because *J* for each pair can differ significantly from the ensemble value.

The quantum yields of donor and acceptor are not readily measurable on a single molecule basis. For molecules known to have quantum yield close to 1, it is plausible to assume that the quantum yield for individual molecules is 1. However, ensemble quantum yields of Texas Red and Tetramethylrhodamine (the acceptor and donor molecule in our experiment respectively) reported in literature are 0.5 and 0.25 respectively and therefore

potential variations on a single molecule basis cannot be ignored. One possible source of variations on the quantum yield is the surface normal component of the dipole moment. Radiative decay rate decreases when the dipole is closer to the surface normal, resulting in the increased excited state lifetime. Since the quantum yield is the ratio between the radiative decay rate and the total decay rate, it is expected to be smaller for the molecules with dipole moment normal to the surface.

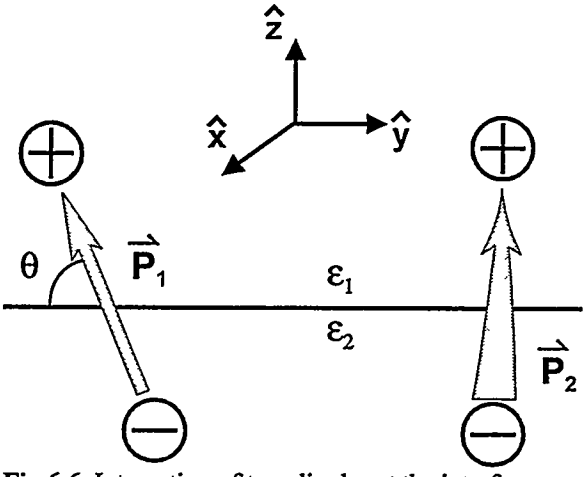

Fig.6.6. Interaction of two dipoles at the interface between two media.

In the case of immobilized molecules on an air-solid or water-solid interfaces, the effective index of refraction depends on the dipole orientations of donor and acceptor. To illustrated this point, we calculate the interaction energy between two static dipoles at the interface between two media of dielectric constants ε_1 and ε_2. (See Fig.6.6.) Dipole moments P_1 and P_2 originate from positive charges in medium 1 and negative charges in medium 2. We choose **z** along the surface normal and **x**, **y** axis are chosen such that $\mathbf{P}_1$ has no x component. Then we define four angles θ, ϕ, ξ, and φ in the following way. θ is the angle between $\mathbf{P}_1$ and the plane, ϕ is the angle between **x** and the radius vector from $\mathbf{P}_1$ and $\mathbf{P}_2$, ξ is the angle between $\mathbf{P}_2$ and the plane and φ is the angle between $\mathbf{P}_2$'s planar component and **x**. Then the potential of two charges making up $\mathbf{P}_2$ due to $\mathbf{P}_1$, calculated using image charge method, is proportional to κ'.

$$\kappa' = \frac{(\varepsilon_1+\varepsilon_2)^2 \sin\theta\sin\xi + 4\varepsilon_1\varepsilon_2\cos\theta\cos\xi\{\sin\varphi - 3\sin\phi\cos(\phi-\varphi)\}}{2\varepsilon_1\varepsilon_2(\varepsilon_1+\varepsilon_2)} \qquad (6.9)$$

If we set $\varepsilon_1 = \varepsilon_2 = 1$, this expression reduces back to the usual orientation factor κ as expected for homogeneous medium. In principle, κ needs to be modified in the presence of inhomogeneous media.

Let us consider special cases. If one of two dipoles are parallel to the interface ($\theta = 0°$ or $\xi = 0°$), then $\kappa'=2\kappa/(\varepsilon_1+\varepsilon_2)$, and the effective dielectric constant $(\varepsilon_1+\varepsilon_2)/2$ is the arithmetic mean of two dielectric constants. If one of two dipoles are normal to the surface ($\theta = 90°$ or $\xi = 90°$), then $\kappa'=\kappa(\varepsilon_1+\varepsilon_2)/2\ \varepsilon_1\varepsilon_2$, and the effective dielectric constant $2\ \varepsilon_1\varepsilon_2/(\varepsilon_1+\varepsilon_2)$ is the harmonic mean of two dielectric constants. For other configurations, the effective dielectric constant takes intermediate values. For the specific system of interest in our experiment, the medium 1 is air with $\varepsilon_1 = 1$, and the medium 2 is glass with $\varepsilon_2 = 1.5^2 = 2.25$. So the effective dielectric constant ranges between 1.38 and 1.63. Hence the effective refractive index ranges between 1.18 and 1.28 depending on the dipole orientations. This uncertainty is an much smaller effect compared to uncertainties in J, κ^2, and quantum yields.

Because of the above uncertainties, the prospect of spFRET as a quantitative tool to measure distances is not clear at this point. For immobilized molecules in solution, some of these parameters may closely follow the average values, however no information is available for such a system yet. Even if it is possible to utilize spFRET as a quantitative tool, the obtained information will be rather limited because individual pairs will exhibit a broad distributions in their distance due to the flexible linkage between the fluorophores and the macromolecule.

The most important advantage of spFRET over ensemble FRET is in dynamic measurements (Ha et al. 1996e; Keller et al. 1996). In conventional ensemble FRET measurements, which rely on signal averaging over many molecules, dynamic events such as relative motion between donor and acceptor molecules can not be detected because of the lack of synchronization of these events. The ability to measure FRET on a single pair potentially allows the study of time-dependent phenomena such as protein-

protein, protein-DNA and molecular motor conformational changes. It is our hope that spFRET will become a useful tool for the study of biochemical reactions at the single molecule level.

6.2.3. spFRET by emission spectrum - experimental demonstration

Initial spFRET results were obtained with NSOM, but it is believed that far-field measurement (with the confocal microscope) will also be possible, eliminating the strong perturbation by the near-field tip. The spectrum and excited state lifetime can be affected by the metallic-coating of the NSOM tip (Ambrose et al. 1994a; Bian et al. 1995; Trautman and Macklin 1996; Xie and Dunn 1994) At room temperature, the tip has little effect on single molecule spectra, although it can have a significant effect on the lifetime. Alteration of lifetime can affect the efficiency of energy transfer although such an effect would not be expected to invalidate the underlying Förster theory. Even though the tip effect on energy transfer was not pursued in this work, we note that quantitative measurements of distances and their relation to energy transfer efficiencies would require investigation of the tip effect.

As a model system, we studied single pair of tetramethylrhodamine (TMR) dye molecule (d, the donor) and Texas Red (TR) dye molecule (a, the acceptor) attached to the 5' ends of hybridized, complementary 10 or 20 bases long DNA strands (Fig.6.7). The main criteria in selecting two fluorophores are good photo-stability and good spectral overlap. In terms of photo-stability, there are molecules that are known to be more photo-stable than our choices. For example, DiI studied by Bell Lab group (Betzig and Chichester 1993; Trautman et al. 1994) has extremely good photo-stability (10^6~10^8 photons emitted before photo-destruction and roughly 10^6 photons are required for average quality emission spectrum) and unity quantum yield when placed on a polymer

matrix (PMMA). Photo-stability of TMR and TR are highly sample dependent and also molecule dependent, but its range is 10^4~10^7. Quantum yields reported in solution measurements are 0.25 and 0.5 respectively. Spectral overlap between them is excellent as can be seen in Fig.6.8. Relatively long R_0 of 50Å is expected based on this measurement assuming that the donor quantum yield is 0.25 and that κ^2 is 2/3, the time averaged value for fast rotation. Selection of the pair was also influenced by the need to put them at a well defined separation using a rigid linker. Because the resolution of the microscope (near-field or far-field) falls far short of the relevant distance scale for energy transfer, each pair has to be isolated from other pairs and it is essential to build a pair using a rigid linker molecule. Very natural choice is DNA molecule because it has been already used for ensemble measurements in solution, the chemistry of binding TMR and TR to DNA molecules using a flexible carbon chain is well understood and the DNA molecule is relatively stiff in its duplex form in solution. Details of the DNA-fluorophore synthesize and the results of preliminary solution measurements follow.

DNA Synthesis

As a model system, we measured energy transfer between a single tetramethylrhodamine dye molecule (TMR, the donor) and a single Texas Red dye molecule (TR, the acceptor) attached to the 5' ends of hybridized, complementary DNA of length 10 or 20 bases (Fig.6.7.). DNA oligomers of the appropriate length were synthesized by standard phosphoramidite technology with a 6-carbon aminophosphoramidite (Glen Research, Sterling Virginia) placed at the 5' end. The donor strand, labeled with the 5-isomer of tetramethylrhodamine isothiocyanate (TMR, Molecular Probes, Eugene Oregon), was 5'-CCACTCTAGG-3' and 5'-CCACTGCACTCGCTGCTAGG-3' for the 10- and 20-mer, respectively. Complementary oligos were synthesized and labeled with Texas Red (TR, Molecular

Probes). Unlabeled strands were also synthesized. All DNA was reverse-phase HPLC purified. For the spectroscopy, strands were dissolved in buffer containing 10 mM Tris-HCl, pH 8.0, 15 mM $MgCl_2$, 100 mM NaCl and hybridized by mixing, heating to 65° C and cooling to 5° C over 15 minutes at approximately 200nM. Donor-only and acceptor-only samples were also made by hybridizing the d-DNA or a-DNA to an unlabeled complement. (We denote the doubly-labeled samples as d-10-a and d-20-a, and the singly labeled, double-stranded samples as d-10, a-10, and d-20, a-20). A titration measuring donor-quenching of TMR-labeled DNA upon addition of TR-labeled DNA was used to verify concentrations and the extent of hybridization. For the d-DNA-a sample, an approximately 1:1 ratio of DNA strands was used; for the donor-only, and acceptor-only sample, a 2-fold excess of unlabeled, complementary strand was used to increase the probability that all dye-labeled DNA was in double-stranded form.

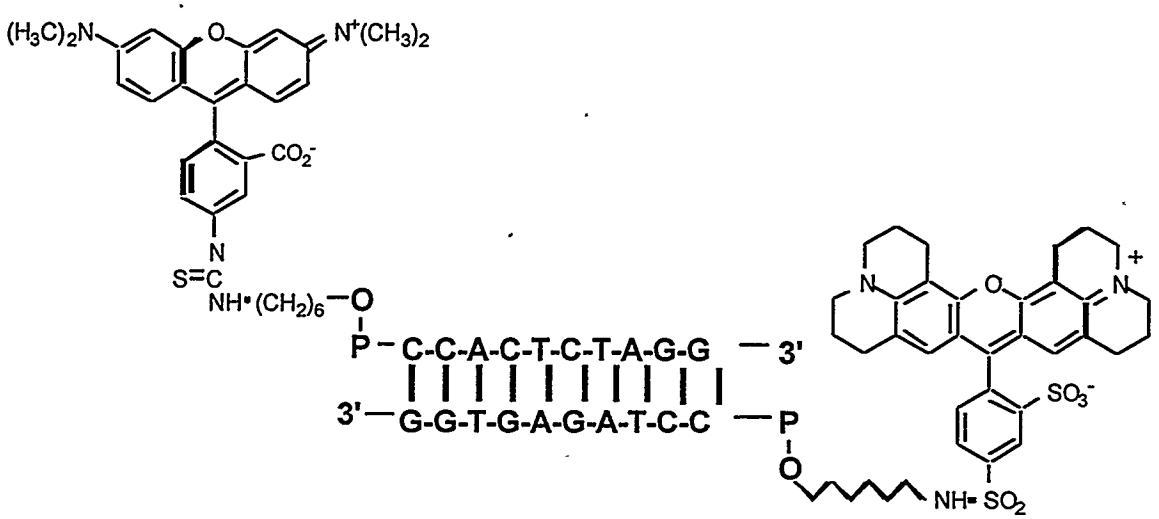

Fig.6.7. Model system of single pair of donor and acceptor fluorophore. The donor is tetramethylrhodamine (TMR) and is attached to the 5' end of a single strand of DNA (10mer or 20mer) through a flexible link of 6 carbon chain. The acceptor is Texas red (TR) and is also bound to a single strand of DNA complementary to the donor strand.

Solution (ensemble) FRET Measurements

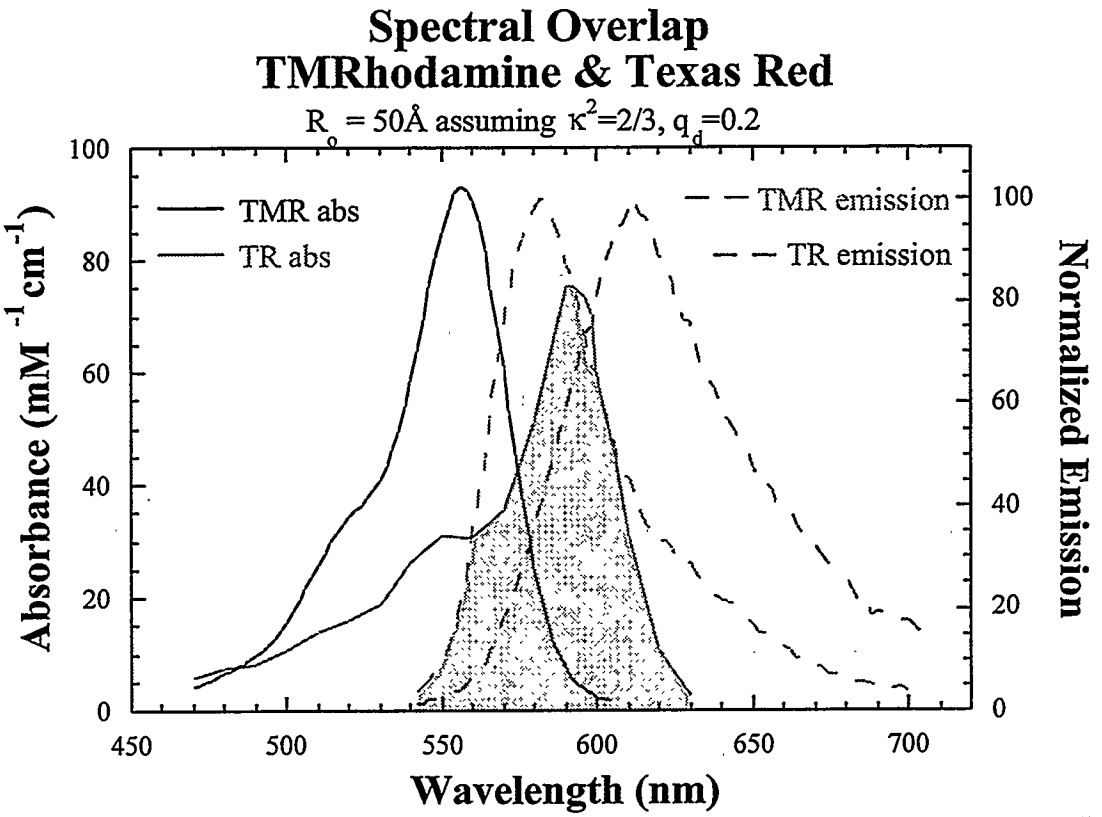

Fig.6.8. Solution spectra of donor-DNA system and acceptor-DNA system. Absorption spectra are in solid lines and emission spectra are in dashed lines. The spectral overlap between the donor emission and the acceptor absorption is considerable and is schematically shaded. Based on the solution measurement, R_0 of 50 Å is calculated assuming $\kappa^2=2/3$ and $q_d=0.2$.

Conventional solution (ensemble) measurements were made on a SPEX fluorolog steady-state fluorimeter. Energy transfer was determined by comparing the relative fluorescence spectra and intensities of d-DNA-a, d-DNA and a-DNA and measuring donor-quenching and sensitized emission according to standard methods. We measured 65% energy transfer on the d-10-a sample, indicating the donor and acceptor were approximately 40 Å apart in solution, and 32% energy transfer for the 20mer sample, which indicated 59Å separation in solution. Estimated distances were based on an R_o of 52Å ($R = R_o[E^{-1}-1]^{1/6}$). R_o was calculated using a measured spectral overlap of $J = 4.2 \times 10^{15}$ $nm^4M^{-1}cm^{-1}$, a TMR quantum yield of 0.25, a κ^2 of 2/3 and an index of refraction

of 1.33. The polarization anisotropy of the d-20 and a-20 were also measured and found to be 0.17 and 0.16, respectively, indicating that the assumption of $\kappa^2 = 2/3$, and therefore the derived-distances, are only rough approximations. In addition, the relatively high anisotropy measurements and the large amount of energy transfer on the 20-mer indicate that, in solution, the dyes are strongly interacting with the DNA and the flexible 6-carbon linkers may enable the dyes to fold back so they are closer together than their points of attachment to the DNA.

NSOM-FRET Measurements

For NSOM-FRET measurements, the DNA was dried on amino-propyl-silanized (APS) glass. Slides were made by washing glass coverslips for 2 minutes in a 1.5% solution (in H_2O) of 3-aminopropyl-triethoxysilane (United Chemical Technologies, Bristol, PA), followed by washing with H_2O, and then drying in a desiccator. Before use, the APS solution was filtered through a 0.2 μm filter and stored in HF-cleaned glassware. A 0.3 μL drop of 10-50 nM dsDNA solution in buffer was spread on APS treated coverslips in a 4°C cold room, followed by washing with H_2O and drying with nitrogen gas.

This preparation resulted in roughly 10 molecules per square micron in ideal cases but the success rate for the proper sample preparation strongly depends on the preparation conditions.

As a reference, emission spectra were taken on singly labeled DNA molecules (d-10, a-10). Fig.6.9 is a scatter plot of these emission spectra. Each single molecule is represented by the peak wavelength and full width half maximum (FWHM) of its emission spectrum. The average peak position and FWHM for the donor-only and acceptor-only are 566.4 ± 9.1 nm, FWHM 34.8 ± 4.9 nm, and 601.6 ± 12.2 nm, FWHM

34.1 ± 4.9 nm, respectively. The variance in these numbers reflects the inhomogeneity due to different local environment. The 35 nm difference in average peak position between donor-only and acceptor-only is three times the uncertainty in their peak positions, indicating that donor-only and acceptor-only spectra can be easily distinguished. These results are also used as base functions when two peaked emission is fit with donor and acceptor components.

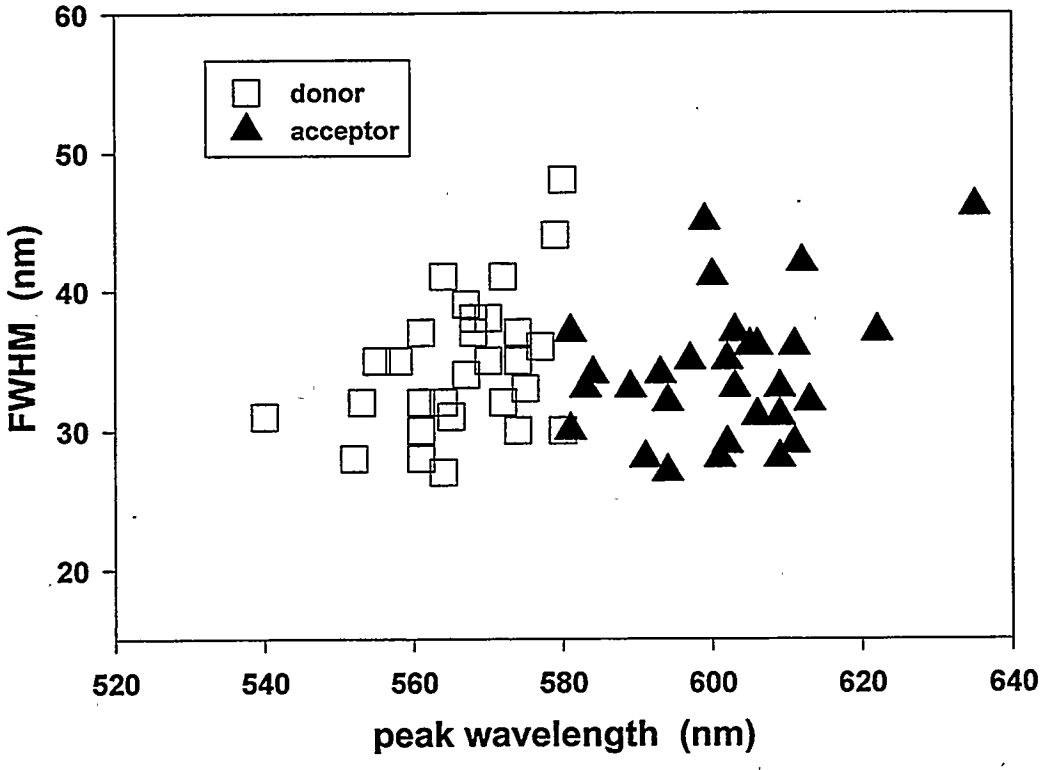

Fig.6.9. Scatter plot of emission spectra of donor labeled DNA and acceptor labeled DNA. Empty squares are donors and filled triangles are acceptors. Each single molecule is represented by the peak wavelength and full width half maximum (FWHM) of its emission spectrum.

In Fig.6.10, fluorescence images taken on the d-DNA-a sample with NSOM are shown. Since the pair complex itself (<10nm) is much smaller than the aperture size (100nm), each pair shows up as a single spot as in the single molecule case. To obtain

these images simultaneously, the emission is split into two channels, donor channel and acceptor channel using a dichroic mirror with a cutoff at 600nm.

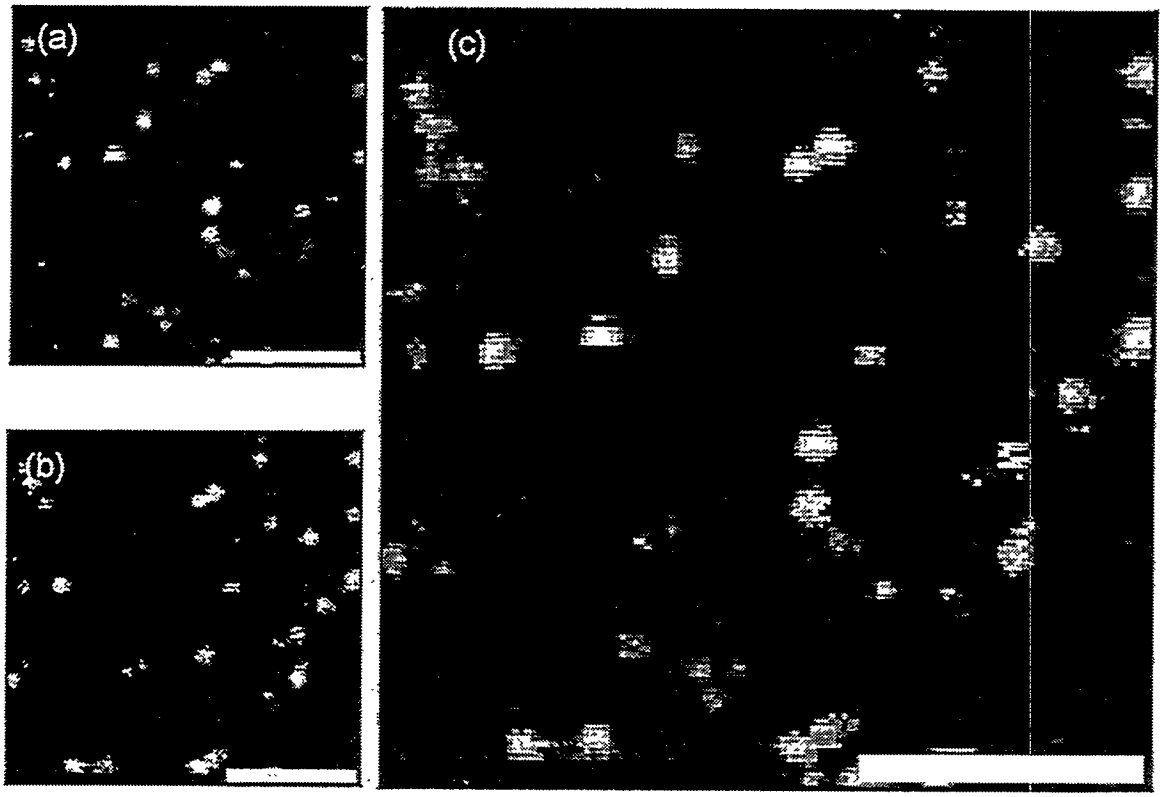

Fig.6.10. Two-color near-field scanning fluorescence images of doubly labeled DNA molecules (scale bar is 1 μm). (a) is for the donor channel image and (b) is for the acceptor channel. Both images were obtained *simultaneously* by separating the emission with a dichroic mirror. The two color images are overlaid to form the composite image of (c). The correlation between (a) and (b) can be used as a crude estimate of the degree of DNA hybridization on the dry surface.

The donor channel image is shown in Fig.6.10a and the acceptor channel image shown in Fig.6.10b. By analyzing the distribution of spots in two channel images, a crude estimate of the degree of DNA hybridization on the dry surface may be made. For example, comparable signal strength on the same spot in both channels could imply simultaneous emission from both donor and acceptor. However, because of strong cross-talk and polarization dependence of the dichroic response (see the previous chapter), and because of the relatively wide distribution of donor and acceptor spectra, absolute discrimination between donor and acceptor emission or collective pair emission is difficult. Much better spectral resolution is obtained with emission spectroscopy, which makes it possible to distinguish the donor emission from the acceptor emission. In this

work, we have measured energy transfer on a single pair by monitoring the emission spectra as a function of time. Another scheme that does not involve the emission spectroscopy is two channel detection with polarization modulated excitation. This unique scheme will be proposed later together with feasibility and limitation considerations.

30% of the d-20-a molecules examined exhibited two peaks in their emission spectra, indicating that the DNA molecule was indeed hybridized on the dried solid surface, bringing the donor-acceptor pair to close proximity. A typical two-peaked spectrum for d-20-a is shown in Fig.6.11a.

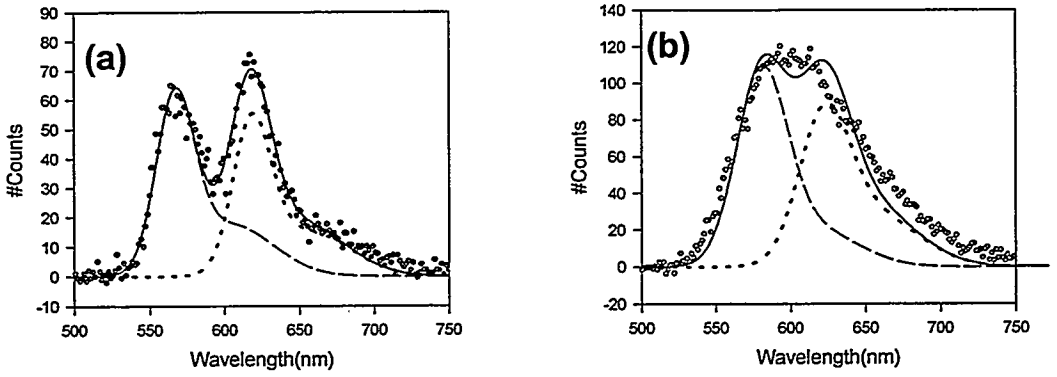

Fig.6.11. Typical spectra (gray circles) obtained on single TMR-20-TR (a) and single TMR-10-TR (b) samples. A small background remains after bleaching of both molecules, and has been subtracted. TMR and TR base-functions are used to fit (a) and (b). The data in (a) can be fit well (solid line) to a superposition of donor (dashed-line) and acceptor (dotted-line) emission, while the broad and featureless spectrum in (b) cannot be fit well

The data can be fit well (solid line) to a superposition of donor (dashed-line) and acceptor (dotted-line) emission spectra obtained by taking many single molecule spectra of d-DNA and a-DNA. Fitting was accomplished by starting with the average donor-only and acceptor-only two-Gaussian curve-fits and allowing the FWHM and the peak positions to vary within their experimentally-determined limits. The excellent fit indicates that any interaction between the two molecules is sufficiently weak that the individual emission characteristics are not perturbed. This weak-coupling indicates that Förster's theory should be applicable to an analysis of energy transfer on the d-20-a. Single peaked

spectra were also observed, most probably due to incomplete labeling, denaturing of the DNA, photo-destruction of donor or acceptor, unfavorable alignment either of dipole orientation or of spectral position, or complete energy transfer.

In contrast to the d-20-a data shown in Fig.6.11a, the typical emission spectra for the d-10-a sample, as shown in Fig.6.11b, cannot be fit well by a superposition of the donor and acceptor spectra. To achieve the fit shown in Fig.6.11b, it was necessary to use the extreme values for the FWHM of the donor-only and acceptor-only base functions (see Fig.6.9). This contrast between 10mer and 20mer samples is highly reproducible. A strong coupling, or Dexter exchange (Dexter 1953), may be present in the 10-mer case. No evidence for strong coupling was observed in solution and therefore the exact configuration of d-DNA-a molecule may be considerably different on a dry surface from that of solution.

Two-peaked emission such as in Fig.6.11a can arise either from independent emission of the donor and the acceptor (acceptor absorption at the 515.5 nm excitation wavelength is non-zero), or due to excitation of the donor, followed by energy transfer to the acceptor. In the following, we show how the dynamics of the photodestruction of the fluorophores can assist us in determining the presence and extent of energy transfer. We distinguish between two cases: 1) either the acceptor photobleaches first, or 2) the donor photobleaches first. If the acceptor photobleaches first (and at the same time stops absorbing light), then donor emission will increase if energy transfer is present, because the de-excitation channel provided by energy transfer is eliminated. If, however, the two-color emission is simply due to independent excitation and emission of the two fluorophores, donor emission will remain at the same intensity after bleaching of acceptor. In the second case, where the donor photobleaches first, the remaining direct excitation component of the acceptor emission can be measured and subtracted from the original two-color spectra. A non-zero difference spectra at the acceptor-emission component is evidence of energy transfer.

The extent of energy transfer can also be determined. If the acceptor photobleaches first, the efficiency of energy transfer is: $E = (I_D - I_{D_A})/(I_D - \alpha \cdot I_{D_A})$ where I_{D_A} is the integrated donor emission in the presence of acceptor (before acceptor photobleaching), I_D is the integrated donor emission after acceptor photobleaching, and α (<1) is the fraction of acceptor absorption which remains after photobleaching. Note that the α term is necessary because a photobleached acceptor (i.e. non-emitting) may potentially still absorb light. In the limit where $\alpha = 0$, this formula is equivalent to the conventional ensemble FRET formula used to measure E by a decrease in donor intensity. In the case where the donor photobleaches first, the efficiency of energy transfer is $E = [1 + (I_{D_A} / I_{A_D}) \cdot (\phi_A / \phi_D)]^{-1}$ where I_{D_A} is the integrated area of the donor emission in the presence of an unbleached acceptor, I_{A_D} is the integrated area of the sensitized emission of the acceptor, and ϕ is the quantum yield for the donor-only or acceptor-only complexes. (Sensitized emission is defined as acceptor emission due only to energy transfer, i.e., not including the fluorescence due to direct excitation.) This equation is identical to the equation used in ensemble-FRET when measuring energy transfer by sensitized emission of the acceptor.

Fig.6.12 and Fig.6.13 shows two cases of energy transfer between a single donor and a single acceptor. In Fig.6.12 and Fig.6.13a, the acceptor photobleaches first; in Fig.6.13b, the donor photobleaches first.

Fig.6.12 shows a continuous series of 5-second spectral scans of one donor-acceptor pair. Fig.6.13a highlights those scans in Fig.6.12 where sudden transitions occurred. Initially (black triangles, Fig.6.13a) fluorescence is predominantly due to acceptor emission (peak at 613 nm) with a small donor component (peak at 574 nm). During the 40th scan (200 sec., shown in arrow, Fig.6.12; gray squares in Fig.6.13a), the acceptor photobleaches and the donor emission rises. The 41st scan (black circles in Fig.6.13a) shows the final donor intensity after acceptor photobleaching. The sudden photobleaching of the acceptor emission is evidence for a single acceptor molecule, and

the corresponding sudden rise in donor emission is strong evidence that the acceptor absorption is significantly reduced after photobleaching and that energy transfer was occurring before the acceptor photobleached.

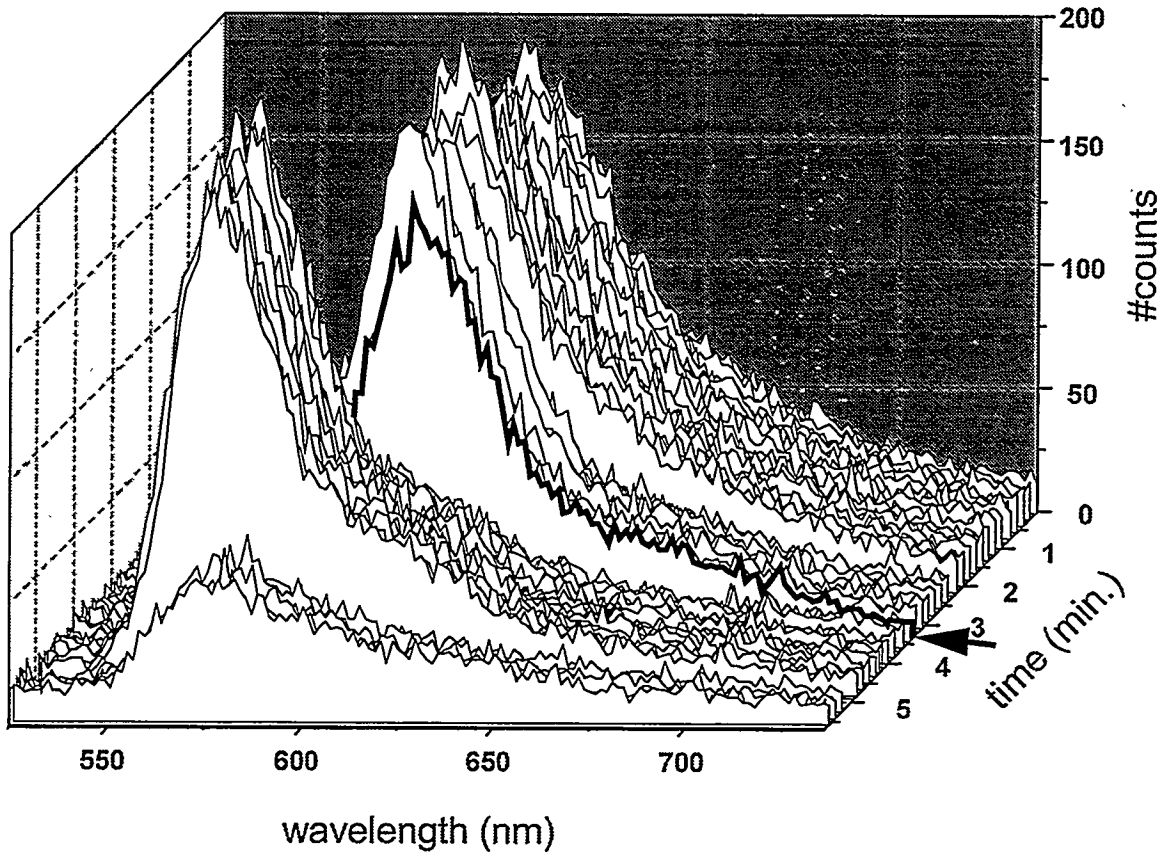

Fig.6.12. Time evolution of a single d-DNA-a pair emission spectra (5 sec/spectrum). Initially, fluorescence is predominantly acceptor emission with a small donor component. During the 40th scan (shown in arrow), the acceptor photobleaches and donor emission increases. At the 60th scan donor photobleaches as well, leaving only background signal.

The sudden donor photobleaching at the 60th scan (300 sec.) is evidence that donor emission is arising from a single donor molecule. From the difference in donor emission intensity between scans 39 and 41 (before and after photobleaching of acceptor), we estimate the energy transfer efficiency to be 85%. The extent of energy transfer is higher if some of the acceptor absorption remains after its emission quenching ($\alpha > 0$).

We have observed a simultaneous increase in donor emission with the photobleaching of the acceptor on three other different d-20-a pairs. We used the same fitting procedure as discussed above and estimated energy transfer efficiencies of 16%, 30% and 51% on

these additional pairs. This wide range in efficiencies (16% to 85%) is due to variances in distances, k^2, quantum yields and spectral overlap among pairs and is a manifestation of the inhomogeneity which comes from different local environments and structures. In particular, distance variation can come from the flexible 6-carbon linkages that can bring the dyes closer together, or farther away than their points of attachment on the DNA. The drying process on the APS treated glass can also contribute to variation in distances. For the particular 20-mer in Fig.6.12 and Fig.6.13a, it is difficult, though not impossible, to explain the 85% energy transfer if one assumes the DNA is in its usual B-form configuration. For this to be the case, the dyes must be aligned optimally for energy transfer (κ^2=4), the donor quantum yield must be one (leading to an R_o of 70 Å) and the flexible linkers must bring the dyes as close as possible, all of which would lead to a dye-dye separation of 52Å. It is therefore likely that the DNA on the surface, for this particular case, is not in its usual B-form. It may be bent by its interaction with the APS-glass or may be unhybridized and a donor and acceptor molecule from separate DNA single-strands are lying in close proximity to each other.

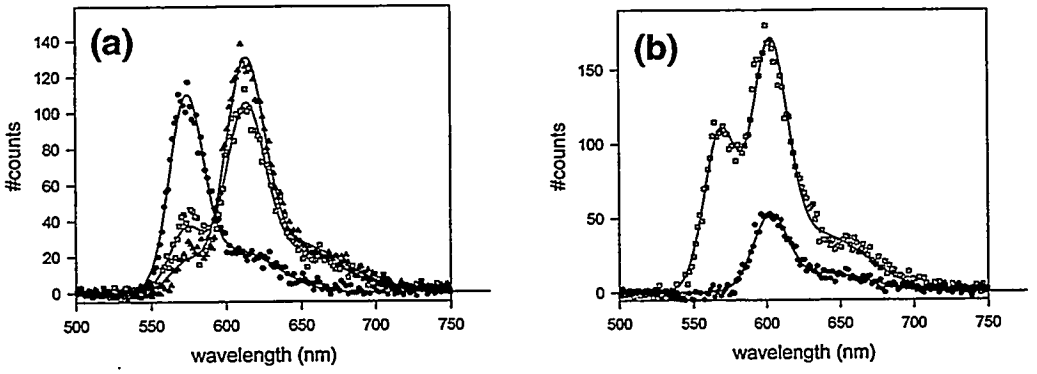

Fig.6.13. (a) Background-subtracted spectra of the previous figure in the 39th , 40th , and 41st scans (black triangles, gray squares, and black circles, respectively). Each spectrum is fit with a combination of donor and acceptor spectra and the fits are shown in solid lines. (b) An example for the case where donor photobleaches first. After the destruction of the donor (within the first scan), a reduced acceptor emission (due to direct excitation) is evident. The acceptor photobleached at the 16th scan. Solid lines are fit to the spectra. *E* is calculated to be 53%.

An alternative explanation for the data in Fig.6.13a, which does not involve energy transfer, can be postulated if three conditions are met: the two fluorophores have non-parallel dipole orientations; the acceptor absorption dipole is parallel to the excitation polarization; the DNA molecule holding the two chromophores undergoes 90° rotation around its long axis. This explanation is unlikely, however, because it requires three simultaneous and independent conditions to be met and because we have observed that sudden large decreases in molecular emission are not caused by rotation. This was done by simultaneously analyzing single molecule emission at two cross polarizations. Rotation would lead to anti-correlated signals; however, we observed a correlated decrease in both signals, indicating that the sudden decreases were due to photobleaching. Also polarization modulation spectroscopy showed that the rotation is a very rare event, and the molecules stay put within the observation window.

Also, we note that this two simultaneous events of acceptor photobleaching and donor emission increase are not caused by a simple spectral jump of a single molecule because the donor component was already present before the acceptor photobleaching and we have not seen a spectral jump of 40nm from a single molecule.

Fig.6.13b illustrates an example of energy transfer where the donor photobleaches first. The sudden photobleaching of the donor, followed at a later point by sudden photobleaching of the acceptor, is evidence that we are looking at a single donor and a single acceptor. After donor bleaching, a small but significant acceptor emission remains (black circles), which is due to direct excitation. By subtracting this direct excitation component from the initial spectrum (gray squares), and comparing the remaining areas due to donor and acceptor emission, we calculate the energy transfer efficiency to be 53%, assuming the donor and acceptor quantum yields are equal.

The data in Fig.6.12 and Fig.6.13 shows two particular cases. As mentioned before, donor emission was observed to increase upon acceptor photobleaching in four cases. We have also observed many cases where photobleaching of either donor or acceptor

does not cause a change in emission of the other, indicating no energy transfer, possibly due to unfavorable dipole-orientations for energy transfer. We have also found in many other cases, both peaks disappear simultaneously. In this case we cannot determine if -- or to what extent -- energy transfer is present. To increase the yield of usable data, the acceptor could be intentionally photobleached with a second excitation wavelength

6.2.4. spFRET with polarization modulation

In conventional FRET, donor and acceptor signals are distinguished by the spectrum only. And for good separation between the direct excitation component and the sensitized component of the acceptor emission, either new sample with donor only or acceptor only have to be prepared or an additional laser excitation should be used to selectively excite the acceptor only in the pair complex. Here, we propose a new way of making that distinction that is applicable to spFRET with added advantage of measuring two dipole orientations in the process.

In this scheme, the excitation polarization is modulated with as in Fig.4.4, while the signal from a pair is monitored in two channels. While sensitized emission will follow the same phase as the donor emission in the signal, the direct excitation component will in general have different phase. By carefully separating two sinusoidal signal from each channel signal, it would be possible 1) to measure the absorption dipole moments of both in the plane, 2) to estimate the donor emission, and two components of acceptor emission, and 3) to estimate the energy transfer efficiency as long as 1) two dipoles are not co-linear, 2) the acceptor photobleaches first, 3) and there is direct excitation component of the acceptor. Conceptual scheme with a simulated data is shown in Fig.6.14. To generate the simulated data, 80% energy transfer, 20% cross talk between channels, 45° between two dipoles are used. Also, the direct excitation component of the acceptor emission is

assumed to be half as strong as the donor emission in the absence of the energy transfer upon the same laser excitation. Signal on donor channel (empty circles) and acceptor channel (filled squares) are shown for repeated full 180° excitation polarization modulation with shot noise included. Solid lines are simulated signals without shot noise..

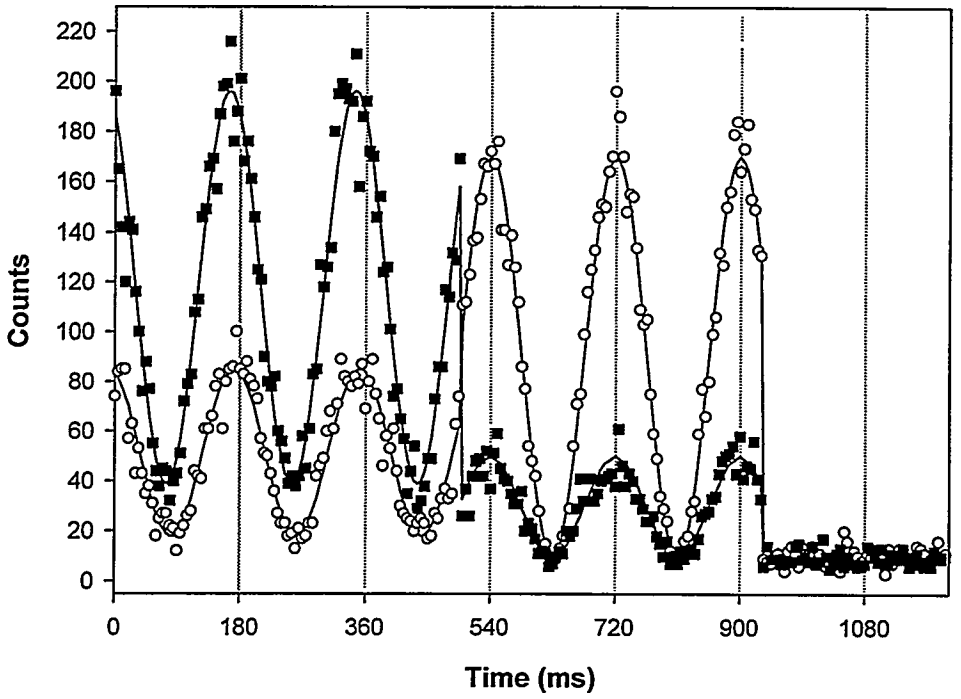

Fig.6.14 Simulated emission time traces of donor and acceptor pair complex showing the acceptor photobleaching at 500ms and the donor photobleaching at 930ms. Energy transfer efficiency and dipole orientations of both donor and acceptor may be determined from such a measurement.

Initially, signal is the mixture of two components with donor dipole orientation or acceptor dipole orientation and the modulation is not 100%. At 500ms, the acceptor photobleached leaving only donor component showing 100% modulation. At 930ms, the donor photobleached as well leaving background signal. From the donor emission only portion of the data, the donor dipole orientation and the donor emission in the absence of

the energy transfer can be found. This information can be used to fit earlier portion of the data with a combination two cosine square functions to extract the acceptor dipole orientation and the energy transfer efficiency. This information recovery scheme does not work if the donor photobleaches first because the remaining acceptor direct excitation does not yield any extra information. Applicability of this technique to real system with its own dynamics hence more noise should be a topic of future experimental and theoretical investigations. Note that this technique is valid only when the system dynamics happens with a slower time scale than the full modulation period. There is certainly a trade-off between how well two components with different phases can be separated and how much the signal is complicated by the system dynamics when longer integration time is used. The details of the experimental conditions will have to be chosen specific to the system under study, but it may be possible to study the energy transfer on a dynamic system if shorter integration time or smaller number of points across the polarization modulation are chosen.

6.2.5. Dynamic aspects of single pair FRET

Our goal in developing spFRET techniques is to apply them to the study of conformational changes of biological macromolecules. The two fluorophores will be attached to the points of interest on the macromolecule (macromolecules) and the emission from the pair will be monitored by two-channels detection with ms time resolution.

In general, the relative motion between the donor and the acceptor will entail both rotation and translation, both affecting the FRET signal. Rotation changes the amount of direct excitation by the laser, and affects the dipole-dipole interaction, hence the energy transfer efficiency. This, in turn, will change the signal ratio between the two channels.

The translation motion (distance changes) alters both the total signal and the ratio between the two channels due to the R^{-6} dependence of the dipole-dipole interaction.

For many applications, it will be useful to decouple rotation from translation. Combining spFRET with polarization modulation may offer a solution to this problem. A possible scheme is to use two different alternating excitation beams, one which excites the donor, the other which excites the acceptor directly. By repeatedly measuring the pair emission for a few linear polarizations (for example, 0°, 45° and 90°) and for each laser excitation, it will be possible to measure the in-plane component of the absorption dipole orientation of both molecules. Any change in orientation will show as change in the phase of the measured waveform, and will be easily detectable. Pure translation will change the total and the ratio signals but not the contrast between different polarizations. Intrinsic spectral jumps of each molecule can significantly complicate the interpretation, and the choice of stable fluorophores is, therefore, essential.

Out of many potential dynamic biological systems that single pair FRET technique can be used to study, we describe one examples. General criteria in evaluating the validity of single FRET technique for this may be applied to other systems as well.

Application of spFRET:Dynamic conformational changes in F_1F_0-ATPase

F_1F_0-type ATPases are a class of enzymes which utilize the energy of ATP to produce an electrical (proton) gradient across membranes. They can also run in "reverse" and synthesize ATP from ADP + P_i by utilizing a proton gradient. Hence, they are molecular motors that convert chemical energy into electrical energy, or visa-versa. They are found in the membranes of a wide variety of organisms, including in the plasma membranes of prokaryotes, in mitochondrial inner membranes of animal and plant cells, and in the chloroplast and thylakoid membranes of plants.

As their name implies, these molecular motors is made of two parts, F_1 and F_0, which are connected by a narrow stalk of approximately 40-45 Å in length. (The stalk is sometimes defined as part of F_1.) F_0 resides in the membrane and in E. Coli, consists of three subunits, a, b, and c. The F_1 contains the catalytic site for ATP hydrolysis and resides adjacent to the membrane. It consists of 5 different subunits, 3α, 3β, 1γ, 1δ, 1ε, with ATP-binding and catalysis occurring in the β subunit. The stalk is formed by the α-, δ- and ε-subunits. Each of the three β-subunit differs in nucleotide-binding occupancy (either empty, ADP+P_i or ATP-bound) and conformation. A vast amount of structural work has been done, including the recent crystallization at 2.8 Å resolution (Abrahams et al. 1994).

The structural features, combined with kinetic data, suggest a mechanism for catalysis that involves the binding of ATP to one of the αβ-subunits, (ADP+P_i is bound to another, and the third is empty), causing a 120° rotation of the αβ-subunits around the stalk, with a concurrent conformational change in the stalk (γ and ε subunits). This conformational changes in the γ and ε-subunits of the stalk may cause protonation of side-chains in the c-subunit of F_0, which aides unidirectional proton translocation across the membrane. Three such 120° rotations, or steps, complete the catalytic cycle. The rotation of the αβ subunits around the stalk is believed to be like a wobbling spinning top — the αβ rotates, but the center of mass of the stalk also moves. Capaldi et al., for example, has shown via cryoelectron microscopy that the center of mass of the ε and γ subunits change with respect to the α and β subunits, depending on the nucleotide-binding state (Capaldi 1994). Note that a conformational change in the stalk is essential for coupling the catalytic, ATP-binding region (ab subunits), to the proton translocation region (F_0 part). Recent real time observation of intersubunit rotation using polarized absorption relaxation is also compatible with the above model (Sabbert et al. 1996).

The structural work, while supporting this dynamic model for catalysis, is capable of only static measurements, or snapshots, of the molecule in motion. The crystal structure,

for example, is just one of several conformational states during this catalytic cycle. *In contrast, spFRET is potentially capable of measuring the relative distances between various parts of the enzyme in real time, on working motors.* The idea is to label the stalk with a donor fluorophore, and one of the αβ subunits with an acceptor, and monitor the extent of energy transfer as a function of time/ATP turnover. *With single-pair FRET it is not necessary to synchronize different motors, since single individual motors can be detected.* One successful energy transfer experiment on chloroplast F_1 has already been achieved to measure distances between the ε and γ subunits on the stalk (Richter et al. 1985). This experiment shows, in a limited way, that it is possible to label F_1 with energy-transfer pairs and maintain function (ATP hydrolysis), although no time-dependent work was done in this experiment, and the purpose was not to test the wobbly-top model. We discuss how to do this below.

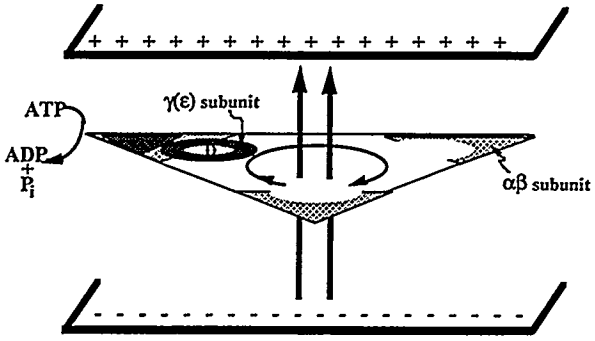

Fig.6.15. Schematics of F1-F0 molecular motor operation. Energy transfer monitored between the donor and acceptor labeled unit might yield the dynamical information of the motor in action.

Fig.6.15 shows a schematic diagram of the proposed FRET experiment. The ε and/or γ subunit on the stalk will be labeled with a donor fluorophore and one of the αβ subunits will be labeled with an acceptor fluorophore. The energy transfer, as measured by donor quenching and acceptor emission will be monitored as a function of time, and function of catalytic (ATP-binding) state. Both the isolated F_1 fragment, and the complete F_1F_O in lipid layers will be tested. If the wobbly-top model is correct, we expect to see a time-dependent, anti-correlated emission of donor and acceptor with an asymmetric duty cycle of 2:1.

There are several elements necessary for such an experiment to work.

• Distance scales appropriate for FRET?: The distance between the donor and acceptor molecules is expected to be on the order of 40-60 Å, (depending on the exact point of attachment of the fluorophores) and the distance changes on the order of 20 Å (see 4.2.1.). These distances are easily measured by FRET. Choosing FRET pairs with an R_0 of approximately 40-50Å makes the measurement optimally sensitive to these changes.

• Time-scales appropriate for FRET?: It is important that the time-scaled be slow enough such that a reasonable signal/noise can be accumulated. As discussed in previous sections, we have achieved sub-millisecond time resolution for the two channel detection with two APDs and 3-5 second time resolution with the spectrometer and CCD camera and further improvement on these numbers are possible with higher excitation in the far-field method as long as saturation limit is not reached. Detecting changes under normal multi-site catalysis will be challenging: the turnover rate is 20μmoles of ATP/sec/mg of enzyme, which, based on a molecular weight of 350kDaltons, yields approximately 7000 ATPs/enzyme/sec, or a characteristic time of 0.14 msec, which is at the limit of our current setup. Using modified ATPs which hydrolyze 30 times more slowly (Capaldi 1995), this then becomes 4.2msec, and by limiting the concentration of ATP, the motor can be stepped one 120° rotation at a time, and made essentially as slow as desired (so-called "uni-site catalysis" where at most one mole of ATP per mole of F_1 is present at any one time).

• Labeling Reaction: Both the stalk and αβ subunits must be labeled with different fluorophores, and the αβ subunit should be labeled such that, on average, less than one αβ subunit per ATPase is labeled. Essential to this approach is the availability of mutant ATPases with cysteines which can be uniquely labeled with fluorophores on both the stalk (ε and γ) and αβ subunits. Capaldi et al. has made a large number of such mutations with cysteines on both the stalk (ε and γ) and the αβ subunits and has shown that they are still active at near unmutated levels (Aggeler et al. 1995a; Aggeler et al. 1995b; Turina

and Capaldi 1994). He has also labeled them with different fluorophores and shown that they are still retain normal activity. In addition, these cysteines can be uniquely labeled in the intact enzyme, i.e. it is not necessary to isolate each subunit and reconstitute the enzyme. Hence it should be possible to label the stalk with one maleimide-fluorophore, and then label the $\alpha\beta$ subunit with another, different, maleimide fluorophore.

• Substrate Condition: For NSOM-based spFRET, it is necessary to place the ATPase on a surface. Both the F_1 alone or the F_0F_1 enzyme embedded in lipid vesicles can be placed on mica and remain active. AFM measurements on F_1 on mica have recently been made (Singh et al. 1995). We have already shown the ability to image single fluorophores on mica and found their stability/spectral characteristics to be similar to those on glass.

Another technological challenge to be met for the realization of this experiment is that single molecule spectroscopy under aqueous condition has to be established. A crucial element is the photostability of the fluorescent dyes such that enough photons are emitted to achieve high signal to noise before photodestruction. The photochemical properties of immobilized fluorescent molecules in aqueous environment need to be studied and optimized. The influence of oxygen concentration, pH, solvent polarity and radical and oxygen scavengers on quantum efficiency and photobleaching lifetime need to be studied.

6.3. Non-Resonant Dual Color Imaging (NRDCI)

6.3.1. Introduction

Usually, the dimensions of a single fluorophore molecule, emitting light in the visible, are under 10 Å. Therefore, it can be considered as a point light source. The response of the optical system - an optical microscope in this case - to a point source is

called the point-spread-function (PSF). It is of the order of the aperture size (600 - 1000 Å) for NSOM. For wide-field microscopy, PSF is given by a spot of diffraction limited radius $r = 1.22 \times \lambda_0 / 2 / NA$ where λ_0 is the wavelength and NA is the numerical aperture of the objective. Improvement of up to a factor of 1.4 can be obtained for confocal microscopy(Sheppard and Wilson 1978). For λ_0=5000 Å, and high numerical aperture, oil immersion objective (NA > 1), r ~ 2500 Å for a wide-field microscope and r ~ 1800 Å for a confocal microscope. According to the criteria set by Rayleigh, two such identical point sources (two fluorescent molecules) cannot be resolved if they are at a distance smaller than the PSF. Hence, the distance between two labeled points on a biological macromolecule, or between two macromolecules, cannot be determined with accuracy better than 600 Å for NSOM, and 1800 for confocal microscope and 2500 Å for wide field microscope.

The "molecular optical imaging" method recently proposed by Betzig (Betzig 1995) relies on the idea that molecules which differ in their optical properties can be isolated and located with an accuracy better than the PSF, and hence defying the Rayleigh criteria. Fig.6.16 illustrates this concept for the case of two molecules.

The uncertainty in localizing the center of the PSF is estimated from χ^2 maximum-likelihood analysis of the data and the knowledge of the PSF. The uncertainty δx, along the spatial coordinate x, is:(Betzig 1995; Bobroff 1986)

$$\delta x = (D/W \times N)^{1/2} \qquad (6.10)$$

where D is a number which depends on the number of parameters in the fit of the PSF and the desired confidence level, N is the number of data points from $-\beta\alpha$ to $\beta\alpha$ (the interval where the PSF is defined above a threshold level) and W is given, in the case of SMD (with Poisson statistics shot noise limited detection), by:

$$\Omega = 1/(2 \cdot \beta \cdot a) \int_{-\beta a}^{\beta a} (1/\mathrm{PSF}(x)) [\partial \mathrm{PSF}(x)/\partial x]^2 dx. \qquad (6.11)$$

As can be seen, the uncertainty δx depends on the inverse square-root of the number of data points and on the shape of the PSF and its gradient along the x direction. As shown

in (Betzig 1995; Bobroff 1986), δx can be on the order of 1/100 of the FWHM of the PSF.

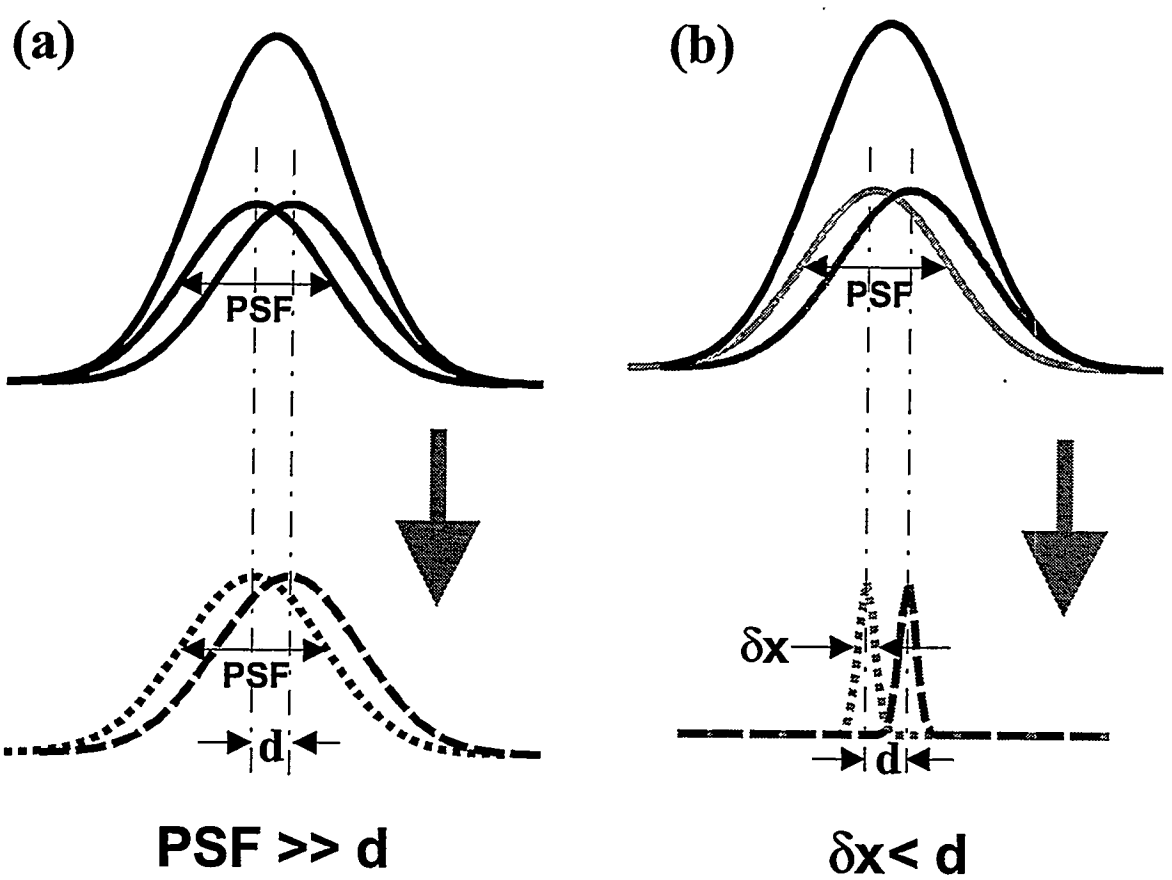

Fig.6.16. (a) Two hypothetical PSFs of two indistinguishable molecules which are separated by a distance smaller than the extent of their PSF. According to the Rayleigh criteria, the two molecules can not be resolved. (b) If, however, the two molecules are distinguishable by one or more optical properties (emission color, radiative lifetime, dipole orientation) symbolically shown by lines of different gray scales, their location and the distance between them can be determined with high precision.

6.3.2. The concept of Non-Resonant Dual Color Imaging

The possibility of locating a single molecule with accuracy of 1/100 of the instrument PSF is extremely interesting. Even more exciting is the possibility of locating *two near-by* molecules with such a precision and thus measuring their distance with the same resolution. However, the main challenge in doing so is to separate the signal from the two

molecules, while maintaining *perfect registry* between the two molecules. Dual-color excitation with NSOM permits exactly that.

The concept is to label the macromolecule with two different fluorophores, on two different sites whose distance is to be measured. In contrast to the spFRET case, the two fluorophores are chosen such that their spectra have no overlaps. The two molecules are excited independently at two different laser wavelengths. The light collection path includes a dual band-stop filter, which blocks the two excitation beams, but passes the emission from the two fluorophores; followed by the tube lens and a dichroic mirror that directs the two color emissions on two APDs (see Fig.6.17). The sample is scanned and two images are simultaneously acquired. Since both excitation colors share the same near-field aperture, the two images are in perfect alignment. The centers of the two PSFs of the two labeling molecules is then determined and the distance between them is extracted.

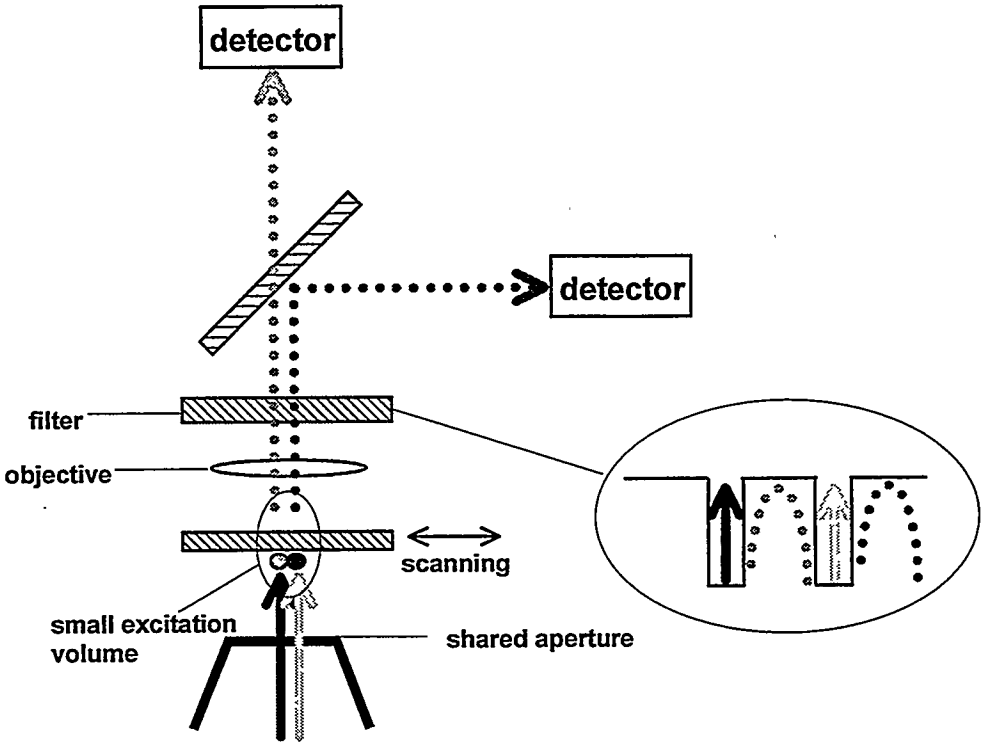

Fig.6.17. Schematics of NRDCI. Two color excitation (solid arrows) and two color emission (dotted arrows) are properly aligned spectrally to allow independent imaging of both molecules.

Potentially, NSOM-NRDCI can achieve differential resolution of a few nanometers because of its small PSF. However, since the NSOM PSF is strongly dependent on the aperture shape, which is generally not known, the accuracy in determining the PSF center is somewhat restricted. In addition, since the NSOM's PSF is sensitive to the dipole orientation of the molecule(Betzig and Chichester 1993), more parameters are needed for the fit thereby reducing the accuracy. In contrast to spFRET, however, this technique does not have an upper limit on resolution. Therefore, it can bridge the gap between FRET (10 - 70 Å) and far-field microscopies (2500 Å).

Optimal selection of fluorophores is very important since the resolution strongly depends on their photostability and the spectral separation between their emission. In contrast to cryogenic conditions, the emission spectrum of fluorophores at room temperature is much broader. Therefore, even with a careful choice of non-resonant fluorophores, considerable crosstalk between the channels is expected. This means that a "ghost" image of one molecule will show up on the other molecule image. Because of the long and asymmetric tail of the fluorophores' emission, the cross-talk from the short-wavelength molecule into the long-wavelength channel is more severe than the reverse.

Better isolation can be achieved if more than one "optical axis" is used. Besides spectral separation by the dichroic, gated photon detection can be used for lifetime discrimination, cross polarization excitation can be used for dipole orientation discrimination, and alternating the laser excitation between two wavelength and detection between two detectors can be used for excitation wavelength discrimination.

6.3.3. Preliminary result of NRDCI with NSOM

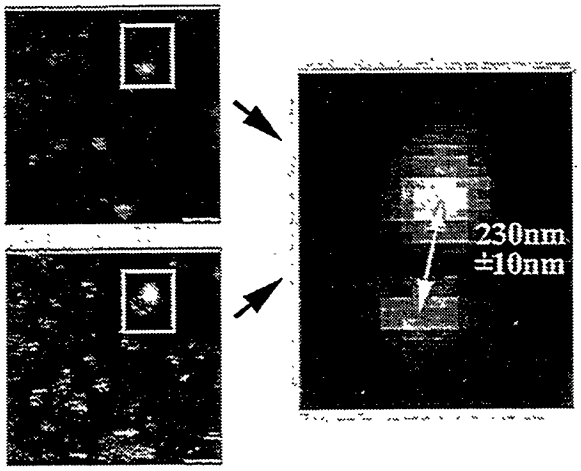

Fig.6.18. Near-field two color images of FITC (green) and Texas Red (red) molecules dispersed on a surface. A composite image of a zoom-in to the boxed area shows the PSF of the two near-by Texas Red and FITC molecules.

A preliminary experiment, which demonstrated the feasibility of the NSOM-NRDCI concept was performed. Fig.6.18 shows two images from two channels together with the composite image of the two molecules marked in the boxes. 488nm and 568nm excitation lines were simultaneously coupled to the NSOM fiber probe and dual-color emission images were taken. To minimize crosstalk between the channels, the two excitation beams were crossed-polarized. The fact that the Texas Red molecule shows up only in the one channel, and the FITC molecule shows up only in the other, is an evidence for a very good spectral separation. Qualitatively, it is clear from the figure that the location of the peak position can be determined with greater precision than the width of the PSF. Consequently, Fig.6.18 shows that the differential resolution in NRDCI is significantly better than the classical Raleigh criteria for diffraction-limited spots. We estimate that the peak position of each of the PSFs is resolved with 10nm accuracy. Future work will focus on labeled oligomers with distance between the two fluorophores smaller than their PSF extent.

6.3.4. Other implementation of Non-Resonant Dual Color Imaging

In contrast to NSOM, the PSF of a confocal microscope is well known (Pawley 1995), and can be accurately measured for a given objective. In this case, less parameters are needed for fitting the data, and hence reducing dx (Eq. (5.1)). However, ensuring that the two excitation colors occupy the same volume within the required differential

resolution is more difficult, because the two laser beams can undergo different chromatic aberrations in the illumination arm.

It may be possible to avoid two-color excitation, by using two sets of fluorophores with a common excitation wavelength but significantly different emission wavelengths. Compound fluorophores with a single excitation wavelength but Stokes shifts varying from 20-200 nm are now commercially available. Another interesting approach is to use two photon absorption to simultaneously excite both fluorophores. Recent studies of two photon confocal microscopy show that the two photon absorption spectrum is much broader than the single photon absorption spectrum while the emission spectrum is the same. Multicolor fluorescence imaging has been demonstrated by two photon absorption with a single laser excitation (Xu and Webb 1996). SMD with two photon excitation was also demonstrated (Mertz et al. 1995). Another possibility is to use a single excitation wavelength to excite two dyes with significantly different lifetimes, and utilize gated photon detection for the isolation of the emission from the two fluorophores.

6.3.5. Application of NRDCI: Protein induced Bending of DNA

We propose to apply our NRDCI technique to structural measurements of protein-induced DNA bends, specifically the bending of DNA caused by the binding of the bacterial protein Integration Host Factor (IHF). As a model system for the development and calibration of NRDCI, the system allows for the use of highly purified protein complexes with chemically characterized DNA targets. In addition, the bending (and looping) of DNA by proteins, which can bring distant sites into close proximity, is now known to be important in prokaryotic and eukaryotic gene regulation (Lobel and Schleif 1990; Wyman et al. 1995), and possibly in helping proteins recognize their binding sites (Guthold et al. 1994). IHF binds to a 36 bp A+T rich DNA binding site. IHF is known to

put a severe bend into the duplex DNA and has been measured previously using electron microscopy and gel-shift mobility. The bends were found to be approximately 130 degrees (Kosturko et al. 1989). Our fluorescence technique, like electron microscopy, is capable of looking at single molecules, and so one can do statistics concerning distribution of distances among many molecules. Our technique has the disadvantage in that it directly visualizes only a part of the complex (i.e. where the fluorophores are), but has the significant advantage of avoiding many artifacts associated with the sample preparation for electron microscopy. In both electron microscopy and our techniques, the sample must be laid on a surface, but Bustamante et. al. has shown in atomic force microscopy measurements that protein-DNA bending interactions are not significantly perturbed if laid on mica in an aqueous environment (Hansma et al. 1995). Gel electrophoresis measurements, while simple, are inherently averages over many molecules, over the course of hours, and are limited in solvent conditions. What are the expected distances? If we use a 36bp length of DNA and label both ends with FITC and TR as in the previous section, then, based on a simple calculation, we estimate that the two fluorophores will be approximately 125 Å apart in the absence of protein, and approximately 70-85 Å apart with protein bound, assuming the DNA is bent 130 degrees upon binding. These distances correspond to approximately 1/8 - 1/13 of the NSOM tip diameter of 1000 Å , which we expect to be measurable via our NRDCI technique.

7. FUTURE DIRECTION

In this dissertation, we have described our contributions to the exciting young field of single molecule spectroscopy. Compared to foreseeable and unforeseeable treasures that SMS may unearth in the future, only a handful of them has materialized. In this chapter, I will discuss a few experiments that we would like to carry out in the near future using the tools we have developed during the last three years. Presentation of these ideas will roughly follow the order of feasibility rather than of priority.

7.1. Tip induced effects on SMS

In any kind of scanning probe microscopies, the probe-sample interaction is an important topic because its understanding is essential for proper interpretation of the measurements. In near-field microscopy, the metallic coating of the tip, which hovers a few nanometers above the molecule, was shown to perturb the excited state lifetime of fluorescent molecules (Ambrose et al. 1994a; Bian et al. 1995; Trautman and Macklin 1996; Xie and Dunn 1994). Lifetime measurements as a function of the probe position relative to the molecule showed that the contrast between the glass and the metallic part of the tip depends on the height of the tip (Bian et al. 1995). Simple intensity measurement cannot be used in this case because when the tip moves, not only does the degree of quenching changes but also the excitation profile changes.

A measurement which can separate lifetime effects from intensity effects is of great interest. It can provide a nano-scale laboratory to study the fundamental physics of a single molecule near a metallic plane. In contrast to experiments done with the near-field microscope, we propose to decouple the excitation from the quencher (metal) by exciting the molecule with a focused laser light, through the glass substrate which supports the

molecule, rather than by the near-field tip. In order to perturb the emission properties of the molecule, an apertureless metallic, non-metallic or magnetic tip will be brought in close proximity to the molecule. The end face of this tip (with a few hundred nanometer diameter) will act as if it is an infinite metallic plane as long as the separation from the molecule is small. The shear force distance regulation scheme will be used to measure and to calibrate the tip-sample distance. Since the molecule will be excited in the far-field, excitation profile in the cavity formed by the glass and the metallic mirror can be well understood and direct interpretation of the emission intensity as a probe of the quenching process will be possible. Of course, lifetime can still be measured over longer range of probe-surface separation. A few different metallic and non-metallic surface can be studied. For example, metals which are known to support strong surface plasmon excitations will be compared with metals which do not. Moreover, studying the quenching effect as a function of the dipole angle from the surface normal will enable a direct test of the microscopic theory for a single dipole near a metal.

By applying a voltage to the tip, Stark shifts in the emission can also be studied. In general, the close proximity of a passive tip (a tip which perturbs the emission, but does not excite it) can be considered as an additional parameter which changes the molecular environment in a controllable way. The room temperature emission spectrum is not affected by the presence of the metallic surface because energy shift is much smaller than the width of the spectrum. But, in the case of single pair prepared for energy transfer measurement, the tip can have a dramatic effect on the total emission from the pair. Both the donor and the acceptor will be quenched by the tip, but the acceptor sensitized emission will be quenched doubly because the energy transfer process has to compete with the non-radiative decay path provided by the tip.

7.2. Cooperative quantum jumps on a pair of molecules

We have observed room temperature quantum jumps of single molecules (see Chapter 5). Since the first observation of quantum jumps from a single ion in the radio-frequency trap, it has been predicted that two or more ions trapped close-by would display collective effects such as super-radiance and correlated jumps (Hendriks and Nienhuis 1988; Lawande et al. 1989; Lewenstein and Javanainen 1987). Preparation of a pair of molecules at a well known separation is routine and is shown to work even on the dry surface for single pair FRET study (see Chapter 6). Combined with the quantum jumps observed from these molecules, it is natural to expect that this system could prove to be the right one to study collective effects on. Note that the dry condition is necessary because only then the triplet state lifetime is long enough for the individual jump to be resolved.

Another application of coupled system is to study the environmental effects on the spectral jumps and dark states. The environment changes have been shown to modify the properties of one molecule. Therefore, it would be interesting to know if the range of these changes is large enough to affect the other molecule 5nm away? Are we going to see correlated spectral jumps? To answer these questions, two molecules will have to be chosen such that they can be studied independently, as is the case in the non-resonant dual color techniques discussed previously (see Chapter 6).

7.3. SMS in solution

Room temperature single molecule detection has evolved in two distinct ways: diffusing molecules in solution and in flow, and immobilized molecules on dry surface. In the first case, a favorable molecular environment for biological molecules can be produced, by controlling the properties of the solution. However, it is hard to perform

spectroscopy on single molecules in these conditions because they stay in the excitation volume for only a few milliseconds. On the other hand, various spectroscopic measurements can be performed on immobilized molecules on dry surface, for their entire emission life. These spectroscopies, however, cannot be applied to the study of biological systems because of the "hostile" environment. We have developed a scheme for binding DNA-fluorophore complexes on a silanized glass surface. Preliminary measurements indicate that the complexes are still bound to the surface when immersed under water. We propose to perform single molecule spectroscopy (SMS) studies of single immobilized fluorophores under water. There are many interesting questions that may be answered by such studies: Is the spectral distribution of the molecular emission more homogeneous in solution? How fast is the photodestruction in various solutions? How does the interaction with the surface alter the triplet state lifetime compared to bulk solution measurements? Are the molecules tightly bound to the surface (as found on dry surfaces), or are they partially free to rotate? Most importantly, the emission properties of immobilized molecules can be studied as function of the solution properties (pH, salt content, oxygen content, etc.). These parameters can be varied while the emission from a single molecule is monitored in time.

7.4. Two photon SMS

Single molecule detection (SMD) by two photon absorption (TPA) excitation was demonstrated at room temperature for diffusing molecules in solution with femtosecond lasers (Mertz et al. 1995), and for molecules in solid matrix at cryogenic temperature with CW lasers (Plakhotnik et al. 1996). We propose to extend TPA-SMD to immobilized molecules at room temperature. Since the emission properties are independent of the

excitation, the TPA absorption properties can be investigated and compared to one photon excitation. Polarization dependent TPA cross section will be measured and will give information on optical selection rules for the two photon processes. TPA spectrum was shown to be much broader than single photon absorption spectrum from ensemble measurement (Xu and Webb 1996). By measuring the one photon and two photon excitation spectrum on a single molecule, it will be possible to compare and evaluate broadening mechanisms. If TPA spectrum is broad on a single molecule level, non-resonant dual color imaging in the far-field with a single excitation source will be possible. TPA-SMD has also a practical advantage over single photon SMD because it does not require UV excitation (most natural fluorophores require one UV photon excitation) and therefore does not require special UV optics.

7.5. Single pair FRET with polarization modulation

The scheme itself was described in single pair FRET part of the thesis. For experimental demonstration of this concept, we have to choose right molecules that are photostable and show less dynamics of its own.

7.6. Room/Low temperate single nanocrystal spectroscopy

Direct extension of SMS to the material science is to single semiconductor nanocrystals. Single CdS and CdSe nanocrystal have already been studied using far-field excitation, showing extremely narrow emission line, power broadening due to light induced spectral jumps, and luminescence intermittence due to photo-ionization. (Empedocles et al. 1996; Nirmal et al. 1996). We are currently building a low temperature module that can be incorporated into the detection and spectroscopy setup we have been

using. New types of nanocrystal will be studied with various spectroscopic tools we have developed. As a preparation, room temperature properties of single nanocrystals will be studied as well.

7.7. Quantitative single pair FRET

Previously, we used synthesized DNA molecules, with pre-determined length, to study interactions between fluorophores. However, the fluorophores were attached to the DNA by 6 carbon-linkers. These linkers are "soft", and when the DNA-fluorophore complexes were laid down on the glass surface, a distribution of distances and relative orientation between the two dipoles resulted. We will develop synthesis of DNA-fluorophore complexes in which the distance and the relative orientation between the two dipoles is fixed (for instance, by the use of base specific intercalating dyes and/or base specific minor/major groove dyes) to create a laboratory for the study of dipole-dipole interaction on a single molecule level.

APPENDIX A. AUTOMATED POSITIONING FOR SINGLE MOLECULE SPECTROSCOPY

The finite emission life of single molecules (governed by photodestruction) limits the total number of emitted photons which are available for both locating the molecule and for the subsequent spectroscopic measurement. The relatively high emission rate required for such "photon hungry" spectroscopies calls for: (1) efficient excitation of the molecule - by carefully centering it in the excitation volume (to obtain maximum signal to background ratio); (2) minimization of the time and the total number of photons required to find and center a single molecule (due to the finite emission life). Manual positioning, done by adjusting the *x-y* voltages of the sample stage piezo tubes is slow and "wastes" valuable photons and can often result in non-optimum positioning because of intrinsic sources of noise from the molecule itself. Many molecules can be destroyed in this process before a stable (and long lived) molecule is found. Such manual positioning selects only a smaller sub set - the most stable and long lived molecules - from a larger distribution. Since it is the molecules in the less stable environment that display interesting dynamics (such as spectral and rotational jumps and transitions to dark states), rapid positioning is necessary for successful spectroscopy of these molecules. For single molecule spectroscopy (SMS) in aqueous solution, where photodestruction efficiency is higher by up to three orders of magnitude compared to dry surfaces, automatic positioning will also be essential. Lastly, manual positioning is very tedious and time-consuming and is difficult to perform on a large number of molecules, while automation can produce large number of data sets, which can be analyzed statistically, and even very rare events can be found among the large number of data.

In this part, we describe an integrated computer controlled optical system which performs rapid automatic positioning of single molecules and subsequent SMS

measurements of various types. It was designed to either detect immobilized molecules on dry or wet surfaces, or with small adjustment to the algorithm, to perform SMS while tracking single moving molecules in liquid environment. The system was used to study single molecules with a confocal microscope and can be adopted for a near-field microscope as well (Ha et al. 1996a; Ha et al. 1996b).

Fig.A.1 shows the experimental set-up.

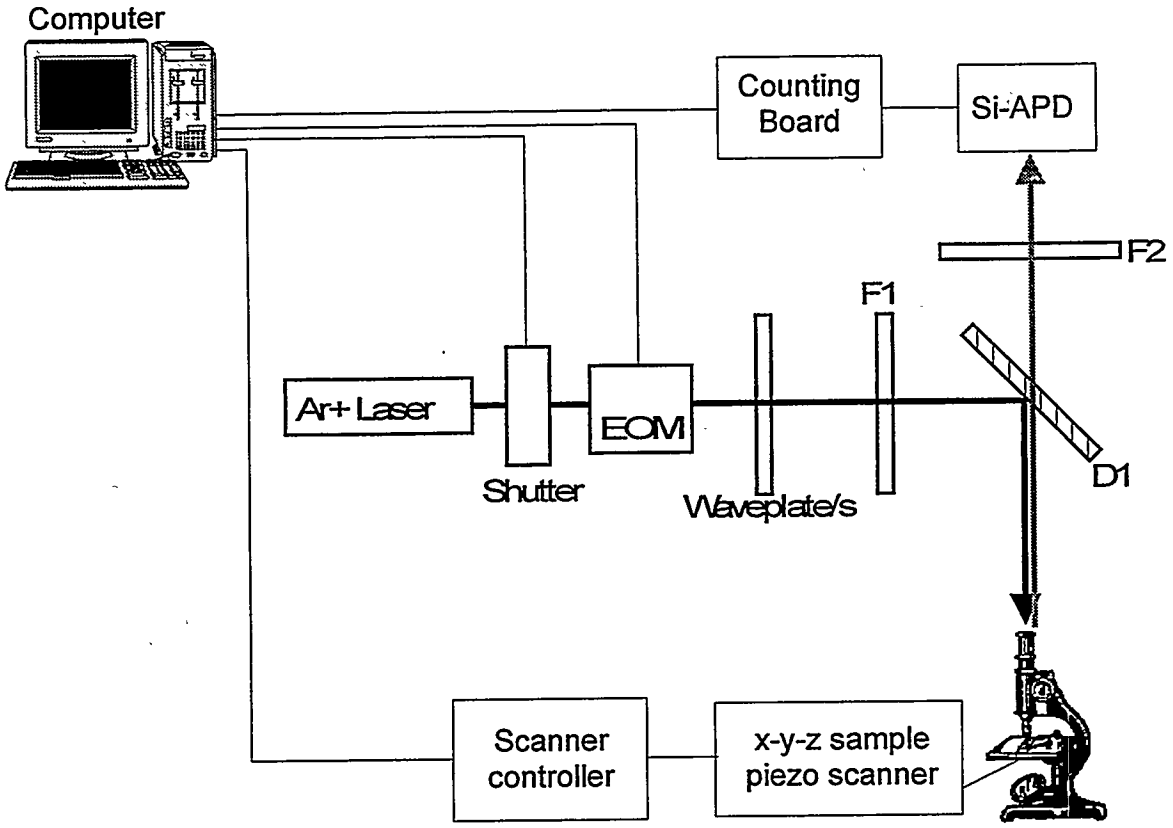

Fig.A.1. Schematics of the experiment: excitation light (thick line) is sent through a shutter, an electro-optic modulator (EOM), waveplates and laser line filter (F1), reflected by a dichroic mirror (D1) and focused on the sample with an oil-immersion objective. The emission (gray line) is collected with the same objective, transmitted though the dichroic and a longpass filter (F2) and imaged on a silicon avalanche photodiode (APD). TTL pulses from the APD are counted by the counting board. The scanner, shutter and electro-optic modulator are computer controlled.

Single molecules are excited at the confocal spot of an air-cooled Ar^+ laser light in the epi-illumination mode. The resulting molecular emission is collected and imaged onto a silicon avalanche photodiode (APD). The sample scan-head is controlled by a scanning controller which allows for external x and y voltage modulation supplied by the computer.

Computer program provides the voltage modulation for sample movement, controls the shutter and the electro-optic modulator for polarization and intensity modulation and reads the photon counts for each integration time from the APD via a counting board. Waveplates are used to control the polarization state of the excitation beam. The sample comprises of Texas Red (TR) molecules which are linked to single strands of DNA molecules bound to silanized glass coverslips.

The positioning of molecules in the excitation volume is divided into two subroutines: search and optimization. The algorithm implemented for search, optimization and subsequent SMS starts with scanning the sample stage as in the normal imaging mode, while monitoring the count rate from the APD. If the signal level exceeds a pre-set *background* threshold value, the scan stops and the optimization routine starts. This routine is a modified finite-difference method with a fixed step size (Gill et al. 1981): the sample stage is moved in the x direction by a small increment dx. If the signal decreases, the sign of dx is changed. The same is repeated for the y direction with $|dy| = |dx|$. After n such x-y increments cycles are repeated, the average value of the signal over the last $2n$ points is evaluated, until it reaches a level higher than another pre-set *signal* threshold value. If the optimization fails due to photodestruction or low signal level, the search subroutine resumes, from the coordinates where sample scanning was halted.

The algorithm of fixed increments in x and y was chosen (instead, for example, x-y crossing, or simplex (Gill et al. 1981)) in order to minimize the effect of piezo hysterisis and piezo creep (which make it difficult to move back to the desired points). Other unique aspects of the problem at hand are : (a) the two-dimensional fluorescence image of single molecules is the confocal point-spread-function (PSF), with a width of w_{PSF}=0.4mm. The *a-priory* knowledge of the two-dimensional signal surface simplifies the optimization problem. For example, an optimal step size for x-y incremental motion can be estimated for a given w_{PSF} (b) there are many sources of noise such as shot noise from photon counting, background counts, dark states of the molecular emission and

spectral jumps. Because of such noise, the experimental parameters have to be chosen more conservatively (longer integration time, more averaging).

In order to test the algorithm and find a reasonable starting set of parameters, we performed a simulation of locating a molecule using the above algorithm for various condition and compared it to the simplex algorithm.

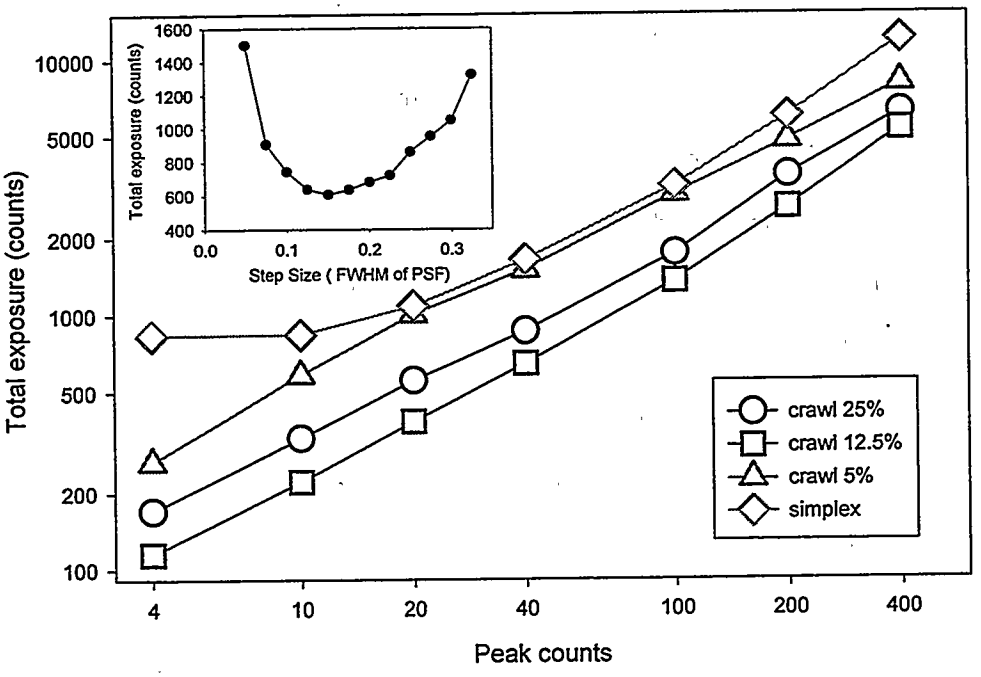

Fig.A.2. Simulated total number of counts, *N*, during positioning versus peak counts. Simulations were done with a modified finite difference method for optimization. Three different step sizes in units of FWHM of PSF (w_{PSF}) are shown. For comparison, the result from a simplex optimization algorithm is also presented (diamonds). The inset shows the dependence of *N* on step size for a fixed peak counts of 40.

We have approximated the PSF by a two-dimensional gaussian function and only shot noise was included. In Fig.A.2, *the figure of merit N*, defined as the total number of counts during the positioning, is plotted vs. the signal level on a log-log scale for various step sizes ($|dy| = |dx|$). The signal level is given in normalized units of peak counts (obtained during one integration period when the molecule is perfectly centered). *N*

decreases together with the signal level, but the decrease slows down for low signal levels due to the dominance of shot noise. The modified finite-difference algorithm works better than the carefully optimized simplex algorithm (reflection coefficient = 1.0, expansion coefficient = 1.5, and contraction coefficient = 0.6) for all signal level even in this ideal case, and the positioning of a molecule can be achieved with less than 1,000 counts. In the inset of Fig. 2, the step size dependence of N for a fixed signal level (40 peak counts) is shown. A clear minimum in the figure of merit is obtained for a step size of $0.15' w_{PSF}$. The existence of an optimal step size stems from the fact that with too small steps it takes too many increments to reach the peak, while with too big steps, the peak can be missed because of overshooting.

The above simulation is valid regardless of the data integration time: the same peak counts can be detected with high excitation and short integration time, or with low excitation and long integration time. However, the integration time in the actual experiment needs careful considerations for achieving high success rate in locating single molecules because of noise (see above). The integration time has to be much longer than the triplet state lifetime (which is sub millisecond for molecules on dry surfaces) but has to be fast enough to minimize the total exposure for given excitation intensity. Higher success rate for positioning molecules was achieved with relatively low excitation and long integration time allowing us to locate molecules with faster dynamics. With a typical value of 10 millisecond integration time, the algorithm was fast enough to finish the positioning process in one or two iterations of 20 points, namely 200 or 400 milliseconds before SMS subroutine started.

Fig.A.3 demonstrates a successful positioning. The lower curve shows photon counts from a single TR molecule. The rise in the signal over the first 200 ms (data points shown as empty squares, 10ms integration time) represents the optimization in positioning, obtained with a step size of $0.125' w_{PSF}$, to bring the molecule to the center of the excitation volume. At the end of the positioning period, the scan stage position was fixed,

integration time was reduced to 0.5 ms, excitation intensity was increased by a factor of 20 and photon counts were acquired as function of time (filled circles - note the difference in time scale) until the emission dropped to the background level due to the photodestruction. The sample stage x and y positions are shown at the top with solid black and solid gray lines respectively. The total number of detected photons from the molecule during the positioning period was 3400 while 6700 photons were detected during the data acquisition. This molecule and the ones shown in Fig.4 would not have survived a manual positioning which normally takes more than 200,000 counts (for example, 20kHz count rate and 10 seconds-long positioning).

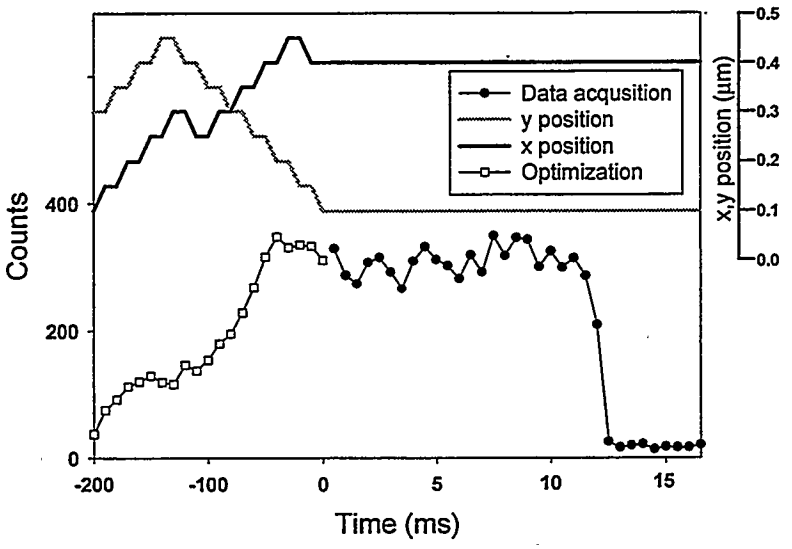

Fig.A.3. Time sequences of photon counts (squares during positioning, circles after positioning is completed), of x-position (solid black line), and of y-position (solid gray line). Note the difference in time scale. The step size for x,y increments was 0.125′ w_{PSF} (50nm). The integration time was reduced from 10ms to 0.5ms and the excitation intensity was increased by a factor of 20 after the positioning subroutine was completed.

Figs.A.4a and A.4b illustrate the immunity of the automated positioning to the molecular noise. Fig.A.4a shows positioning of a molecule which displays rapid telegraph noise, due to transitions to the triplet state (Ha et al. 1996f). For the optimization subroutine, integration time was set to 10ms (data points in open squares). Once the

molecule was positioned, excitation intensity was increased by 20 and integration time was reduced to 200ms (filled circles). Turn-on and off in the molecular emission, which are due to quantum jumps to the triplet state, are evident.

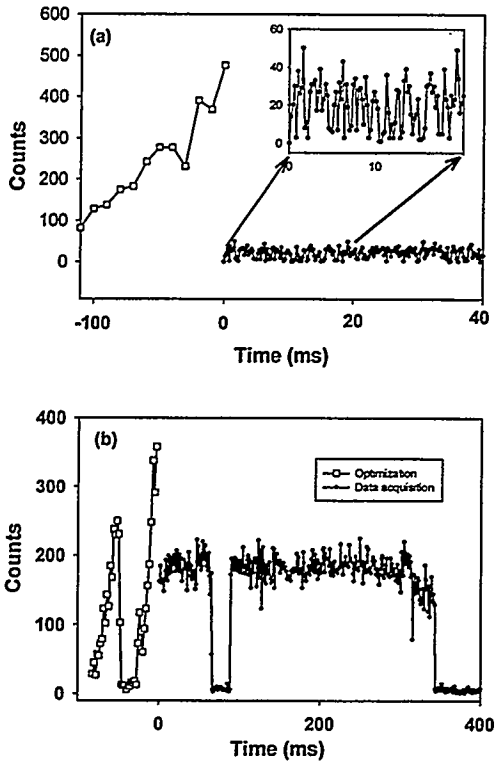

Fig.A.4. Immunity of the positioning algorithm to intrinsic noise: (a) quantum jumps to triplet states. Inset is the zoom-out showing individual jumps. 10ms integration for positioning and 0.2ms integration for data were used. (b) Long dark states during and after the completion of the positioning subroutine.

Since the PSF is known, the range of incremental motion during the optimization can be limited to the PSF extent. Therefore, even if the molecule transits to a long dark state during the optimization, the algorithm can still be resumed and finished successfully as long as the molecule returns to the fluorescent ground state in time. An example is given in Fig.A.4b. Two reversible transitions to long dark states, one during the optimization (empty squares) and one during the data acquisition (filled circles) were observed before the irreversible destruction of the molecule. The examples in Figs.A.4a and A.4b demonstrate that the optimization algorithm is robust enough to deal with intrinsic molecular fluctuations.

With the positioning tool in hand, various SMS spectroscopies could be performed. Two such spectroscopies are demonstrated in Fig.A.5. Single molecule fluorescence saturation spectroscopy was performed by intensity modulation. A representative data for these measurements is shown in Fig.A.5a. The search subroutine lasted for 100 ms (3 ms integration, empty squares), after which the intensity modulation spectroscopy subroutine started. The emission rate from a single molecule was recorded (1ms integration, filled

circles) while the excitation intensity was repeatedly modulated from I_0 to 20 I_0 ($I_0 = 2.5$ kW/cm^2). Saturation studies on a large number of molecules confirmed the extended triplet state lifetime on dry surfaces.

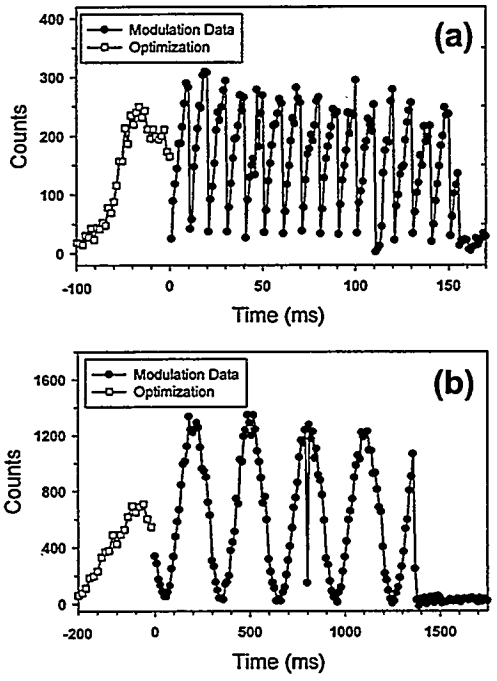

Fig.A.5. Intensity (a) and polarization (b) modulation spectroscopy performed after successful positioning. The modulation was done with an electro-optic modulator combined with a polarizer and/or a quarter-waveplate. Noise due to intrinsic molecular properties such as dark states and spectral jumps is evident both during the positioning and the modulation spectroscopy.

In Fig.A.5b, polarization modulation data is shown. Here, after the completion of a successful positioning in 200ms (10 ms integration), the emission time trace was recorded (10 ms integration, filled circles) while the excitation polarization was repeatedly modulated from 0^o to 150^o with 30 points per period . The 100% modulation depth with a $cos^2(t)$ time dependence is evidence for the fixed, single molecular dipole. This technique can be used to distinguish rotational jump from dark states and spectral jumps. In fact, due to automation, very rare events such as rotational jumps could be observed after studying hundreds of molecules. The data in Figs.A.5a and A.5b demonstrate the simplicity and the ease at which the search, optimization and modulation spectroscopy are combined to produce high quality spectroscopic data on single molecules.

The automated positioning technique was also applied to frequency resolved emission spectroscopy of a large number of molecules. At the end of the positioning subroutine, the photons were redirected from the APD to a spectrometer and a CCD camera for the acquisition of consecutive emission spectra. Compared to manual positioning, dynamical events such as spectral jumps and dark states were observed with

much higher frequency, and molecules with higher photodestruction efficiency could be observed. It is interesting to note, however, that the distribution of the spectral peak position for these molecules was not consistent with the ensemble spectrum measured on a more dense sample. This is due to the selection procedure which favors molecules in the blue wing of the distribution. Only those molecules have strong enough absorption at the laser wavelength and therefore have emission high above the *signal* threshold value. This point illustrates the danger in drawing general conclusions about the total population based on spectroscopy performed on many single molecules chosen by a specific selection rule.

REFERENCES

1. Abrahams, J. P., Leslie, A. G. W., Lutter, R., and Walker, J. E. (1994). "Structure at 2.8Å resolution of F1=ATPase from bovine heart mitochondria." *Nature*, 370, 621-628.
2. Aggeler, R., Haughton, M. A., and Capaldi, R. A. (1995a). "Disulfide bond formation between the COOH-terminal domain of the beta subunits and the gamma and epsilon subunits of the Escherichia coli F1-ATPase. Structural implications and functional consequences." *Journal of Biological Chemistry*, 270(16), 9185-9191.
3. Aggeler, R., Weinreich, F., and Capaldi, R. A. (1995b). "Arrangement of the epsilon subunit in the Escherichia coli ATP synthase from the reactivity of cysteine residues introduced at different positions in this subunit." *Biochimica et Biophysica Acta*, 1230(1-2), 62-68.
4. Ambrose, W. P., Basche, T., and Moerner, W. E. (1991). "Detection and Spectroscopy Of Single Pentacene Molecules In a Para-Terphenyl Crystal By Means Of Fluorescence Excitation." *Journal Of Chemical Physics*, 95(10), 7150-7163.
5. Ambrose, W. P., Goodwin, P. M., Martin, J. C., and Keller, R. A. (1994a). "Alterations Of Single Molecule Fluorescence Lifetimes In Near-Field Optical Microscopy." *Science*, 265(5170), 364-367.
6. Ambrose, W. P., Goodwin, P. M., Martin, J. C., and Keller, R. A. (1994b). "Single Molecule Detection and Photochemistry On a Surface Using Near-Field Optical Excitation." *Physical Review Letters*, 72(1), 160-163.
7. Ambrose, W. P., and Moerner, W. E. (1991). "Fluorescence Spectroscopy and Spectral Diffusion Of Single Impurity Molecules In a Crystal." *Nature*, 349(6306), 225-227.
8. Asimov, M. M., Gavrilenko, V. N., and Rubinov, A. N. (1990). "Laser Photolysis Of Laser Dyes and the Influence Of Triplet Quenchers." *Journal Of Luminescence*, 46(4), 243-249.
9. Basche, T., Kummer, S., and Brauchle, C. (1995). "Direct Spectroscopic Observation Of Quantum Jumps Of a Single Molecule." *Nature*, 373(6510), 132-134.
10. Basche, T., and Moerner, W. E. (1992). "Optical Modification Of a Single Impurity Molecule In a Solid." *Nature*, 355(6358), 335-337.
11. Basche, T., Moerner, W. E., Orrit, M., and Talon, H. (1992). "Photon Antibunching In the Fluorescence Of a Single Dye Molecule Trapped In a Solid." *Physical Review Letters*, 69(10), 1516-1519.
12. Bergquist, J. C., Hulet, R. G., Itano, W. M., and Wineland, D. J. (1986). "Observation of quantum jumps in a single atom." *Physical Review Letters*, 57(14), 1699-702.
13. Bethe, H. A. (1944). *Physical Review*, 66, 163.
14. Betzig, E. (1995). "Proposed Method For Molecular Optical Imaging." *Optics Letters*, 20(3), 237-239.

15. Betzig, E., and Chichester, R. J. (1993). "Single Molecules Observed By Near-Field Scanning Optical Microscopy." *Science*, 262(5138), 1422-1425.
16. Betzig, E., Finn, P. L., and Weiner, J. S. (1992). "Combined Shear Force and Near-Field Scanning Optical Microscopy." *Applied Physics Letters*, 60(20), 2484-2486.
17. Betzig, E., Harootunian, A., Lewis, A., and Isaacson, M. (1986). "Near-field diffraction by a slit: implications for superresolution microscopy." *Applied Optics*, 25(12), 1890-900.
18. Betzig, E., and Trautman, J. K. (1992). "Near-Field Optics - Microscopy, Spectroscopy, and Surface Modification Beyond the Diffraction Limit." *Science*, 257(5067), 189-195.
19. Betzig, E., Trautman, J. K., Harris, T. D., Weiner, J. S., and Kostelak, R. L. (1991). "Breaking the Diffraction Barrier - Optical Microscopy On a Nanometric Scale." *Science*, 251(5000), 1468-1470.
20. Bian, R. X., Dunn, R. C., Xie, X. S., and Leung, P. T. (1995). "Single Molecule Emission Characteristics In Near-Field Microscopy." *Physical Review Letters*, 75(26), 4772-4775.
21. Blatchford, J. W., Gustafson, T. L., Epstein, A. J., Vandenbout, D. A., Kerimo, J., Higgins, D. A., Barbara, P. F., Fu, D. K., Swager, T. M., and Macdiarmid, A. G. (1996). "Spatially and Temporally Resolved Emission From Aggregates In Conjugated Polymers." *Physical Review B-Condensed Matter*, 54(6), R3683-R3686.
22. Bobroff, N. (1986). "Position Measurement With A Resolution And Noise-Limited Instrument." *Review Of Scientific Instruments*, 57, 1152.
23. Born, M., and Wolf, E. (1980). *Principles of Optics*, Pergamon Press, Oxford.
24. Buratto, S. K., Hsu, J. W. P., Betzig, E., Trautman, J. K., Bylsma, R. B., Bahr, C. C., and Cardillo, M. J. (1994a). "Near-Field Photoconductivity - Application to Carrier Transport In Ingaasp Quantum Well Lasers." *Applied Physics Letters*, 65(21), 2654-2656.
25. Buratto, S. K., Hsu, J. W. P., Trautman, J. K., Betzig, E., Bylsma, R. B., Bahr, C. C., and Cardillo, M. J. (1994b). "Imaging Ingaasp Quantum-Well Lasers Using Near-Field Scanning Optical Microscopy." *Journal Of Applied Physics*, 76(12), 7720-7725.
26. Capaldi, R. A. (1994). "Coupling between catalytic sites and the proton channel in F1F0-type ATPases." *Trends in Biochemical Sciences*, 19, 284-289.
27. Capaldi, R. A. (1995). *private communication.*
28. Chishti, A. H., Andrabi, K. I., Derick, L. H., Palek, J., and Liu, S. (1992). *Mol. Biochem. Parasitol.*, 52, 283-288.
29. Croci, M., Muschenborn, H. J., Guttler, F., Renn, A., and Wild, U. P. (1993). "Single Molecule Spectroscopy - Pressure Effect On Pentacene In P-Terphenyl." *Chemical Physics Letters*, 212(1-2), 71-77.
30. Dexter, D. L. (1953). *Journal Of Chemical Physics*, 21, 836-850.
31. Discher, D. E., Winardi, R., Schischmanoff, P. O., Pavra, M., Conboy, J. G., and Mohandas, N. (1995). *Journal of Cell Biology*, 130, 897-907.

32. Empedocles, S. A., Norris, D. J., and Bawendi, M. G. (1996). "Photoluminescence Spectroscopy Of Single Cdse Nanocrystallite Quantum Dots." *Physical Review Letters*, 77(18), 3873-3876.
33. Enderle, T., Ha, T., Chemla, D. S., Magowan, C., and Weiss, S. (1996). "Surface specific mapping and co-localization of malarial and host proteins in red-blood-cell membrane by dual-color near-field scanning optical microscopy." *To be published in Proceedings of the National Academy of Sciences of the United States of America.*
34. Forster, T. (1948). "Intermolecular energy migration and fluorescence." *Ann. Phys.*, 2, 55-75.
35. Frohn, J., Wolf, J. F., Besocke, K., and Teske, M. (1989). "Coarse tip distance adjustment and positioner for a scanning tunneling microscope." *Review Of Scientific Instruments*, 60, 1200.
36. Funatsu, T., Harada, Y., Tokunaga, M., Saito, K., and Yanagida, T. (1995). "Imaging Of Single Fluorescent Molecules and Individual ATP Turnovers By Single Myosin Molecules In Aqueous Solution." *Nature*, 374(6522), 555-559.
37. Gill, P. E., Murray, W., and Wright, M. H. (1981). *Practical Optimization*, Academic Press, New York.
38. Gregor, M. J., Blome, P. G., Schofer, J., and Ulbrich, R. G. (1996). "Probe Surface Interaction In Near-Field Optical Microscopy - the Nonlinear Bending Force Mechanism." *Applied Physics Letters*, 68(3), 307-309.
39. Gregor, M. J., Blome, P. G., Ulbrich, R. G., Grossmann, P., Grosse, S., Feldmann, J., Stolz, W., Gobel, E. O., Arent, D. J., Bode, M., Bertness, K. A., and Olson, J. M. (1995). "Near-Field Optical Characterization Of the Photoluminescence From Partially Ordered (Gain)P." *Applied Physics Letters*, 67(24), 3572-3574.
40. Grober, R. D., Harris, T. D., Trautman, J. K., Betzig, E., Wegscheider, W., Pfeiffer, L., and West, K. (1994). "Optical Spectroscopy Of a Gaas/Algaas Quantum Wire Structure Using Near-Field Scanning Optical Microscopy." *Applied Physics Letters*, 64(11), 1421-1423.
41. Gruenberg, J., Allred, D. R., and Sherman, I. W. (1983). *Journal of Cell Biology*, 97, 795-802.
42. Guthold, M., Bezanilla, M., Erie, D. A., Jenkins, B., Hansma, H., and Bustamante, C. (1994). "Following the assembly of RNA polymerase-DNA complexes in aqueous solutions with the scanning force microscope." *Proceedings Of the National Academy Of Sciences Of the United States Of America*, 91(26), 12927-31.
43. Guttler, F., Sepiol, J., Plakhotnik, T., Mitterdorfer, A., Renn, A., and Wild, U. P. (1993). "Single Molecule Spectroscopy - Fluorescence Excitation Spectra with Polarized Light." *Journal of Luminescence*, 56(N1-6), 29-38.
44. Ha, T., Chemla, D. S., Enderle, T., and Weiss, S. (1996a). "Single molecule spectroscopy with automated positioning." *To be published in Applied Physics Letters.*
45. Ha, T., Chemla, D. S., Enderle, T., and Weiss, S. (1996b). "Strategy for room temperature spectroscopy of single molecules." *submitted.*

46. Ha, T., Enderle, T., Chemla, D. S., Selvin, P. R., and Weiss, S. (1996c). "Single Molecule Dynamics Studied By Polarization Modulation." *Physical Review Letters*, 77(19), 3979-3982.
47. Ha, T., Enderle, T., Chemla, D. S., and Weiss, S. (1996d). "Dual-molecule spectroscopy: molecular rulers for the study of biological macromolecules." *To be published in IEEE Journal of Special Topics in Quantum Electronics*.
48. Ha, T., Enderle, T., Ogletree, D. F., Chemla, D. S., Selvin, P. R., and Weiss, S. (1996e). "Probing the Interaction Between Two Single Molecules - Fluorescence Resonance Energy Transfer Between a Single Donor and a Single Acceptor." *Proceedings Of the National Academy Of Sciences Of the United States Of America*, 93(13), 6264-6268.
49. Ha, T., Enderle, T., Selvin, P. R., Chemla, D. S., and Weiss, S. (1996f). "Room temperature observation of Quantum Jumps." *To be published.*
50. Hansma, H. G., Laney, D. E., Bezanilla, M., Sinsheimer, R. L., and Hansma, P. K. (1995). "Applications For Atomic Force Microscopy Of DNA." *Biophysical Journal*, 68(5), 1672-7.
51. Harootunian, A., Betzig, E., Isaacson, M., and Lewis, A. (1986). "Super-resolution fluorescence near-field scanning optical microscopy." *Applied Physics Letters*, 49(11), 674-6.
52. Harris, T. D., Gershoni, D., Grober, R. D., Pfeiffer, L., West, K., and Chand, N. (1996). "Near-Field Optical Spectroscopy Of Single Quantum Wires." *Applied Physics Letters*, 68(7), 988-990.
53. Hendriks, H. W., and Nienhuis, G. (1988). "Collective quantum jumps in pairs of atoms with two or three states." *Journal of Modern Optics*, 35(8), 1331-43.
54. Hess, H. F., Betzig, E., Harris, T. D., Pfeiffer, L. N., and West, K. W. (1994). "Near-Field Spectroscopy Of the Quantum Constituents Of a Luminescent System." *Science*, 264(5166), 1740-1745.
55. Higgins, D. A., and Barbara, P. F. (1995). "Excitonic Transitions In J-Aggregates Probed By Near-Field Scanning Optical Microscopy." *Journal Of Physical Chemistry*, 99(1), 3-7.
56. Hirschfeld, T. (1976). "Optical microscopic observation of single small molecules." *Applied Optics*, 15, 2965-66.
57. Hsu, J. W. P., Lee, M., and Deaver, B. S. (1995). "A Nonoptical Tip-Sample Distance Control Method For Near-Field Scanning Optical Microscopy Using Impedance Changes In an Electromechanical System." *Review Of Scientific Instruments*, 66(5), 3177-3181.
58. Jalocha, A., and Vanhulst, N. F. (1995). "Dielectric and Fluorescent Samples Imaged By Scanning Near-Field Optical Microscopy In Reflection." *Optics Communications*, 119(1-2), 17-22.
59. Johnson, P., and Garland, P. B. (1982). *Biochem. J.*, 203, 313.
60. Karrai, K., and Grober, R. D. (1995). "Piezoelectric Tip-Sample Distance Control For Near-field Optical Microscopes." *Applied Physics Letters*, 66(14), 1842-1844.
61. Kasche, V., and Lindqvist, L. (1964). *Journal Of Physical Chemistry*, 68, 817.

62. Keller, R. A., Ambrose, W. P., Goodwin, P. M., Jett, J. H., Martin, J. C., and Wu, M. (1996). "Single Molecule Fluorescence Analysis In Solution." *Applied Spectroscopy*, 50(7), A12-A32.
63. Kilejian, A., Rashid, M. A., Aikawa, M., Aji, T., and Yang, Y. F. (1991). *Mol. Biochem. Parasitol.*, 44, 175-182.
64. Kohler, J., Disselhorst, J., Donckers, M., Groenen, E. J. J., Schmidt, J., and Moerner, W. E. (1993). "Magnetic Resonance Of a Single Molecular Spin." *Nature*, 363(6426), 242-244.
65. Kosturko, L. D., Daub, E., and Murialdo, H. (1989). "The interaction of E. coli integration host factor and lambda cos DNA: multiple complex formation and protein-induced bending." *Nucl. Acids Res.*, 17(1), 317-333.
66. Lawande, S. V., Lawande, Q. V., and Jagatap, B. N. (1989). "Role Of the Dipole-Dipole Interaction In the Interpretation Of Quantum Jumps In 2 3-Level Atoms." *Physical Review a-General Physics*, 40(6), 3434-3437.
67. Leech, J. H., Barnwell, J. W., Aikawa, M., Miller, L. H., and Howard, R. J. (1984). *Journal of Cell Biology*, 98, 1256-1264.
68. Leong, J. K., and Williams, C. C. (1995). "Shear Force Microscopy With Capacitance Detection For Near-Field Scanning Optical Microscopy." *Applied Physics Letters*, 66(11), 1432-1434.
69. Lewenstein, M., and Javanainen, J. (1987). "Cooperative quantum jumps with two atoms." *Physical Review Letters*, 59(12), 1289-92.
70. Lewis, A., Isaacson, A., Harootunian, A., and Muray, A. (1984). "Development of a 500 Å spatial resolution light microscope. I. Light is efficiently transmitted through lambda /16 diameter apertures." *Ultramicroscopy*, 13, 227-230.
71. Lieberman, K., and Lewis, A. (1993). "Simultaneous Scanning Tunneling and Optical Near-Field Imaging With a Micropipette." *Applied Physics Letters*, 62(12), 1335-1357.
72. Lobel, R. B., and Schleif, R. F. (1990). "DNA Looping And Unlooping By Ara C Protein." *Science*, 250, 528-532.
73. Lu, H. P., and Xie, X. S. (1996). "Single Molecule Spectral Fluctuations at Room Temperature." *To be published.*
74. Lustigman, S., Anders, R. F., Brown, G. V., and Coppel, R. L. (1990). *Mol. Biochem. Parasitol.*, 38, 261-270.
75. Macklin, J. J., Trautman, J. K., Harris, T. D., and Brus, L. E. (1996). "Imaging and Time-Resolved Spectroscopy Of Single Molecules At an Interface." *Science*, 272(5259), 255-258.
76. Magowan, C., Coppel, R. L., Lau, A. O. T., Moronne, M. M., Tchernia, G., and Narla, M. (1995). *Blood*, 86, 3196-3204.
77. Martin, Y., Zenhausern, F., and Wickramasinghe, H. K. (1996). "Scattering Spectroscopy Of Molecules At Nanometer Resolution." *Applied Physics Letters*, 68(18), 2475-2477.
78. Meixner, A. J., Zeisel, D., Bopp, M. A., and Tarrach, G. (1995). "Super-Resolution Imaging and Detection Of Fluorescence From Single Molecules By Scanning Near-Field Optical Microscopy." *Optical Engineering*, 34(8), 2324-2332.

79. Mertz, J., Xu, C., and Webb, W. W. (1995). "Single-Molecule Detection By Two-Photon-Excited Fluorescence." *Optics Letters*, 20(24), 2532-2534.
80. Moerner, W. E., Kador, L. (1989). "Optical detection and spectroscopy of single molecules in a solid." *Phys. Rev. Lett.*, 62(21), 2535-38.
81. Moyer, P. J., Kammer, S., Walzer, K., and Hietschold, M. (1995). "Investigations Of Liquid Crystals and Liquid Ambients Using Near-Field Scanning Optical Microscopy." *Ultramicroscopy*, 61(1-4), 291-294.
82. Muramatsu, H., Chiba, N., Homma, K., Nakajima, K., Ataka, T., Ohta, S., Kusumi, A., and Fujihira, M. (1995). "Near-Field Optical Microscopy In Liquids." *Applied Physics Letters*, 66(24), 3245-3247.
83. Nagourney, W., Sandberg, J., and Dehmelt, H. (1986). "Shelved optical electron amplifier: observation of quantum jumps." *Physical Review Letters*, 56(26), 2797-9.
84. Nie, S. M., Chiu, D. T., and Zare, R. N. (1994). "Probing Individual Molecules With Confocal Fluorescence Microscopy." *Science*, 266(5187), 1018-1021.
85. Nirmal, M., Dabbousi, B. O., Bawendi, M. G., Macklin, J. J., Trautman, J. K., Harris, T. D., and Brus, L. E. (1996). "Fluorescence Intermittency In Single Cadmium Selenide Nanocrystals." *Nature*, 383(6603), 802-804.
86. Orrit, M., and Bernard, J. (1990). "Single Pentacene Molecules Detected By Fluorescence Excitation In a Para-Terphenyl Crystal." *Physical Review Letters*, 65(21), 2716-2719.
87. Pawley, J. B. (1995). Handbook of biological confocal microscopy, Plenum Press, New York.
88. Plakhotnik, T., Walser, D., Pirotta, M., Renn, A., and Wild, U. P. (1996). "Nonlinear Spectroscopy On a Single Quantum System - Two-Photon Absorption Of a Single Molecule." *Science*, 271(5256), 1703-1705.
89. Pohl, D. W., Denk, W., and Lanz, M. (1984). "Optical stethoscopy: Image recording with resolution lambda /20." *Applied Physics Letters*, 42, 651-653.
90. Reilly, P. D., and Skinner, J. L. (1993). "Spectral Diffusion Of Single Molecule Fluorescence - a Probe Of Low-Frequency Localized Excitations In Disordered Crystals." *Physical Review Letters*, 71(25), 4257-4260.
91. Richter, M. L., Snyder, B., McCarty, R. E., and Hammes, G. G. (1985). "Binding stoichiometry and structural mapping of the epsilon polypeptide of chloroplast coupling factor 1." *Biochemistry*, 24(24), 5755-5763.
92. Sabbert, D., Engelbrecht, S., and Junge, W. (1996). "Intersubunit Rotation In Active F-Atpase." *Nature*, 381(6583), 623-625.
93. Sase, I., Miyata, H., Corrie, J. E. T., Craik, J. S., and Kinosita, K. (1995). "Real Time Imaging Of Single Fluorophores On Moving Actin With an Epifluorescence Microscope." *Biophysical Journal*, 69(2), 323-328.
94. Sauter, T., Blatt, R., Neuhauser, W., and Toschek, P. E. (1986a). "'Quantum jumps' observed in the fluorescence of a single ion." *Optics Communications*, 60(5), 287-92.
95. Sauter, T., Neuhauser, W., Blatt, R., and Toschek, P. E. (1986b). "Observation of quantum jumps." *Physical Review Letters*, 57(14), 1696-8.

96. Scalettar, B. A., Selvin, P. R., Axelrod, D., Klein, M. P., and Hearst, J. E. (1990). "A Polarized Photobleaching Study Of Dna Reorientation In Agarose Gels." *Biochemistry*, 29(20), 4790-4798.

97. Schmidt, T., Schutz, G. J., Baumgartner, W., Gruber, H. J., and Schindler, H. (1996). "Imaging Of Single Molecule Diffusion." *Proceedings Of the National Academy Of Sciences Of the United States Of America*, 93(7), 2926-2929.

98. Shalom, S., Lieberman, K., Lewis, A., and Cohen, S. R. (1992). "A Micropipette Force Probe Suitable For Near-Field Scanning Optical Microscopy." *Review Of Scientific Instruments*, 63(9), 4061-4065.

99. Sheppard, C. J. R., and Wilson, T. (1978). "Depth Of Field In The Scanning Microscope." *Optics Letters*, 3, 115-117.

100. Shera, E. B., Seitzinger, N. K., Davis, L. M., Keller, R. A., and Soper, S. A. (1990). "Detection Of Single Fluorescent Molecules." *Chemical Physics Letters*, 174(6), 553-557.

101. Singh, S., Turnia, P., Capaldi, R. A., and Keller, D. "Structure of the F1Fo ATP Synthase from E.coli." *STM '95: 8th International Conference on Scanning Tunneling Microscopy / Spectroscopy and Related Techniques*.

102. Stahelin, M., Bopp, M. A., Tarrach, G., Meixner, A. J., and Zschokkegranacher, I. (1996). "Temperature Profile Of Fiber Tips Used In Scanning Near-Field Optical Microscopy." *Applied Physics Letters*, 68(19), 2603-2605.

103. Stryer, L., and Haugland, R. P. (1967). *Proceedings Of the National Academy Of Sciences Of the United States Of America*, 58, 719-730.

104. Toledo-Crow, R., Yang, P. C., Chen, Y., and Vaeziravani, M. (1992). "Near-Field Differential Scanning Optical Microscope With Atomic Force Regulation." *Applied Physics Letters*, 60(24), 2957-2959.

105. Trautman, J. K., and Macklin, J. J. (1996). "Time-Resolved Spectroscopy Of Single Molecules Using Near-Field and Far-Field Optics." *Chemical Physics*, 205(1-2), 221-229.

106. Trautman, J. K., Macklin, J. J., Brus, L. E., and Betzig, E. (1994). "Near-Field Spectroscopy Of Single Molecules At Room Temperature." *Nature*, 369(6475), 40-42.

107. Turina, P., and Capaldi, R. A. (1994). "ATP hydrolysis-driven structural changes in the gamma-subunit of Escherichia coli ATPase monitored by fluorescence from probes bound at introduced cysteine residues." *Journal of Biological Chemistry*, 269(18), 13465-71.

108. Valaskovic, G. A., Holton, M., and Morrison, G. H. (1995). "Parameter Control, Characterization, and Optimization In the Fabrication Of Optical Fiber Near-Field Probes." *Applied Optics*, 34(7), 1215-1228.

109. Vale, R. D., Funatsu, T., Pierce, D. W., Romberg, L., Harada, Y., and Yanagida, T. (1996). "Direct Observation Of Single Kinesin Molecules Moving Along Microtubules." *Nature*, 380(6573), 451-453.

110. Vamosi, G., Gohlke, C., and Clegg, R. M. (1996). "Fluorescence Characteristics Of 5-Carboxytetramethylrhodamine Linked Covalently to the 5' End Of Oligonucleotides - Multiple Conformers Of Single-Stranded and Double-Stranded Dye-Dna Complexes." *Biophysical Journal*, 71(2), 972-994.

111. Vanhulst, N. F., and Moers, M. H. P. (1996). "Biological Application Of Near-Field Optical Microscopy." *Ieee Engineering In Medicine and Biology Magazine*, 15(1), 51-58.
112. Vanhulst, N. F., Moers, M. H. P., Noordman, O. F. J., Tack, R. G., Segerink, F. B., and Bolger, B. (1993a). "Near-Field Optical Microscope Using a Silicon-Nitride Probe." *Applied Physics Letters*, 62(5), 461-463.
113. Vanhulst, N. F., Moers, M. H. P., Tack, R. G., and Bolger, B. (1993b). "Combined Scanning Near-field Optical and Force Microscopy." *Microscopy Research and Technique*, 25(2), 177-178.
114. Vogel, M., Gruber, A., Wrachtrup, J., and Vonborczyskowski, C. (1995). "Determination Of Intersystem Crossing Parameters Via Observation Of Quantum Jumps On Single Molecules." *Journal Of Physical Chemistry*, 99(41), 14915-14917.
115. Widengren, J., Rigler, R., and Mets, U. (1994). "Triplet-State Monitoring by Fluorescence Correlation Spectroscopy." *Journal of Fluorescence*, 4, 255.
116. Wild, U. P., Guttler, F., Pirotta, M., and Renn, A. (1992). "Single Molecule Spectroscopy - Stark Effect Of Pentacene In Para-Terphenyl." *Chemical Physics Letters*, 193(6), 451-455.
117. Wilkerson, C. W., Goodwin, P. M., Ambrose, W. P., Martin, J. C., and Keller, R. A. (1993). "Detection and Lifetime Measurement Of Single Molecules In Flowing Sample Streams By Laser-Induced Fluorescence." *Applied Physics Letters*, 62(17), 2030-2032.
118. Wrachtrup, J., Vonborczyskowski, C., Bernard, J., Orrit, M., and Brown, R. (1993a). "Optical Detection Of Magnetic Resonance In a Single Molecule." *Nature*, 363(6426), 244-245.
119. Wrachtrup, J., Vonborczyskowski, C., Bernard, J., Orrit, M., and Brown, R. (1993b). "Optically Detected Spin Coherence Of Single Molecules." *Physical Review Letters*, 71(21), 3565-3568.
120. Wyman, C., Grotkopp, E., Bustamante, C., and Nelson, H. C. (1995). "Determination of heat-shock transcription factor 2 stoichiometry at looped DNA complexes using scanning force microscopy." *Embo Journal*, 14(1), 117-23.
121. Xie, X. S., and Dunn, R. C. (1994). "Probing Single Molecule Dynamics." *Science*, 265(5170), 361-364.
122. Xu, C., and Webb, W. W. (1996). "Measurement Of Two-Photon Excitation Cross Sections Of Molecular Fluorophores With Data From 690 to 1050 nm." *Journal Of the Optical Society Of America B-Optical Physics*, 13(3), 481-491.
123. Zenhausern, F., Martin, Y., and Wickramasinghe, H. K. (1995). "Scanning Interferometric Apertureless Microscopy - Optical Imaging At 10 Angstrom Resolution." *Science*, 269(5227), 1083-1085.
124. Zenhausern, F., Oboyle, M. P., and Wickramasinghe, H. K. (1994). "Apertureless Near-Field Optical Microscope." *Applied Physics Letters*, 65(13), 1623-1625.